GEOLOGIC MAP OF THE SULTAN 7.5-MINUTE QUADRANGLE, KING AND SNOHOMISH COUNTIES, WASHINGTON

by Joe D. Dragovich, Heather A. Littke,
Shannon A. Mahan, Megan L. Anderson,
James H. MacDonald, Jr., Recep Cakir,
Bruce A. Stoker, Curtis J. Koger,
John P. Bethel, S. Andrew DuFrane,
Daniel T. Smith, and Nathan M. Villeneuve

WASHINGTON
DIVISION OF GEOLOGY
AND EARTH RESOURCES
Map Series 2013-01
October 2013

WASHINGTON STATE DEPARTMENT OF
Natural Resources
Peter Goldmark - Commissioner of Public Lands

DISCLAIMER

INDEMNIFICATION

Research supported by the U.S. Geological Survey, National Cooperative Geologic Mapping Program, under USGS award number G12AC20234. The views and conclusions contained in this document are those of the authors and should not be interpreted as necessarily representing the official policies, either expressed or implied, of the U.S. Government.

WASHINGTON STATE DEPARTMENT OF NATURAL RESOURCES

DIVISION OF GEOLOGY AND EARTH RESOURCES

Washington Department of Natural Resources
Division of Geology and Earth Resources

Mailing Address:
MS 47007
Olympia, WA 98504-7007

Street Address:
Natural Resources Bldg, Rm 148
1111 Washington St SE
Olympia, WA 98501

Phone: 360-902-1450; *Fax:* 360-902-1785
E-mail: geology@dnr.wa.gov
Website: http://www.dnr.wa.gov/geology

Publications List:
http://www.dnr.wa.gov/ResearchScience/Topics/GeologyPublicationsLibrary/Pages/pubs.aspx

Washington Geology Library Catalog:
http://www.dnr.wa.gov/ResearchScience/Topics/GeologyPublicationsLibrary/Pages/washbib.aspx

Washington State Geologic Information Portal:
http://www.dnr.wa.gov/geologyportal

Suggested Citation: Dragovich, J. D.; Littke, H. A.; Mahan, S. A.; Anderson, M. L.; MacDonald, J. H., Jr.; Cakir, Recep; Stoker, B. A.; Koger, C. J.; DuFrane, S. A.; Bethel, J. P.; Smith, D. T.; Villeneuve, N. M., 2013, Geologic map of the Sultan 7.5-minute quadrangle, Snohomish and King Counties, Washington: Washington Division of Geology and Earth Resources Map Series 2013-01, 1 sheet, scale 1:24,000, plus 52 p. text.

Published in the United States of America

GLOSSARY

apsl – above present sea level
CCFZ – Cherry Creek fault zone
CF – Carnation fault
IRSL – infrared stimulated luminescence
K-spar – potassium feldspar
LP – local provenance
M_D – duration magnitude
MF – Monroe fault
M_L – local magnitude
NP – northern provenance
OSL – optically stimulated luminescence
PF – plagioclase feldspar
PG – Puget Group provenance
Qm – monocrystalline quartz
Qp – polycrystalline quartz
RMFZ – Rattlesnake Mountain fault zone
SP – Snoqualmie or Skykomish River basin provenance
SWIF – southern Whidbey Island fault zone
TCFZ – Tokul Creek fault zone

Table of Contents

List of Figures

List of Tables

Geologic Map of the Sultan 7.5-minute Quadrangle, Snohomish and King Counties, Washington

by Joe D. Dragovich[1], Heather A. Littke[1], Shannon A. Mahan[2], Megan L. Anderson[3], James H. MacDonald Jr.[4], Recep Cakir[1], Bruce A. Stoker[5], Curtis J. Koger[6], S. Andrew DuFrane[7], John P. Bethel[8], Daniel T. Smith[8], and Nathan M. Villeneuve[1]

[1] Washington Division of Geology and Earth Resources
MS 47007
Olympia, WA 98504-7007

[2] U.S. Geological Survey
Box 25046, MS 974
Denver Federal Center
Denver, CO 80225-5046

[3] Colorado College
Department of Geology
14 E Cache La Poudre St
Colorado Springs, CO 80903

[4] Florida Gulf Coast University
Department of Marine and Ecological Science
Fort Myers, FL 33965

[5] Earth Systems
19729 207th Ave SE
Monroe, WA 98272

[6] Associated Earth Sciences, Inc.
911 5th Ave, Suite 100
Kirkland, WA 98033

[7] University of Alberta
Department of Earth and Atmospheric Sciences
1-26 Earth Sciences Building
Edmonton, Alberta, Canada T6G

[8] King County Department of Natural Resources and Parks
Water and Land Resource Division
201 S Jackson St
Seattle, WA 98104

INTRODUCTION

The Sultan map is the seventh in a series of 7.5-minute quadrangle geologic maps, each of which represents a year-long effort to document surficial and bedrock geology and geologic structures in King and Snohomish Counties—a densely populated region that is seismically active. As described below, active or potentially active structures include the southern Whidbey Island fault zone (SWIF), Cherry Creek fault zone (CCFZ), Carnation fault, and probably the Monroe fault and Monroe syncline (Fig 1). These structures are responding to north–south crustal compression across the Puget Lowland of western Washington. A bedrock high north of the Carnation fault and south of the Monroe fault is proposed as a 'pop-up' structure between these reverse faults with opposite vergence. To enhance our mapping effort, we have added detailed field observations and several types of geological analyses to existing data, including prior geologic mapping (for example, Tabor and others, 1993; Booth, 1990). We include geotechnical findings from Snohomish County road and bridge engineering studies, as well as surface and subsurface information from several geotechnical companies. The map sheet presents the geologic map, cross sections, provenance table, correlation diagram, and geophysical maps and models of the cross sections. Appendices A and B present radiocarbon, optically stimulated luminescence (OSL), and infrared stimulated luminescence (IRSL) age information for Quaternary deposits. Appendices C through F provide further geochemical, earthquake, U-Pb age data and photographs, respectively. We follow the nomenclature of Booth (1990) for glacial features, such as Vashon stade proglacial lakes (for example, 'Glacial Lake Skykomish'). Names of all faults, folds, and geomorphic features shown on the geologic map, such as the Monroe fault, are informal. The term "volcanic rocks of Mount Persis" of Tabor and others (1993) is herein abbreviated to Mount Persis unit. We use the informal term "Olympia beds" in the same sense as the "deposits of the Olympia nonglacial interval" was used by Pessl and others (1989).

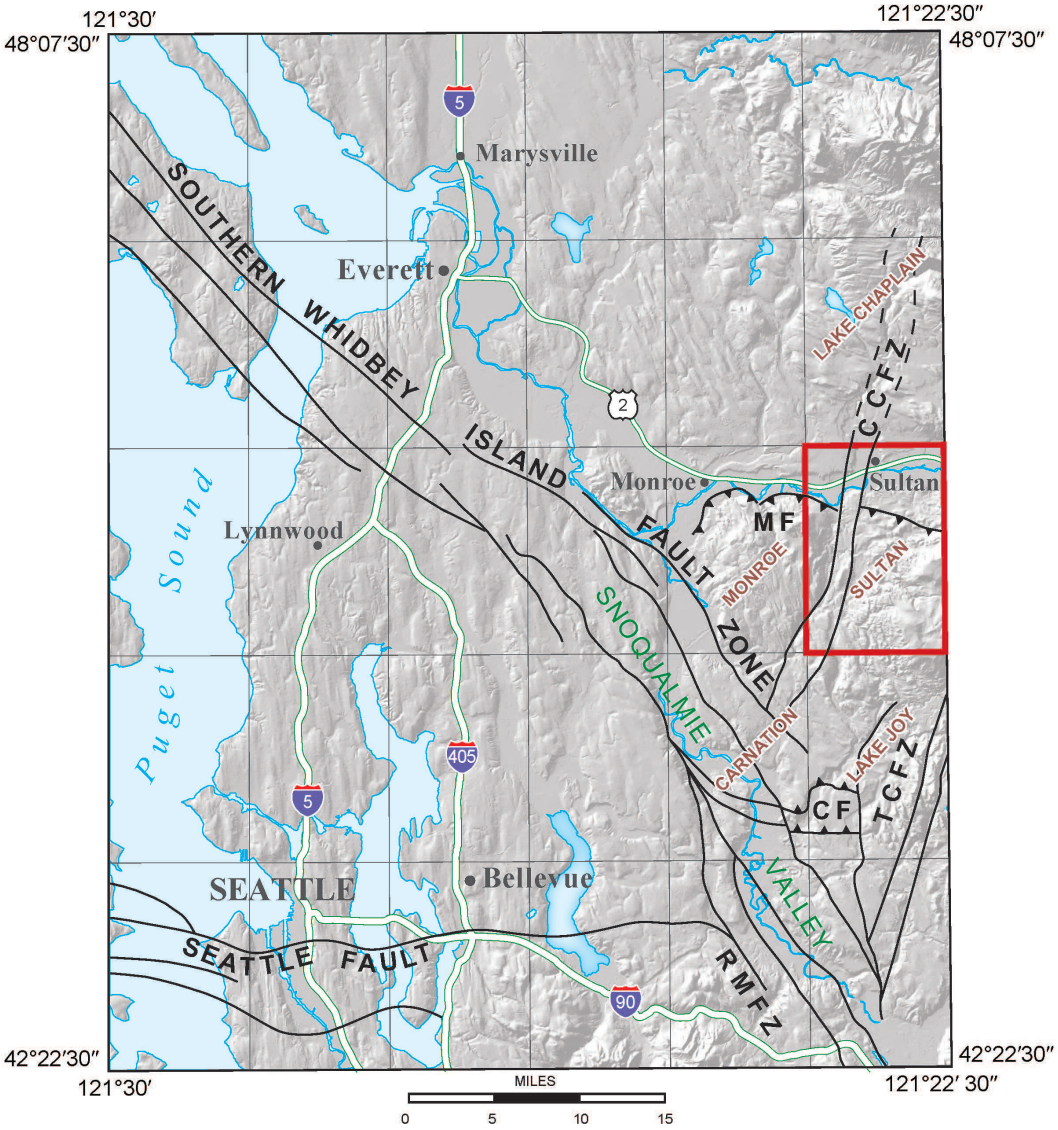

Figure 1. Simplified regional tectonic map of the central Puget Lowland and Cascade foothills showing the Sultan 7.5-minute quadrangle (red border). Current mapping indicates that the Cherry Creek fault zone (CCFZ) projects into the Lake Chaplain quadrangle north of the Sultan quadrangle. The Tokul Creek fault zone (TCFZ) is similar to the CCFZ and is likely a left-lateral fault zone conjugate to the SWIF. MF, Monroe fault; CF, Carnation fault.

DESCRIPTION OF MAP UNITS

We used the Udden-Wentworth scale (Pettijohn, 1957) to classify unconsolidated sediments, Dickinson's (1970) terminology for sandstones, and Le Maitre and others' (2002) and Frost and others' (2001) terminology for volcanic rocks. Clinopyroxenes are collectively described as 'augite' but may include other petrographically similar varieties. We use the time scales of the U.S. Geological Survey Geologic Names Committee (2010) and Wolfe and others (1998). Description of weathering rinds on basaltic clasts follows the methodology of Colman and Pierce (1981). Thin-section point-count data on the sand-size fractions helped differentiate several glacial and nonglacial units. An important compositional discriminator for Quaternary strata studied for this report is the average percentage of monocrystalline quartz (Qm) versus quartz-mica tectonite/polycrystalline quartz/chert (Qp) versus potassium feldspar (K-spar) ternary system and shown as $Qm_xQp_xPF_x$. The normalized $Qm_xQp_xPF_x$ data provided below were obtained from petrographic examination of 20 sand samples from the Sultan quadrangle as well as from Dragovich (2007) and Dragovich and others (2009b, 2010a,b, 2012). Percentages given for individual mineral or lithic grains

are not normalized and represent the whole clast population. Quaternary sand deposit provenances are defined by compositional data derived from sand point-count data, petrographic observations, and sand geochemistry, as well as field data and observations (Table 1). Nonglacial Pleistocene geologic units, such as ancient Skykomish River alluvium ('Olympia beds'; unit Qc$_o$), have Holocene analogues (modern Skykomish River alluvium) with similar facies and provenance. (See *Pleistocene Alluvium and Quaternary Structures* section for more information.)

Table 1. Sedimentary provenances for Quaternary deposits for the Sultan, Lake Joy, Monroe, Carnation, North Bend, Fall City, and Snoqualmie quadrangles (Dragovich, 2007; Dragovich and others, 2009a,b,c, 2010a,b, 2011a,b, 2012, this study). Geologic units in the Sultan quadrangle are shown in bold. Provenances are defined by compositional data derived from sand point-count data, petrographic observations, sand geochemistry, and field data. Nonglacial Pleistocene geologic units were deposited in fluvial depositional environments similar to modern (Holocene) major or minor river deposits of the same provenance. RMFZ = Rattlesnake Mountain fault zone; SWIF = southern Whidbey Island fault zone.

Group	Geologic unit(s)	Provenance and facies notes
SP (Snoqualmie or Skykomish River basin provenance)	**Qa** (Snoqualmie and Skykomish Rivers), **Qc$_o$**, Qc$_{WS}$, Qc$_h$, **Qc$_{pf}$**	Snoqualmie and Skykomish River basins or central Cascade (nonglacial) provenance with easterly erosional sources carried by rivers generally flowing west. The major bedrock erosional sources for SP sediments are Tertiary intrusive rock bodies such as the expansive Snoqualmie, Index and Grotto batholiths. Ancient and modern Skykomish River alluvial facies are similar to ancient and modern Snoqualmie River alluvial facies. These nonglacial units contain abundant monocrystalline quartz, K-spar, and plagioclase, lesser but distinct granitic lithic grains, biotite, pyroxene, and hornblende. Dragovich and others (2009a,b,c, 2010a,b, 2011a,b, 2012, this study) postulate structural control of parts of major river valleys by faults, such as the RMFZ–SWIF or Monroe fault system, resulting in locally thick sedimentary basins, deformed SP stratigraphic sequences and (or) the creation of inverted basins.
LP (local provenance)	**Qa** (Tolt River and Youngs–Elwell Creek), **Qc$_{ol}$**, Qc$_{hmp}$	Nonglacial small-basin provenance with local sources carried by low-order rivers flowing generally west, away from the Cascade foothills. Examples include both the modern and ancient Tolt River and Youngs–Elwell Creek basins (40–100 mi^2; 104–259 km^2). Modern Tolt River alluvium is compositionally and stratigraphically similar to ancient Tolt River alluvium and alluvial fan deposits (Dragovich and others, 2010a,b, 2012). Sediments are distinctly locally sourced and contain significant volcanic lithic grains, meta-argillite, and metasandstone, primarily derived from the volcanic rocks of Mount Persis and Western mélange belt. Like the modern Tolt River fan at the city of Carnation, ancient Tolt River alluvium may have interfingered with ancient Snoqualmie River alluvium locally and may include alluvial fan deposits (Dragovich and others, 2012). Ancient Youngs–Elwell Creek alluvium appears to interfinger with SP alluvium (unit Qc$_o$) southwest of the city of Sultan, similar to the modern interaction of the Skykomish River with the Youngs–Elwell Creek alluvial system.
PG (Puget Group provenance)	Qc$_{wp}$	Puget Group nonglacial provenance with local erosional sources to the south and southwest originating from the Seattle uplift (for example, Tiger Mountain) and delivered via fluvial mechanisms. Sands are lithic rich. Whidbey Formation (unit Qc$_{wp}$) strata in the southwestern portion of the Carnation quadrangle (Dragovich and others, 2010a,b) are derived from the Puget Group and contain significant andesite detritus, as well as some arkosic (feldspathic) sandstone, and siltstone from the Tukwila, Renton, and Tiger Mountain Formations. Whereas LP sediments in the current quadrangle and previous nearby study areas are derived from Mount Persis unit volcanics and Western mélange belt bedrock sources, PG in the Carnation quadrangle is derived from Puget Group sources and can be seen as a subdivision of local provenance (LP). Both LP and PG represent relatively small-basin, low-order river deposits compared to SP and NP, and thus represent smaller stream, river, and fan deposits. Fluvial PG sediments may interfinger with ancient SP fluvial sediments southwest of the current map area near the city of Carnation; this is similar to the interaction of modern Raging River–Snoqualmie River alluvial facies at Fall City where modern PG and SP sediments interfinger (Dragovich and others, 2010a,b).
NP (northern provenance)	**Qgl$_r$**, **Qgos**, **Qgod**, **Qgof**, **Qgic**, **Qgik**, **Qgog**, **Qgt$_v$**, **Qga$_v$**, **Qgl$_v$**, Qgt$_p$, Qgo$_p$, Qgl$_p$, Qgd$_d$, Qgd$_{pd}$	Northern provenance deposited during continental glaciations. Sediments are locally mixed with some sediments of eastern and northeastern Cascade provenance (particularly for some Vashon stade recessional deposits transported by ice-marginal meltwater). Glacial units contain various lithic clast types, including high-grade metamorphic clasts, and have a high polycrystalline/monocrystalline quartz ratio and less K-spar when compared to local Cascade sources. Sand grain types tend to be polymictic or varied due to the complexity of the northern provenance.

Quaternary Sedimentary Deposits

HOLOCENE NONGLACIAL DEPOSITS

Qp **Peat**—Loose or soft peat, muck, and organic silt and clay with local thin beds of Mazama ash (Knoll, 1967). Peat is also interstratified with alluvial deposits along low-energy-river valleys, such as Cherry

Creek, and deposited in upland depressions and kettles over low-permeability glacial deposits or in abandoned channel depressions in the Skykomish River valley. Most of these deposits were mapped using lidar, topographic maps, aerial photographs, and the previous mapping of Booth (1990). We obtained an age of 9,400 ±40 yr BP (age site 40D) from peat interbedded with Youngs Creek alluvium in the central portion of the quadrangle (sec. 19, T27N R8E; Appendix A). We also obtained an IRSL age of 112 ±7.60 ka (age site 43B) in stratified coarse to medium alluvial sand 3 ft (1 m) above age site 40D that we believe to be erroneous, due to its likely erosional path and quick deposition (sec. 30, T27N R8E; Appendix B). Also see radiocarbon ages from peat bogs reported by Yount and others (1980), Broecker and others (1956), and in the Lake Joy quadrangle (Dragovich and others, 2012).

Qa **Alluvium**—Generally sand, silt, (cobble) gravel, gravelly sand, sandy pebble gravel, peat, and organic sediments; subrounded to rounded clasts; loose; well stratified and sorted; plane-bedded sands, wood debris, and detrital wood are common. Young or old Holocene alluvium is mapped in the Skykomish River and Sultan, Youngs, and Elwell Creek valleys. The Skykomish River channel deposits contain more cobble gravel—typical of a higher-energy, braided-river depositional style—but also contain overbank sand, silt, and organic sediments, including peat. Point-bar pebble counts reveal that the gravelly alluvium contains ~20–26% 'granite' (intrusive rocks), ~25% volcanic rocks, as well as ~13–16% metasedimentary rocks. Sands (~71% SiO_2) are mostly light olive gray and contain monocrystalline quartz, plagioclase, and K-spar (~5%), and lesser, but significant, hornblende, pyroxene, and mica; some metasedimentary and greenstone lithic grains, mostly derived from the Western mélange belt, K-spar-bearing true granite, and a few high-grade metamorphic lithic grains.

We obtained an IRSL age of 1.46 ±0.09 ka at age site 44G, taken from a modern channel bar on the north bank of the Skykomish River (sec. 5, T27N R8E; Appendix B). Sultan Creek alluvium is mostly gravel and (gravelly) sand and lesser silt, peat, and organic sediments derived from local sources. Subsurface information suggests this alluvium is ~10 to 80 ft (~3–24 m) thick. Youngs Creek and Elwell Creek alluvium is mostly cobble and boulder gravel, pebble or gravel sand, and sand. Sands (62–78% SiO_2) contain significant volcanic lithic grains (~60%) with lesser metasedimentary lithic grains eroded from the Western mélange belt; they also contain granitic lithic grains, undivided metamorphic lithic grains, monocrystalline and polycrystalline quartz, plagioclase with some pyroxene and hornblende, and rare K-spar. These Holocene deposits are similar to Olympia beds (unit Qc_{ol}) mapped above Elwell Creek. Lower Elwell Creek alluvium is estimated at ~10 to 50 ft (~3–15 m) thick on the basis of a few lithologic well logs. Elwell Creek is directly south of the Skykomish River of which it is a tributary and is an extention of Youngs Creek.

Qoa **Older alluvium**—Generally sand, silt, gravel, peat, and organic sediments; subrounded to rounded clasts; loose; well stratified and sorted; plane-bedded sands, wood debris, and detrital wood are common. Unit Qoa is inset against Pleistocene deposits or bedrock and elevated above the modern Youngs–Elwell Creek or Skykomish River flood plains (Booth, 1990). It includes well-stratified and -sorted, loose sand and gravel similar to unit Qa. Unit Qoa terraces were mapped using field mapping, aerial photographs, and lidar elevation information. Holocene tectonic uplift or tilting may have contributed to the isolation of these alluvial bodies. Older alluvium that is substantially elevated above the Skykomish River may be late Pleistocene fluvial outwash (unit Qgof) that graded to a waning Glacial Lake Skykomish. In this scenario, perched bodies are fluvial-deltaic outwash deposited on the periphery of a shallowing Glacial Lake Skykomish similar to the 'Monroe fan' of Dragovich and others (2011a).

Qls **Landslide deposits (Holocene to latest Pleistocene)**—Diamicton or boulder gravel with minor sand or gravel beds where locally modified by stream processes. Sediments are loose or soft and are typically poorly sorted and unstratified. Clasts are angular to subangular where derived from bedrock, but contain mostly rounded clasts where landslides originated in Quaternary deposits. Mapped landslides include rock falls, lateral spreads, slump-earthflows, debris slumps, and larger debris-flow deposits, but also a few areas of thick colluvium (see landslide classification system of Varnes, 1978a,b). This unit may include chaotic, stratified slump blocks or debris-flow aprons originating in unstable Vashon recessional deposits perched on hillsides. Some landslides may have been initiated during late Pleistocene deglaciation.

Qaf **Alluvial fan deposits (Holocene to latest Pleistocene)**—Debris-flow diamicton, alluvial gravel, boulder gravel, and sand. Sediment is loose, mostly poorly to moderately sorted and moderately stratified to massive. The reduced gradient where streams emerge from confining valleys causes some sediment load to be deposited as a fan. For example, we map lowermost Elwell Creek alluvium as an alluvial fan where the river gradient is significantly reduced, forming a subtle fan-like body at the junction between the creek and the Skykomish River. Unit Qaf deposits are distinguished from unit Qls deposits by their location and regular lobate shape visible on lidar imagery or aerial photographs. Some fans may have initiated as fan deltas that graded to Glacial Lake Skykomish at the close of the last glaciation similar to the 'Monroe fan' at the city of Monroe (Dragovich and others, 2011a).

PLEISTOCENE GLACIAL AND NONGLACIAL DEPOSITS

Vashon Stade of the Fraser Glaciation

Deposits of the Vashon stade of the Fraser glaciation of Armstrong and others (1965) are widely distributed across the study area. Glacial ice and meltwater deposited drift and carved the southern Puget Lowland into a complex geomorphology that provides insight into late Pleistocene glacial processes. Vashon deposits are typically fresh to only slightly weathered; basalt clasts have very thin (commonly <0.5 mm) or no weathering rinds.

Vashon Recessional Deposits

Puget lobe continental ice advanced south across the Puget Lowland and covered the map area (see the ice limit along the eastern edge of the map area at significant site 63M, sec. 27, T27N R8E). Vashon deglaciation in the map area began about 14,000 yr BP along the Cascade Range foothills directly to the east, and the map area was fully deglaciated by about 13,500 yr BP (Porter and Swanson, 1998). The Puget lobe ice front receded across the map area in a northwesterly direction, leaving Vashon recessional deposits. Detailed mapping of the deposits show that lithologies commonly transition texturally horizontally and (or) vertically due to complex facies changes generated by dynamic glacial depositional environments.

During ice recession, a series of ice-marginal lakes and connecting glaciofluvial channels formed in the wake of the retreating ice lobe. The geometry, inset relations, and elevation of these deposits reflect successive lowering of the base level as lower valleys became ice-free and emerging spillways migrated westward and northward; this resulted in younger inset or terraced recessional deposits graded to these spillways (Knoll, 1967; Booth, 1990; Porter and Swanson, 1998).

Booth (1990) subdivided recessional outwash deposits into five stages of deglaciation and emphasized the importance of both ice-marginal and subglacial meltwater paths. For example, some of the southwest-trending valleys traversing the glacial uplands are the result of meltwater erosion and sedimentation in subglacial tunnels and open recessional valleys. Our mapping confirms that ice-marginal meltwater followed several elevated pathways during glacial recession, depositing ice-contact, fluvial, deltaic, kame, and lake sediments. Glacial Lakes Snoqualmie and Skykomish were ice-dammed lakes that covered the Skykomish and Snoqualmie valleys during deglaciation and merged as ice tongues receded down the Snoqualmie and Skykomish valleys to the area near the city of Monroe west of the Sultan area (Mackin, 1941; Booth, 1990; Dragovich and others, 2007, 2009a,c, 2010a,b, 2011a,b, 2012). Glacial lake elevations controlled the location of recessional outwash bodies and smaller lakes in the region. For example, the Tolt River outwash complex of Dragovich and others (2012) directly south of the Sultan map area is graded to Glacial Lake Snoqualmie.

The glacial recessional sands are compositionally distinct from the ancient nonglacial SP alluvium and have a low monocrystalline-quartz grain content and a relatively high polycrystalline quartz to monocrystalline quartz ratio (Dragovich, 2007; Dragovich and others, 2009b, 2010a,b, 2011a,b, 2012)(Table 1). Some recessional sands have a minor but distinct K-spar component (1–8%), as well as some K-spar-bearing granitic lithic grains and significant local mélange belt and Tertiary volcanic detritus. Dragovich and others (2012) related this somewhat elevated K-spar content to the proximity of Tertiary intrusive bodies and 'arkosic' metasandstones of the Western mélange belt of Tabor and others (1993) and local erosion by ice-marginal or internal-recessional pathways.

Qgl_r **Recessional glaciolacustrine deposits**—Silt, clayey or sandy silt, and silty sand, typically with scattered dropstones; local lenses or beds of sand or gravel. Sediments are loose or soft, massive or laminated to thinly bedded, and locally display varve-like rhythmites. Kame lake deposits locally display some soft-sediment deformational features, such as tilted or deformed bedding, and were deposited in small

proglacial lakes in upland ice-marginal settings, such as the Youngs Creek ice-contact complex. Upward-fining sequences record waning lake sedimentation in small proglacial lakes. Upward-coarsening sequences may begin as glacial-lake deposits (units Qgl_r and Qgos) and grade into overlying deltaic (unit Qgod) and fluvial (unit Qgof) deposits as a result of progradation of the outwash complexes into Glacial Lake Skykomish or smaller ice-marginal glacial lake environments. Glacial Lake Skykomish sediments were deposited mostly below ~400 to 440 ft (122–134 m) elevation in the northern part of the map area (Cross Sections A and B). Broecker and others (1956) reported a radiocarbon date of 11,900 yr BP from peat overlying soft blue clay (unit Qgl_r) in the Lake Joy quadrangle (Dragovich and others, 2012), indicating that the area was fully deglaciated before that time.

Qgos **Outwash sand**—Sand and pebbly sand with some interbeds of silty sand, silt, or gravel; sands are typically dark blue-gray, weathering brownish gray. Sediments are loose or soft and vary from unstratified to weakly stratified to plane-bedded, laminated, and, rarely, crossbedded. Vertical and horizontal fining trends indicate mostly shallow-water glaciolacustrine deposition. Unit Qgos complexly interfingers with recessional lake deposits (unit Qgl_r), fluvial outwash deposits (unit Qgof), and deltaic deposits or kame deltaic deposits (unit Qgod). Some unit Qgos sands coarsen upward into unit Qgod sands and gravels, and they locally fine downward to unit Qgl_r silty lake deposits due to deltaic progradation.

Qgod **Deltaic outwash and kame deltas**—Sandy cobble gravel, gravel, (pebbly) sand; sands are typically dark blue-gray to light gray, weathering to yellowish brown or brownish gray. Sediments are loose, moderately to well sorted, and well stratified in thin to very thick beds. Deltas have high-amplitude planar foreset beds graded to temporary ice-dammed lake levels. This unit includes fairly small kame deltas such as unit Qgod in the Youngs Creek ice-contact complex (secs. 9–10, T27N R8E) or ice-free deltas graded to Glacial Lake Skykomish. The Youngs Creek ice-contact complex lacks evidence for near-ice deposition and is graded to the open Glacial Lake Skykomish relict surface (elevation ~420 ft; 128 m) where delta gravels grade to Glacial Lake Skykomish delta front sands (unit Qgos) and glacial lake silts (unit Qgl_r).

Qgof **Fluvial outwash deposits**—Cobble and boulder gravel, gravel, pebbly sand, and interbeds of sand and rare silt; sands are grayish brown, weathering olive-yellow. Sediment is loose and moderately to well stratified and commonly contains medium to very thick subhorizontal beds that have local bar or ripple crossbedding, imbricated gravel, and rip-up clasts. This unit lacks ice-contact sedimentary structures and other geomorphic and stratigraphic evidence for nearby ice, but some unit Qgof outwash grades laterally into ice-contact deposits, particularly in the southwestern portion of the map area around the Youngs Creek ice contact complex. Unit Qgof locally forms the topset beds on deltas (unit Qgod). Inset fluvial outwash terraces in unit Qgof record fluvial incision as base levels dropped and meltwater incised into older glacial deposits (Booth, 1990). As observed in adjacent quadrangles, many terraces record ancient southwest-trending recessional meltwater pathways that generally decrease in elevation to the west and southwest and record hydrologic communication between Glacial Lakes Skykomish and Snoqualmie (Dragovich and others, 2010a,b) via the ancient Tolt River delta of Dragovich and others (2012). The elevation of Glacial Lake Snoqualmie was a major geomorphic control over recessional outwash deposition for the southern part of the map area. For example, unit Qgof inset fluvial terraces are the result of fluvial incision or erosion in response to dropping glacial lake levels.

Qgic **Ice-contact deposits, undivided**—Cobble and boulder gravel and gravel locally containing diamicton, silty pebbly gravel and sand, pebbly sand, and silt. Sediment is loose or soft and mostly moderately stratified, medium to very thickly bedded, and variously sorted; abrupt grain-size changes are common. Ice-contact primary structures include oversteepened and contorted bedding and other ice-shear or slump features, producing variously dipping strata. Diamictons have several origins, including melt-out, debris flow, and water-laid, dropstone-rich diamictons deposited in a variety of settings; these are interstratified with granular supraglacial, englacial, and subglacial meltwater sand and (or) gravel deposits. The upper surface is typically hummocky and contains numerous kettle depressions. The Youngs Creek ice-contact complex has several mappable ice-contact facies, including fluvial-deltaic kames (unit Qgik), glaciofluvial outwash, and hummocky dead-ice facies. Locally, the dead-ice deposits of the complex grade from kame deposits to recessional outwash fluvial deposits (unit Qgof) and are part of a north-

northeast-trending belt of ice-contact deposits, implying an ice margin that waned or stagnated along the highlands during ice recession. Some of the smaller isolated unit Qgic deposits mapped elsewhere likely accumulated where active ice lobes were stable long enough for debris to accumulate and do not necessarily represent ice stagnation. (See Booth [1990] or Knoll [1967] for a discussion of the temporal and spatial relations of deglaciation, as well as the subglacial depositional model of Booth [1984, 1986, 1990].) Locally divided into:

Qgik **Kames**—Cobble and boulder gravel, gravel, sand, and pebbly sand, and rare lenses of diamicton (mostly flow till or melt-out till from buried sediment-laden ice blocks). The sands are typically dark yellowish gray to gray. Sediments are loose, moderately to well stratified, medium to very thickly bedded, and commonly display till or silt rip-up clasts, crossbedding, cut-and-fill structures, and localized oversteepened or slumped bedding. This unit includes both fluvial and, locally, deltaic kame deposits. Kames were mapped where sedimentary structures, geomorphology, and (or) geologic setting imply lateral ice buttressing. Fluvial kame deposits in the Youngs Creek ice-contact complex grade laterally into or overlie divided kame deltas (unit Qgod) and (or) proglacial lake deposits (units Qgos and Qgl_r), forming coarsening-upward deposits. In other areas, receding or wasting ice impinged upon highlands, leaving more isolated kame deposits.

Qgog **Outwash gravel deposits, undivided**—Bouldery pebble cobble gravel to pebbly sand; loose; massive to crudely bedded; mostly ice-contact deposits including kame outwash bodies, but may include any of the gravelly Vashon recessional facies, such as fluvial outwash (unit Qgof). We were unable to assign a depositional environment to unit Qgog deposits because they are poorly exposed.

Vashon Advance Proglacial and Subglacial Deposits

Throughout the map area, drumlins and flutes show that Puget lobe ice advanced from northwest to southeast. Ice advance over this part of the lowland occurred about 14,500 yr BP and blocked ancient rivers, creating extensive temporary lakes across much of the map area (Mackin, 1941; Booth, 1990). Most mapped advance outwash consists of proglacial-fluvial-deltaic sediments, although some may be kame or other ice-contact deposits, or subglacial ice-tunnel sediments deposited between advancing ice and restricting highlands. A complex series of advance deposits formed in front of the advancing ice as the ice interacted with the steep Cascade foothills near the Vashon ice limit in the southeastern part of the map area. Facies relations among river and delta deposits (unit Qga_v) and lake deposits (unit Qgl_v), as well as their thickness and widespread areal distribution, indicate that one or more large proglacial lakes progressively occupied significant portions of the map area during ice advance (Knoll, 1967; Dragovich and others, 2007, 2009a,c, 2010b, 2011a, 2012).

Advance outwash (average ~$Qm_{40}Qp_{54}PF_6$) and lake deposits are similar to other glacial outwash deposits; advance outwash sediment is polycrystalline quartz-rich and contains a polymictic variety of lithic grain types (unnormalized 60–70%) with less monocrystalline quartz and little or no K-spar versus nonglacial deposits that have a modern or ancient Skykomish River basin provenance (Table 1). Petrographic and geochemical analyses of advance outwash sands indicate a complex provenance involving local, eastern, and northern sources. Bedding in advance outwash and lake deposits generally has a southeast primary dip, reflecting glaciofluvial or deltaic deposition into temporary glacially dammed lakes or into steep-gradient and high-energy braided streams, sloping away from the advancing ice front. Thus, dips of Vashon strata on the geologic map show subtle bedding that sloped away from the ice as foreset beds on deltas or composed the lee side of fluvial bars and probably do not indicate significant tectonic tilting. This differs from the ancient alluvial nonglacial deposits (for example, unit Qc_o), which were originally deposited as subhorizontal fluvial flood deposits.

Qgt_v **Lodgment till**—Unstratified mixture of clay, silt, sand, and gravel (diamicton) and rare lenses of sand and gravel; grayish blue to very dark gray, locally slightly weathered to mottled yellow-brown; sand-silt matrix-supported; unsorted; dense; accreted at the base of the Vashon ice and thus typically displays a friable shear fabric. Clasts are both local and northern-sourced and rounded to subangular. Angular clasts are present where this unit directly overlies bedrock. Till is generally from 5 to 50 ft (1.5–15 m) thick and unconformably overlies advance deposits, older Quaternary deposits, and bedrock. Rare possible Pleistocene alpine tills were observed in Youngs Creek and included in this unit. We place the Vashon

stade glacial ice limit in the easternmost part of the quadrangle (significant site 63M) similar to Booth (1990), who mapped undivided mass-wasting deposits above the ice limit along and directly to the east of the Sultan map area.

Qga_v **Advance outwash deposits**—Sandy and pebbly gravel, sand and cobble gravel, and local silt interbeds. Sands are typically dark green-gray, weathering to yellowish brown, light yellowish brown, or pale brown. Sediments are dense and typically well sorted and stratified in thin to very thick beds with local (laminated) silt interbeds, rip-up clasts, deltaic and bar foreset beds, cut and fill structures, and rare ice-shear structures. Advance outwash is complexly interlayered with, conformably overlies, or may locally underlie glacial-lake deposits (unit Qgl_v). Unit Qga_v is most commonly overlain by Vashon lodgment till (unit Qgt_v) along a sharp contact. In the southeastern part of the map area, widespread thick sequences of advance outwash and lake deposits locally contain well-exposed, high-amplitude deltaic foreset beds (significant sites 20Q and 20W (sec. 27, T27N R8E, and sec. 35, T29N R8E, respectively). Composite sections of fluvial-deltaic advance outwash and glacial-lake deposits are fairly thick where fluvial-deltaic deposits prograded into restricted proglacial lakes during ice advance. Radiocarbon dates for this unit from south and west of the map area are 14,450 to 14,560 yr BP (Porter and Swanson, 1998; Associated Earth Sciences, Inc., 2003; Dragovich and others, 2007).

Qgl_v **Advance glaciolacustrine deposits**—Silt, clayey silt, pebbly silt, and diamicton, locally with very thin to thick beds of sand. Sediment is stiff to hard or dense to very dense and typically contains scattered dropstones and beds or lenses of massive till-like diamicton that may be iceberg melt-out till or flow till. Stratification and sorting vary, and sediments are massive to thinly bedded, laminated, or varved. Some exposures are mostly diamicton with thin, wispy interbeds of silt or laminated silt and sand. Unit Qga_v typically overlies unit Qgl_v regionally, but unit Qga_v underlies thick successions of unit Qgl_v in some areas; elsewhere, the two units are complexly interbedded, particularly in the southeastern part of the map area where complex thick expanses of Vashon advance outwash are mapped. Some outcrops expose contorted or folded bedding, sand dikes or other liquefaction features. Inclined to recumbently folded sand, silt, and clay beds were found at significant sites 11S (sec. 35, T27N R8E), 12B (sec. 3, T26N R8E), 15U (sec. 10, T26N R8E), 20L (sec. 27, T27N R8E), 31B (sec. 19, T27N R8E), and 59J (sec. 13, T27N R7E), most in the southeastern part of the map area or along Youngs Creek.

Observed folds typically verge east-southeast, subparallel to the Vashon ice-flow direction, and thus have an orientation and geometry consistent with a glacial ice-shear origin; similarly Knoll (1967) noted "overridden and deformed proglacial lake clays" in the area. Conversely, we observed probable Quaternary faults in Youngs Creek at significant sites 31D, 31G, 31H, and 31L (sec. 24, T27N R7E) where unit Qgl_v is likely tectonized into unit Qtz by apparently discrete fault zones. (See Appendix E and *Fault Nomenclature, Activity, and Structures* for discussion of neotectonic faults and correlation of the Duvall earthquake epicenter with the CCFZ.) We obtained an infinite radiocarbon age (>43,500 yr BP) from a wood fragment in unit Qgl_v at age site 31E (sec. 24, T27N R7E; Appendix A). The rounding of this compressed and carbonized wood fragment in laminated silt and sand with scattered gravel suggests a detrital origin and derivation from older Quaternary strata by proglacial erosion during Vashon ice advance in the late Pleistocene. Unit Qgl_v includes some of the transitional beds of Booth (1990) and correlates with Lawton Clay mapped elsewhere in the Puget Lowland. (See Pessl and others [1989] for a regional description of the 'transitional beds'.)

Pre-Fraser Glacial and Nonglacial Deposits

Qco_l **Sediments of the Olympia nonglacial interval, local facies**— Boulder to pebble gravel, sand with lesser silt and clayey silt with local peat and organic sediments; informally referred to as "Olympia beds" in this pamphlet. Sands are moderately weathered to yellowish to orangish brown or yellowish to olive gray. Sediments are dense, thinly to very thickly bedded, and well stratified and sorted. Subhorizontal, very thick beds of channel gravel with bar and cut and fill structures and crossbedding are common. Sands (SiO_2 ~66–75%) are lithic rich and have a local source similar to adjacent Holocene Youngs–Elwell Creek alluvium. Sands contain significant Tertiary Mount Persis (unit Evs_p) volcanic clasts (35–60%) and plagioclase, and fewer but appreciable polycrystalline quartz, granitic lithic grains, hornblende, and

pyroxene grains with some metasandstone and meta-argillite derived mostly from local mélange belt rocks (unit KJm$_w$). May also contain minor monocrystalline quartz, epidote, high-grade metamorphic and sedimentary lithic grains, and little to no K-spar. Unit Qc$_{ol}$ is exposed in the central to northwestern part of the map area, mostly as cutbanks along Youngs–Elwell Creek and represent ancient, relatively steep-gradient fluvial deposits. The composition, distribution, and stratigraphy indicate a depositional setting analogous to the modern Youngs–Elwell Creek fluvial system and similar to unit Qc$_{ol}$ in both the Carnation and Lake Joy quadrangles, which Dragovich and others (2010a,b, 2012) suggested was ancient alluvium deposited by westerly flowing secondary streams or rivers.

We obtained a radiocarbon age of 22,020 ±100 yr BP at age site 31AB and IRSL age of 39.8 ±1.94 ka at nearby age site 43D from unit Qc$_{ol}$ along Elwell Creek (sec.13, T27N R7E, and Appendices A and B). Dragovich and others (2012) obtained a radiocarbon age of 30,550 ±190 yr BP from organic sediments in unit Qc$_{ol}$ ~2 mi (3.2 km) directly south of the southeast corner of the Sultan quadrangle along North Fork Tolt River; they speculated that unit Qc$_{ol}$ in the Lake Joy and Carnation quadrangles likely formed broad alluvial fans similar to the modern Tolt River fan at Carnation, where the Tolt meets the Snoqualmie River. This stratigraphic arrangement is similar to the apparent interbedding of ancient Youngs–Elwell Creek alluvium (unit Qc$_{ol}$) with ancient Skykomish River alluvium (unit Qc$_o$) near the present intersection of Elwell Creek with the Skykomish River as shown on Cross Section A. (See multiple radiocarbon dates and 17.1–73.3 ka OSL/IRSL ages reported with the description of unit Qc$_o$ below.)

Qc$_o$, Qc$_o$?

Sediments of the Olympia nonglacial interval, ancient Skykomish River facies—Sand, sandy silt, silty sand, and silt with some clay, organic silt-clay, and minor peat with few gravel beds; typically yellowish or grayish brown or brown-gray with distinctive dark grayish orange oxidation; dense; laminated to very thickly bedded and well stratified. Unit Qc$_o$ contains charcoal, disseminated detrital organic matter, trough-and-ripple crossbedding, graded beds, sand dikes, chaotic or folded bedding, and flutes with rare dish structures. Thick exposures of orangish well-bedded sand and silt (fluvial overbank deposits) that form thick, upward-fining pebbly sand–sand–silt sequences typical of meandering river systems are common. Lenticular beds of sand and gravel represent channel deposits with originally sub-horizontal floodplain overbank silt and sand deposits. Unit Qc$_o$ is the ancient Skykomish River alluvium mapped in the Skykomish valley around Monroe and areas to the west (Dragovich and others, 2011a,b) and is compositionally very similar to the ancient Snoqualmie River alluvium ($Qm_{40\text{-}82}Qp_{10\text{-}46}PF_{8\text{-}26}$) of Dragovich (2007) and Dragovich and others (2007, 2009a,b,c, 2010a,b, 2011). Compared to glacial deposits, ancient Skykomish River basin provenance (SP; Table 1) alluvial sands contain more K-spar (8–10%) and limited amounts of polycrystalline quartz and have the same SP signature as units Qc$_{pf}$, Qc$_{ws}$, and Qc$_h$ mapped in adjacent quadrangles. Sands (72–74% SiO_2) from this unit are geochemically similar to felsic compositions and were predominantly derived from an intermediate to slightly primitive arc source with mixing from older accreted sedimentary and metamorphic sources (Appendix C; Dragovich and others, 2010a,b, 2011b). Multiple Olympia bed ages from 17,150 yr BP to >44,020 yr BP were obtained previously by Associated Earth Sciences (2001, 2002, 2004, 2007) and Dragovich and others (2007, 2009a,b,c, 2010a,b, 2012) in quadrangles south and southwest of the map area, where SP beds were assigned to the Olympia nonglacial interval (~15–60 ka).

Dragovich and others (2011a,b) also obtained radiocarbon ages of 17,500 ±80, 18,730 ±110, 19,920 ±130, 24,790 ±170, and >43,500 yr BP and two OSL ages of 50.5 ±3.53 and 51.1 ±3.84 ka from the Monroe quadrangle directly west of the Sultan quadrangle. Most important are the age estimates of 51.1 ka (OSL age and infinite radiocarbon site 10-24D) and 24,790 ±170 yr BP (infinite radiocarbon site 10-49E along the western edge of the map area directly south of the Monroe fault (sec. 11, T27N R7E; Appendix A). A comparison of the various elevations of the ancient Skykomish River alluvium (unit Qc$_o$) relative to the mapped (potentially active) Monroe fault anticline and syncline structures (Cross Sections A and B) implies likely neotectonism across these structures. The distribution, structural geometry, and elevation of Olympia beds around the Skykomish River suggest uplift of unit Qc$_o$ along the proposed Monroe fault. For this study, we obtained unit Qc$_o$ IRSL ages south of the Skykomish River of 73.3 ±2.67, 36.8 ±1.47, and 24.5 ±1.31 ka at sites 44B and 44D (secs. 11-12, T27N R7E) and 44E (sec. 7, T27N R8E) respectively, as well as radiocarbon ages 18,020 ±70, 21,890 ±80, and 23,760 ±100 yr BP at age sites 102A (sec. 9, T27N R8E) and 31AE and 44A (sec. 13, T27N R7E), respectively (Appendices A

and B). We obtained an OSL/IRSL ages of 22.9 ±2.00 to 23.8 ±1.83 ka at age site 44A, generally consistent with our radiocarbon age of 23.76 ka at this site (Appendices A and B). Our new OSL age of between 30 and 215 ka from unit Qco?, directly west of the Sultan River and north of the Skykomish River at age site 45A (sec. 31, T28N R8E) was sampled from the core of the Monroe syncline (Appendix B). We tentatively assign these nonglacial fluvial deposits to the Olympia nonglacial interval (Olympia beds), but acknowledge that these sediments in the core of the Monroe syncline might be ancient alluvium correlative with the Whidbey Formation. See unit Qco? east of the Sultan River in the northwest of part of the map area. Olympia beds occupy the core of the Monroe syncline in the Monroe quadrangle directly west of the map area (Dragovich and others, 2011a,b); however, the elevation of the Olympia beds in the core of the Monroe syncline in the Sultan quadrangle implies perhaps extreme tectonic dislocation or uplift and thus further age dating may indicate a correlation with the Whidbey Formation for these nonglacial fluvial deposits.

Our new data support earlier contentions of Dragovich and others (2011a,b) that: (1) the elevation difference of about 420 ft (~128 m) between ancient SP alluvium (unit Qco) exposed along the present Skykomish River and that perched across the limbs of the Monroe anticline is at least partially the result of folding and uplift across the Monroe fault and anticline, suggesting a potentially active structure; (2) the orientation of bedding in unit Qco and pre-Fraser SP deposits (unit Qcpf) in the area north of the Skykomish River indicates folding around the proposed Monroe syncline. (See *Pleistocene Alluvium and Quaternary Structures* and Cross Section A.) Olympia beds include some of the transitional beds of Booth (1990) and correlate with the deposits of the Olympia nonglacial interval of Pessl and others (1989).

Qcpf **Pre-Fraser continental nonglacial deposits, ancient Skykomish River facies, undivided (Pleistocene)**—Sand, silt, clay with locally some organic matter and peat, and lesser pebbly sand and gravel deposited prior to the Fraser glaciation; sands typically yellow-brown-gray, weathering to a distinctive orange-gray or light yellowish brown or gray; dense; laminated to very thickly bedded and mostly well stratified; may contain charcoal, disseminated organic matter, trough-and-ripple crossbedding, and graded beds; liquefaction features observed in most outcrops and include sand dikes, flames, and distorted or destroyed? bedding (Dragovich and others, 2011a,b, 2012; Appendix E). Petrographic inspection of several sand samples revealed that the deposits contain significant monocrystalline quartz (≤25%), K-spar, and lesser but significant hornblende, pyroxene, mica, and granitic lithic grains. Some sands contain a higher percentage of volcanic and other lithic grains and polycrystalline quartz due to mixing of ancient Skykomish River alluvium with local alluvium, such as along alluvial fans or river cutbanks. This dual composition is observed at age sites 45A and 45B (sec. 31, T28N R8E), where adjacent SP and SP 'transitional' beds are documented both petrographically and geochemically (see *Geochemistry of Bedrock and Quaternary Sand Deposits* and Appendices B and C). Other beds at this site contain the distinctive ancient SP composition, with significant monocrystalline quartz, K-spar (5–10%), and lesser but significant hornblende, pyroxene, and mica. As in the quadrangles directly south and west of the map area (Dragovich and others, 2010a,b, 2011a,b, 2012), unit Qcpf is tentatively inferred to be 250 to 450 ft (76–137 m) thick in the Monroe syncline, where thick successions of sand and silt with some clay and a few beds of gravel are tentatively correlated with unit Qcpf. For example, some wells, such as W66 on Cross Section A, apparently lack diamicton or hardpan, commonly correlated with glacial intervals, and contain peat, wood, sticks, and logs indicative of thick nonglacial fluvial deposits in the subsurface along what we informally term the "Monroe synclinal basin". (See Dragovich and others [2011a,b] for mapping, structure, geophysics, and age constraints along the Monroe syncline directly east of the Sultan quadrangle.) Similar to modern Snoqualmie River deposits, unit Qcpf stratigraphic style and the dominance of sands and silts suggest deposition as thick fining-upward gravel-sand-silt sequences. This is typical of meandering river systems, where thick successions of thinly bedded sand and silt likely represent overbank deposits similar to the other SP units, including modern alluvium. Unit Qcpf deposits compositionally match modern and ancient Skykomish and Snoqualmie SP alluvial units and are likely correlative with units such as the Olympia beds (unit Qco), Whidbey Formation (unit Qcws), or the Hamm Creek formation of Troost and others (2005)(unit Qch) or older nonglacial units as previously mapped to the south, southwest, and west (Dragovich and others, 2010a,b, 2011a,b, 2012). (See *Geochemistry of Bedrock and Quaternary Sand Deposits* and Table 1.)

Similar to radiocarbon ages from unit Qc_{pf} strata in the Monroe quadrangle (Dragovich and others, 2011a,b), we obtained a radiocarbon age of >43,500 yr BP from a small wood fragment at age site 41P (sec. 1, T27N R8E) and an infinite IRSL age of >300 ka from overbank facies of silty fine- to medium-grained sands at age site 45B north of the Skykomish River and directly above the west bank of the Sultan River (Appendices A and B). The silts and pebbly sands at this site are intensely liquefied and display contorted and discontinuous bedding common to the unit regionally. We correlate subaerial exposures of unit Qpf of Booth (1990) north of the Skykomish River with either units Qc_{pf} or Qc_o on the basis of field, age, petrographic, geochemical, and other observations.

Qgn_{pf} **Pre-Fraser glacial and nonglacial deposits, undivided (Pleistocene to Pliocene?)(cross sections only)**—Dense to very dense gravel, boulder gravel, sand, silt, clay, and diamicton; may locally contain peat or organic sediments. The few wells or boreholes that penetrated this unit drilled into early(?) Pleistocene glacial strata containing diamicton or hardpan below organic-bearing nonglacial SP strata of unit Qc_{pf} in the subsurface. Dragovich and others (2007, 2009c, 2010a,b, 2012), Booth (1990), and Knoll (1967) also describe outcrops of old and undivided glacial and nonglacial deposits elsewhere in the Snoqualmie and Skykomish valley area, including the highly weathered tills and outwash in unit Qgn_{pf} of Dragovich and others (2009a,b) south of the map area.

Tertiary Volcanic, Intrusive, and Sedimentary Rocks

Ts **Sedimentary or volcaniclastic rocks, undivided (Miocene to Eocene)(cross sections only)**—Rocks likely correlative with the distal volcaniclastic rocks of Mount Persis, rocks of Bulson Creek, Blakeley Formation, or Miocene sedimentary rocks; see units Evc_p, ΦEc, ΦEn and Mvc in the Monroe area for further descriptions (Dragovich and others, 2011a,b, 2010a,b). This unit is shown only on the cross sections, at depth within the Monroe syncline (see *Isostatic Gravity and Aeromagnetic Analyses*).

$Eigd_y$ **Youngs Creek intrusive complex (Eocene)(cross section B only)**—Massive, medium-grained granodiorite (~66% SiO_2); dark or light bluish gray, weathering to yellowish gray. Locally contains tabular mafic enclave bodies (2–12 cm wide) of fine-grained gabbro. Unit $Eigd_y$ granodiorite is composed of euhedral to subhedral and mostly equigranular plagioclase (~35%), K-spar (~20%), and quartz (~10–20%), and minor mildly to strongly chloritized hornblende with scattered opaque minerals and local clinopyroxene; moderately to strongly hydrothermally altered with conspicuous chlorite ± epidote and secondary actinolite and K-spar replacing plagioclase was observed locally. This stock was mapped by Tabor and others (1993) at the headwaters of Youngs Creek directly to the east of the map area in the Gold Bar quadrangle; we informally name this stock the Youngs Creek intrusive complex. We also tentatively include small intrusive bodies that intrude the Western mélange belt north of the Monroe fault in the northeast part of the map area (Cross Section B) in the complex. These bluish gray rocks are petrographically similar to the stock and contain hypidiomorphic granular and fine- to medium-grained plagioclase phenocrysts (≤4 mm) with interstitial quartz (10–20%), augite, and some hornblende with scattered opaque minerals. Reconnaissance mapping of this stock combined with geophysical observations imply that a mafic gabbro is part of the complex (see *Isostatic Gravity and Aeromagnetic Analyses*). The garnet-bearing hornfels across the easternmost-central part of the map area is consistent with new gravity data that suggests the Youngs Creek intrusive complex shallowly underlies the east-central part of the quadrangle.

We obtained U-Pb zircon ages of 39.35 ±0.31 and 42.99 ±0.26 Ma from a rock quarry in the stock 1.62 mi (2.6 km) directly east of age site 11G and the Sultan quadrangle's eastern boundary (sec. 26, T27N R8E). As illustrated in Appendix F, this bi-modal zircon age population is likely due to intrusive activity over an extended range of time. As shown on the correlation diagram on the map sheet, this age is similar to the 43.7 ±1.0 Ma age of pumiceous tuff in the adjacent Monroe quadrangle (Dragovich and others, 2011a,b). The age, field relations, composition, and geochemistry of this body indicate that the stock is (1) likely a major sub-volcanic intrusive source for the volcanic rocks of Mount Persis of Tabor and others (1993) similar to the 46 Ma unit Ei_p, and (2) not correlative with the younger Index batholith as suggested by Tabor and others (1993). The 47 Ma K-Ar Fuller Mountain plug of Tabor and others (1993) south of the study area may also be an intrusive center for the Mount Persis unit. (See additional

age information in description of unit Evs_p and *Geochemistry of Bedrock and Quaternary Sand Deposits*.)

Evs_p **Volcanic rocks of Mount Persis of Tabor and others (1993), undivided (Eocene)**—Interbedded andesitic to basaltic flows, and lesser andesitic to rhyolitic tuff and (tuff) breccia, volcanic and tuffaceous sandstone and siltstone, lahar deposits, volcanic conglomerate, shale, organic-matter-rich siltstone, and coal (Tabor and others, 1993; Dragovich and others, 2009a,b, 2010a,b, 2011a,b, 2012). Flows are mostly andesite or basaltic andesite, but locally include dacite and basalt. Volcanic sedimentary rocks are moderately to well stratified and typically contain tuff or breccia beds. Within the Sultan quadrangle, rocks are locally strongly altered, particularly near tectonic zones (units tz and tz_h), but also away from fault zones, suggesting that some alteration is related to magmatic fluids from shallow intrusion of $Eigd_y$ and Ei_p intrusive bodies along the eastern part of the map area (Cross Section B). Regionally the Mount Persis unit unconformably overlies the Western mélange belt (Cross Sections A and B; Tabor and others, 1993; Danner, 1957). Directly to the southwest and west of the map area, along the easternmost part of the Seattle basin and within the broad SWIF, the Mount Persis unit underlies younger Tertiary strata (Dragovich and others, 2007, 2009a,b, 2010a,b, 2011a,b; Sherrod and others, 2008). The transition from proximal to distal Mount Persis unit volcanism occurs in the adjacent Lake Joy and Monroe quadrangles (Dragovich and others, 2011a,b, 2012) where the volume of distal volcanic sedimentary rocks and mafic flows locally increases. (See units Evc_p and Evb_p). Although the Mount Persis unit likely originally thinned to the west and south where distal volcaniclastic and tuffaceous strata interbedded with mafic flows, it now thins to the east across the current map area because of uplift, exhumation, and subaerial erosion of the Mount Persis unit to the east; this is similar to relations directly south of the map area where the Mount Persis unit thins within the Tokul Creek fault zone (Dragovich and others, 2012).

Tabor and others (1993) assigned a late Eocene age to the Mount Persis unit on the basis of (1) an apatite fission-track age (47.0 ±4.0 Ma; age site USGS 33, sec. 23, T27N R8E), (2) a hornblende K-Ar age (38.1 Ma), and (3) their observation that the Mount Persis unit is intruded by the Index batholith (34 Ma) and mafic dikes (33 Ma) northeast of the map area. Dragovich and others (2009a,b, 2011a,b) obtained U-Pb zircon ages of 36 ±2.3 Ma and 43.7 ±1.0 Ma from tuff in the adjacent Snoqualmie and Monroe quadrangles, respectively. Available age and stratigraphic information suggest that Mount Persis volcanism spans millions of years (~36–47 Ma) and involved several intrusive centers. (See correlation diagram on map sheet.) Identified intrusive centers include unit Ei_p in the Sultan, Monroe, and Lake Joy quadrangles, as well as the Youngs Creek intrusive complex of this study and perhaps the 46.6 ±2.0 Ma Fuller Mountain plug of Tabor and others (1993). (See Appendix F and units $Eigd_y$ and Ei_p for new U-Pb ages). Locally divided into:

Eva_p, Evd_p **Andesite flows**—Andesite; may locally include dacite or basaltic andesite flows; medium bluish gray to dark gray, weathered or altered to dark reddish gray or brown-gray, maroon-gray, or yellow-brown-gray. Unit Evd_p dacite flows are generally similar to unit Eva_p, but are lighter gray and contain quartz phenocrysts. Andesite flows are typically massive, but locally exhibit strong flow structure, including aligned phenocrysts, microlites, amygdules, or vesicles, flow breccia, and altered flow tops; well-formed columns are rare. These two-pyroxene flows contain phenocrysts of plagioclase commonly with augite ± hypersthene and rare quartz microphenocrysts. Some flows contain (chloritized) hornblende, and a few also contain (chloritized) biotite. Glomeroporphyritic textures and oscillatory-zoned plagioclase are common. Dark andesite flows with aligned microphenocrysts of plagioclase in a fine-grained holocrystalline groundmass containing disseminated opaque minerals are noteworthy in this quadrangle (see unit Eva_{pd} below). Locally, rocks are moderately to strongly propylitically altered, particularly near tectonic zones (units tz and tz_h), and contain secondary calcite, epidote, chlorite, sercite, and quartz with various sulfide minerals including pyrite. Flow units are 30 to 100 ft (9–30 m) thick (Cross Sections A and B). Very thick flows are likely compound lava flows that filled paleovalleys in volcanic highlands (Dragovich and others, 2010a,b, 2011a,b, 2012). Tabor and others (1993) report a fission track age of 47 Ma from age site USGS 33 along the east-central edge of the quadrangle, which is similar to the age of

46 Ma for the Drunken Charlie intrusive complex (unit Ei_p) and 47 Ma for the Fuller Mountain plug of Tabor and others (1993) along the easternmost edge of the Snoqualmie quadrangle.

Eva_{pd} **Dark basaltic andesite flows**—Basaltic andesite to andesite flows; may include basalt flows; typically dark gray to bluish gray to very dark gray, weathered or altered to reddish gray, reddish brown, or brownish yellow. Flows are typically fine grained but show subtle flow structure defined by aligned phenocrysts and amygdules. Thick compound flows are common and well-formed columns and pillows are rare. Unit Eva_{pd} contains phenocrysts of plagioclase and augite ± hypersthene with significant disseminated opaque grains that color the rock dark gray. Some flows have (chloritized) hornblende and rare biotite, and a few flows have sparse blocky plagioclase phenocrysts (~1–2 mm) surrounded by microlite crystals. Unit Eva_{pd} is typically almost holocrystalline and has glomeroporphyritic microphenocryst patches and chloritized or sericitized interstitial glass. We separated unit Eva_{pd} from basalts (unit Evb_p) and andesites (unit Eva_p) in the field by rock color and the amount and composition of the phenocrysts. However, outcrops of the mafic flows are megascopically similar. The dark, fine-grained rocks are difficult to classify in the field, and thus many unit Eva_{pd} exposures had to be classified via petrographic and geochemical analyses. Also, because of this similarity, some basalt flows may have been mapped as unit Eva_{pd}. Although most of these dark volcanic rocks are demonstrably volcanic flows, we cannot exclude the possibility that some are dikes or sills, particularly in areas where outcrop exposures are poor.

Evb_p, Eib_p **Basalt flows and dikes**—Basalt to basaltic andesite; dark gray or reddish or greenish gray; weathered or altered to very dark grayish brown or light olive-brown. The flows are typically fine-grained and massive, but locally show flow structure defined by aligned phenocrysts and amygdules (≤1.2 in. or 3 cm) or vesicles. Thick compound flows are common, and columns, pillows, scoria, and hyaloclastite are observed regionally in Mount Persis unit basalt flows. We mapped a few well-exposed basaltic dikes in the eastern and southeastern part of the map area (unit Eib_p). Flows contain phenocrysts of plagioclase and augite ± hypersthene, typically with (chloritized) hornblende. Unit Evb_p is glassy to holocrystalline and has glomeroporphyritic microphenocryst patches; microscopic flow alignment is common. Basalt flows are dark and generally lack megascopic plagioclase phenocrysts. Many of the wells located directly south of the Monroe fault on Cross Section A in the northwestern part of the map area report thick to very thick basalt flows in the subsurface. This subsurface information, combined with limited field evidence and geophysical data, indicates that distal Mount Persis unit basalt flows are interbedded with volcaniclastic fluvial deposits (unit Evc_p) south of the Monroe fault on Cross Section A in the northwestern part of the map area. This relationship suggests that the lower part of the Mount Persis unit in this area preserves distal mafic flows and fluvial volcanic sediments. (See *Isostatic Gravity and Aeromagnetic Analyses* in this pamphlet and Figs. 1 and 2 on map sheet.)

Evt_p **Tuff**—Variable composition including crystal and lithic vitric, crystal lithic, lithic, and vitric lithic andesitic to dacitic (59–67% SiO_2) and rhyolitic tuff with lesser lapilli tuffs and lapillistone, variable but typically light to dark gray to bluish or greenish gray to light yellowish brown. Lithic tuff beds are typically greenish. Tuff beds are locally semi-vesicular and commonly form thick to very thick beds between flows or breccia beds; they are typically massive, but some beds are crudely compositionally banded (gradations of crystal, glass, and lithic contents), and pumice is typically flattened in lapilli tuff beds. Propylitic alteration (generally epidote, chlorite, calcite, sercite ± albite and quartz) of tuff is common. Tuffs are remarkably compositionally and texturally variable between non-pumiceous tuffs, composed of euhedral to anhedral quartz and plagioclase phenocrysts in yellowish to light greenish glass, to felsic or intermediate pumiceous lapilli tuff beds. Non-pumiceous felsic tuff locally contains plagioclase microlites or larger phenocrysts, locally with a few scattered grains of altered pyroxene and rarely hornblende; pumice-bearing tuffs may contain semi-vesicular to non-vesicular andesite and (or) dacite lapilli in a clear to dark variable glass and commonly contain

plagioclase with some quartz grains. Some non-pumiceous tuff beds are distinctly lithic-rich and grade from andesitic to dacitic lapilli tuff to lithic volcanic breccia of unit $Evbx_p$ or occur as tuff beds within volcaniclastic fluvial deposits (unit Evc_p). Excellent exposures of the pumiceous lapilli tuff are at significant sites 5G and 47A (secs. 7 and 5, respectively, T26N R8E). Noteworthy are multicolored lapillistone or lapilli tuff that might be a very thick tuff or tuffaceous sedimentary marker bed deposited at the edge of the Mount Persis unit Eocene basin and before transition of the Monroe fault to a compressional structure (Fig. 2). We observed this possible marker bed at several sites within units tz or tz_h or directly south of the Monroe fault as a basin-marginal lithology in the north-central and northwestern part of the study area. These beds contain a variety of volcanic clast types as well as subrounded metasedimentary grains (≤10%), including a few grains of distinctive radiolarian-bearing metachert, K-spar, and mica eroded from the adjacent Western mélange belt highlands. At significant sites 22C (sec. 11, T27N R7E), 23E (sec. 12, T27N R7E), 51N (sec .8, T27N R8E) and 52R (sec. 17, T27N R8E), these multi-colored beds are tectonized within Monroe fault or McCoy Creek fault zones, forming protomylonite or cataclasite mapped as unit tz.

Dragovich and others (2009a,b, 2011a,b) obtained U-Pb zircon ages of 36 ±2.3 Ma and 43.7 ±1.0 Ma from rhyolitic or pumiceous tuff in the Snoqualmie and Monroe quadrangles, respectively. The 43.7 Ma tuff beds in the Monroe quadrangle are compositionally similar to very thick pumiceous lapilli tuff beds in the Sultan quadrangle. These beds also have an age similar to the Youngs Creek intrusive complex (39–43 Ma), suggesting the complex may be the intrusive source for these felsic tuff beds.

$Evbx_p$ **Volcanic breccia**—Dacitic to andesitic lithic tuff breccia with lesser (crystal) lithic lapilli tuff and minor agglomerate; typically dark green-gray to light gray, but multicolored with red, green, and black to gray volcanic clasts and matrix common; weathers to gray-brown. Breccia beds are generally very thick, massive, and moderately to poorly sorted. Bomb breccias are common in the map area, with maximum clast size varying from 18 to 60 in. (45–180 cm) at significant sites 14P (sec. 19, T27N R8E), 18Q (sec. 22, T27N R8E), 21G (sec. 30, T27N R8E), 30L (sec. 35, T27N R7E), and 54M (sec. 32, T27N R8E), with the largest observed bomb at 31N (sec. 24, T27N R7E). Poorly sorted volcanic breccia interbedded with volcanic sediments (unit Evc_p) at site 21G contains bombs up to 43 in. (110 cm), indicating catastrophic input of breccia into fluvial basins. Pumiceous lapilli tuff beds are generally mapped as tuff (unit Evt_p). However, a few pumiceous tuff breccia beds are compositionally similar to pumiceous lapilli tuff beds and may be coarser-grained equivalents. Some breccia beds contain scattered dark-gray basaltic andesite to basalt clasts, and a few contain minor exotic greenstone, metasandstone, and metachert clasts derived from nonvolcanic sources (Danner, 1957). Unit $Evbx_p$ consists for the most part of very thick pyroclastic flow deposits containing homogeneous dacite fragments, likely resulting from volcanic dome collapse. Some breccia beds are thinner pyroclastic surge deposits in volcanic epiclastic rocks or flow breccia beds in flows. Thin to very thick interbeds of epiclastic volcanic sandstones in a few outcrops show that some very thick breccia units are the result of emplacement of stacked pyroclastic deposits into restricted fluvial basins. Unlike more distal volcanic Mount Persis unit environments, lahars are rare in the map area and included with unit $Evbx_p$. Unit $Evbx_p$ clasts in nearby quadrangles are either (1) two-pyroxene andesites that are petrographically and geochemically similar to the Mount Persis unit andesite flows, or (2) semi-vesicular, light-green dacite clasts (63–70% SiO_2)(Dragovich and others, 2009a,b, 2010a,b, 2011a,b, 2012). As in adjacent quadrangles, breccia clasts in the Sultan quadrangle appear to be mostly augite ± hornblende to plagioclase ± quartz phyric dacite (63–65% SiO_2). Some dacitic breccia may correlate with the extensive hornblende-phyric dacite breccia unit (38.1 Ma) of Tabor and others (1993) to the east of the map area.

Evc_p **Volcaniclastic rocks**—Lithic and feldspatholithic volcanic to tuffaceous sandstone, silty sandstone, and siltstone containing some interbeds of volcanic conglomerate, volcanic pebble conglomerate, tuff, lapilli tuff, breccia, shale, organic siltstone, and coal; generally light

yellowish brown to very pale brown to light bluish gray to greenish gray sandstone, and some dark red to reddish brown to grayish black volcanic siltstone. Volcanic sediments are mostly well to moderately sorted and well stratified and contain angular to subrounded grains; strata vary from massive to medium to thickly bedded. The plane-and-ripple crossbedding typical of fluvial environments is common. Fossil leaves, stems, and fragments of black to brown, carbonized petrified wood are common and consist mostly of fragments of broadleaf trees and stems similar to modern *Equisetum* (Dragovich and others, 2010b, 2012; Danner, 1957). Carbonized petrified logs, some of which are upright relative to sedimentary bedding, are also common. The compositional spectrum of volcaniclastic rock types includes crystal-rich sediments with significant subangular to angular plagioclase, volcanic quartz, and various amounts of fragmental pumice that are likely fluvially reworked crystal-vitric ash-flow tuff; sandstone is dominated by angular microlitic volcanic grains that are likely reworked lithic ash-flow tuff. Most volcaniclastic rocks are rich in angular to sub-rounded volcanic lithic grains and contain abundant basaltic andesite to dacite clasts, but they also locally contain altered volcanic glass, monocrystalline quartz, plagioclase, hornblende, and pyroxene. Danner (1957) described andesitic boulder conglomerates with shale lenses, which are likely fluvial deposits in the Youngs Creek area; most conglomerate contains subrounded clasts dominated by basalt, andesite, and dacite, and, locally, some metachert, jasper, greenstone, and metasandstone.

Dragovich and others (2009b) described unit Evc_p sandstones with a mixed volcanic and Western mélange belt (unit KJm_w) provenance near the structural edge of the Mount Persis unit basin south of the map area; these contain some metachert, metasandstone, greenstone or meta-argillite clasts similar to sandstones directly south of the Monroe fault (Fig. 2). Several volcanic sandstone samples from the area to the south contain the same exotic grains derived from the Western mélange belt highlands, such as radiolarian-bearing metachert. (See unit Evt_p multicolor tuff.) Unit Evc_p likely represents stream deposits within a dissected volcanic highland setting over much of the map area. In this proximal volcanic setting, the lenticular fluvial beds are largely surrounded by more direct volcanic deposits such as flows, tuffs, and breccias. Moderately sorted and massive to crudely graded sandstone and pebbly sandstone beds could be hyperconcentrated flood (lahar runout) deposits resulting from the transformation of pyroclastic flows or volcanic debris flows to more sorted sandy deposits within a fluvial environment. Also, some pumiceous tuff beds could be pyroclastic surge deposits. Although the erodibility of most volcanic sedimentary rocks results in poor surface exposure, subsurface data suggest that volcanic sedimentary rocks are relatively common in the subsurface in some areas (Cross Section A). Stratigraphic relations of unit Evc_p directly south of the Monroe fault along the western edge of the map area suggest a more distal fluvial broad-plain environment where basalt (unit Evb_p) flowed into a more open environment similar to adjacent Monroe and Lake Joy quadrangle depositional models (Cross Section A; Dragovich and others, 2011a,b, 2012).

Ei_p **Drunken Charlie Lake intrusive complex**—Dacite porphyry, dacite and tuff breccia with basaltic andesite or basalt dikes; dacite is medium bluish gray to dark greenish gray; mostly massive porphyry are hypabyssal with fine-grained dacite locally intruding(?) the porphyry. Dacite bodies are locally intruded by mafic dikes. Dacite porphyry is locally brecciated and contains subangular to angular clasts ranging from lapilli to bombs with a local semi-vesicular texture surrounded by fine-grained dacite. Some clast shapes suggest brecciation during intrusion. Other clasts have sub-vertical alignment or are suggestive of vertical flow. Dacite (64% SiO_2) contains euhedral plagioclase (≤4 mm long) with mafic minerals (converted to chlorite or chlorite + calcite) in a glassy clear matrix forming ~30% of the porphyry. Other dacites lack glass. Quartz forms small embayed phenocrysts (≤1 mm) and occurs in the glassy matrix containing microlites of plagioclase, quartz and a few opaque minerals. The complex is locally propylitically altered similar to unit Ei_p mapped in the Lake Joy quadrangle and may be the result of hydrothermal fluids along nearby faults and (or) by deuteric fluids. Composition–contact relations and textures suggest a probable dacitic dome and (or) plug complex similar to

unit Eip complexes mapped in the Lake Joy quadrangle by Dragovich and others (2011a,b, 2012) directly west and south of the map area.

We obtained a zircon U-Pb age of 46.46 ±0.37 Ma from unit Eip at age site 47G (sec. 5, T26N R8E) near Drunken Charlie Lake in the southeastern part of the map area (Appendix F). This age is similar to other Mount Persis unit ages of Tabor and others (1993) including: (1) a zircon fission track age of 47 Ma obtained from an andesite flow at age site USGS 33 along the eastern edge of the map area, and (2) K-Ar hornblende age of 47 Ma for the Fuller Mountain plug south of the study area. These ages provide evidence that the Mount Persis unit is locally as old as ~47 Ma. (See 'Fuller Mountain plug' in unit Eigdy and Mount Persis unit ages in unit Evsp above.)

Mesozoic Low-Grade Metamorphic Rocks (Prehnite–Pumpellyite Facies)

KJm$_W$ **Western mélange belt of Tabor and others (1993), undivided (Cretaceous to Jurassic)**—Dominantly meta-argillite, metasandstone, greenstone, metagabbro, metachert, with metadiabase, metatonalite, slate, phyllite, marble with meta-quartz-diorite, hornblendite, (banded) amphibolite, and rare ultramafite observed regionally (Fuller, 1925; Danner, 1957; Dragovich and others, 2007, 2009a,b,c, 2010a,b, 2011a,b, 2012). Most metasedimentary rocks were deposited as turbidites along an accretionary wedge (Jett, 1986; Jett and Heller, 1988). Although mélange rocks are exposed north of the Monroe fault in the northern part of the map area, geophysical modeling, subsurface data, and mapping indicate that the Mount Persis unit unconformably overlies the mélange belt basement south of the Monroe fault (Cross Sections A and B). Locally divided into:

KJmv$_W$ **Metavolcanic rocks**—Greenstone derived from metamorphosed andesite to basaltic tuff, volcanic flows, and rare volcanic breccia; greenish gray to dark greenish black. Tabor and others (2000) described boudins of metamorphosed quartz-porphyry dikes(?) in faintly foliated greenstone south of the study area. Regionally metamorphosed flows are mostly massive to moderately foliated metabasaltic andesite along with lesser metabasalt or meta-andesite that display rare amygdaloidal texture and pillow structures (Dragovich and others, 2009a,b,c). This unit contains plagioclase and actinolized or chloritized pyroxene phenocrysts in a chloritic matrix and may locally contain minor quartz and opaque minerals. Only the larger greenstone bodies are shown on the map; the thin metatuff interbeds observed in the metasedimentary rocks of the Western mélange belt are not shown. An alkali oceanic island basalt (OIB) provenance is indicated by the geochemistry of one very thick mafic mugearite flow interbedded with metachert in the northeast part of the map area (Appendix C). Available information suggests accretion of OIB seamount provenance to the Western mélange belt during the Jurassic and Cretaceous. Metatuff is mostly calc-alkaline (Dragovich and others, 2009a,b,c).

KJms$_W$ **Metasedimentary rocks**—Marine lithofeldspathic to feldspatholithic subquartzose metasandstone, silty metasandstone, meta-argillite, metatuff, and minor marble and (chert pebble) metaconglomerate; typically greenish gray to dark or bluish gray or gray-green and weathered to brown; meta-argillite typically black or greenish or bluish black to dark gray. Danner (1957) mapped metamorphosed limestone bodies in mélange directly west of the map area. Relict sand and gravel clasts are subrounded to angular; graded bedding and load casts are locally preserved. Very thin to very thick meta-argillite beds are interbedded with metasandstone, forming much of the mélange belt matrix that is easily eroded and rarely exposed. This deformed metasedimentary matrix hosts intensely folded rocks with transposed bedding. Conversely, less-deformed homoclinal sequences of well stratified metasedimentary rocks are locally very thick and well exposed in McCoy Creek at significant site 51J (sec. 7, T27N R8E). Metatuff interbeds contain relict plagioclase, pyroxene, and quartz phenocrysts in a chloritic matrix and attest to a volcanic contribution to the Western mélange belt rocks. Rocks are typically moderately foliated and partly recrystallized, and they commonly have a synkinematic metamorphic fabric defined by aligned white mica and moderately aligned relict

clasts. Metamorphic minerals are white mica, actinolite/tremolite, epidote or clinozoisite, chlorite ± pumpellyite, and prehnite. Relict clasts include mixtures of plagioclase, monocrystalline quartz, chert (locally enclosing radiolarians), polycrystalline quartz, and K-spar with volcanic and sedimentary lithic clasts. Detrital biotite or muscovite is locally conspicuous, as are rip-up clasts of meta-argillite.

Most of the petrographically examined rocks conform to the cherty petrofacies, and only locally the arkosic or lithic petrofacies, of Jett and Heller (1988). (See petrofacies mapping of Tabor and others [1993] and Jett [1986] and metasandstone geochemistry of Dragovich and others [2009b,c] for further information.) These metasedimentary rocks were deposited as turbidites along an accretionary wedge, although *Equisetum* fossils found by Dragovich and others (2009a) indicate a local shallow marine or terrestrial environment. C. D. Blome (USGS, *in* Walsh, 1984) reported Cretaceous or Jurassic radiolarians (*Sethocapsa*?) from metasandstone south of the study area. Dragovich and others (2009a,b) obtained a minimum U-Pb detrital zircon population age of ~96 Ma from feldspathic meta-sandstone south of the study area. This minimum population age confirmed that the turbidites are as young as mid-Cretaceous with accretionary mélange-belt formation and sedimentation probably ending ~96 Ma. The age is consistent with other regional age and structural considerations that indicate thrusting of the Northwest Cascade System and the structural emergence of mélange belts at ~90 Ma (Tabor, 1994; Dragovich and others, 2009a,b). A U-Pb detrital-zircon age population peak of ~147 Ma was also found, along with lesser amounts of detrital grains as old as Triassic (230 Ma), indicating that the source rock(s) for the turbidites is Mesozoic.

$KJmc_w$ **Metachert**—Metachert locally with meta-argillite interbeds; mapped separately from the metasedimentary rocks where very thick; maroon to reddish or white. Commonly banded, with bedding varying from undeformed to strongly contorted; generally occurs as streamlined pods with scaly margins. Tabor and others (1993, 2000) reported Cretaceous to Jurassic ages for the Western mélange belt, including a late Jurassic radiolarian age from a metachert bed at age site USGS 4F (sec. 16, T27N R8E) in the northeast section of the quadrangle and south of the Skykomish River, as well as a radiolarian age directly south of the map area (Dragovich and others, 2012).

$KJigb_w$ **Metagabbro (cross sections only)—**Metagabbroic greenstone as described in Tabor and others (1993) and Dragovich and others (2011a,b, 2012); occurs as tectonic lenses in the mélange as modeled in the subsurface.

Holocene to Tertiary Tectonic Zones

tz, tz_h, Qtz **Tectonic zone**—Cataclasite, fault breccia, clay-rich fault gouge, protomylonite, or moderately to strongly slickensided, fractured, and veined rocks in fault zones; greenish, yellowish to orangish to variously colored, mottled, and altered. Dragovich and others (2007, 2009a,b,c, 2010a,b, 2011a,b, 2012) map similar tectonic zones along faults west, southwest, and south of the map area. Unit tz_h represents mappable zones of hydrothermal alteration within tectonic zones that are common in the map area; these zones are yellowish or reddish brown, white, or red or dark red, and principally represent propylitic alteration mineral assemblages but rarely include phyllic and potassic zone assemblages. Alteration minerals include chlorite and calcite, locally with some opal or secondary quartz, zeolites, white mica, biotite, clays, and K-spar. Sulfide mineralization is locally conspicuous. Most unit tz_h alteration is structurally controlled (for example, along the CCFZ), but some may also be related to hydrothermal alteration associated with Tertiary intrusions outside tectonic zones, such as near units Ei_p and $Eigd_y$ (see *Isostatic Gravity and Aeromagnetic Analyses* and Cross Section B). Quaternary tectonic zones (unit Qtz) are only mapped around significant sites 31D, 31G, 31H, and 31L, where unit Qgl_v appears to be faulted near the main strand of the CCFZ along Elwell Creek (Appendix E). This tectonic deformation is characterized by high-angle fractures and (or) discrete faults with bedding offsets in Pleistocene deposits. Quaternary deformation is also inferred in the subsurface on Cross Sections A and B, adjacent to active or potentially active faults, as well as around folds that appear to deform Quaternary sediments such as the

Monroe anticline and syncline. (See *Fault Nomenclature, Activity, and Structure* and *Pleistocene Alluvium and Quaternary Structures*.)

FAULT NOMENCLATURE, ACTIVITY, AND STRUCTURES

Geologic mapping of the Sultan quadrangle continues efforts to better understand the southern Whidbey Island fault zone (SWIF) and its relation to the Cherry Creek (CCFZ) and Monroe fault zones. West of the map area, Sherrod and others (2008) extended the SWIF eastward from the Whidbey Island area to the Maltby quadrangle west of the Sultan area (Fig. 1). In a series of geologic maps, Dragovich and others (2007, 2009a,b,c, 2010a,b, 2011a,b, 2012) extended the Rattlesnake Mountain fault zone (RMFZ) from the North Bend, Snoqualmie, and Fall City quadrangles northwestward through the Carnation, Monroe, and Lake Joy quadrangles and correlated this broad fault zone with the SWIF. In these reports, we map the SWIF as a likely strike-slip fault zone comprising several active or potentially active segments. Some of the segments align with probable active fault strands mapped by Sherrod and others (2008) to the west. Major faults of the RMFZ–SWIF previously mapped west to south of the map area include the Cherry Valley fault (CVF), CCFZ, Snoqualmie Valley faults, Rattlesnake Mountain faults, and Carnation faults. Dragovich and others (2010a,b) correlated the main strand of the RMFZ with the Cottage Lake lineament of the SWIF of Sherrod and others (2008). The SWIF likely traverses the southwestern part of the Lake Joy map area and western part of the Monroe quadrangle directly south and west of the present study area.

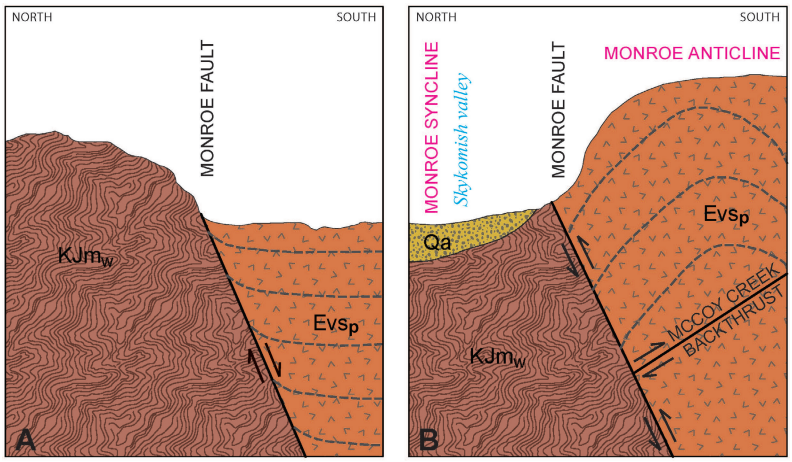

Figure 2. Diagrammatic cross section of the Monroe fault showing inferred Tertiary kinematic history. **A**. Eocene north–south extension across the Monroe fault produced the Mount Persis unit volcanic basin. Some Mount Persis unit beds have a partial Western mélange belt provenance consistent with basin-marginal deposition. **B.** Post-Eocene kinematic reversal of the Monroe fault and rejuvenation as a compressional reverse fault; McCoy Creek backthrust and the Monroe anticline also help accommodate compression. This rejuvenation initiated in the Oligocene to Miocene and likely accompanied the onset of north–south compression in the Puget Lowland and may be currently ongoing. Rejuvenation explains the younger Mount Persis unit over the older Western mélange belt fault arrangement and probably resulted in the formation of the Monroe synclinal basin.

Our current mapping confirms that the contact between the Mount Persis unit and the Western mélange belt directly south of the Skykomish River is a well-exposed reverse fault, which was originally suggested by Danner (1957) and was termed the Monroe fault by Dragovich and others (2011a,b)(Cross Section A). Reverse faults within the Lake Joy, Carnation, and Monroe quadrangles include the Carnation, Monroe, and Fontal Road faults (Dragovich and others, 2010b, 2011a,b, 2012). Folds associated with the reverse faults, including the Tolt River anticline (Dragovich and others, 2012), are likely flexural-slip, with axial traces subparallel to the faults. The Monroe anticline and syncline are mapped from the Monroe quadrangle into the present map area and are similarly interpreted as flexural-slip folds accommodating the current north–south compression of the Puget Lowland. We base this interpretation on the (1) parallelism of structures, (2) geophysical data, and (3) kinematic field data for the fault zones. Reverse fault kinematic indicators along the Carnation fault in the Lake Joy quadrangle (Dragovich and others, 2012) and along the Monroe fault in this study area (for example, significant site 22C) include shallow-dipping, very thick and well-exposed foliated protomylonites or cataclasites with down-dip lineations. The northerly vergence of the reverse faults in the Monroe quadrangle contrasts with the southerly vergence of the Carnation faults in the Carnation and Lake Joy quadrangles, possibly reflecting a regional pop-up or positive flower structure within or directly east of the SWIF (Dragovich and others, 2011a,b, 2012)(Fig. 1). We tentatively interpret these faults as restraining bend duplex structures within the SWIF (Dragovich and others, 2012), but how this pop-up relates to regional tectonics is unresolved. The McCoy Creek fault is interpreted as a backthrust to the Monroe reverse fault. Evidence for a backthrust was observed at significant site 52R along McCoy Creek, where south-vergent mylonites are paired with a northerly-dipping stretch lineation. In this model (Fig. 2), compression along the Monroe fault is

accommodated by shortening along the McCoy Creek backthrust as well as the Monroe anticline. The Monroe fault was likely originally an extensional Eocene structure that was rejuvenated as a reverse fault later in the Tertiary.

The CCFZ has been mapped from the Carnation quadrangle, where it intersects the SWIF, northeast into the Sultan quadrangle (Dragovich and others, 2010a,b, 2011a,b, 2012), and it likely continues north-northeast (Fig. D1 epicenter map) as a splay to the SWIF. The left-lateral strike-slip CCFZ is a conjugate fault zone to the right-lateral SWIF. Most kinematic indicators along the CCFZ, such as shallow slickenlines on steep shear planes and en echelon vein arrays, suggest left-lateral strike-slip or oblique-slip offset. An active CCFZ is indicated by (1) the 1996 Duvall earthquake and its aftershocks, and (2) faulted Vashon advance lake deposits (unit Qgl$_v$) near the main strand of the CCFZ along Youngs Creek (see significant sites 31D, 31G, 31H, and 31L and Appendix E), and perhaps (3) the transition of the Skykomish River at the town of Sultan from a multi-thread braided channel upstream to a single-thread channel downstream, coinciding with the CCFZ main strand. The faults and liquefaction features that offset and (or) intrude units Qgl$_v$ and Qtz are interpreted to result from or near the main strand of the CCFZ. The 1996 Duvall earthquake (max. M_L=5.3 or M_D=5.4, local and duration magnitudes, respectively; http://www.pnsn.org/event/10389973# overview) occurred as a mainshock and aftershock sequence that was roughly centered on the intersection of the Lake Joy, Monroe, Carnation, and Sultan quadrangles within the CCFZ, with most hypocenters originating at a shallow depth (1.2–5 mi; 2–8 km)(Dragovich and others, 2010a,b, 2011a,b, 2012). The main shock epicenter was located in the southwest corner of the Sultan quadrangle at significant site DQ (sec. 2, T26N R7E). Dragovich and others (2011b, 2012) proposed that thrust and reverse faults within the CCFZ are anastomosing structures that link the high-angle faults. The combined focal mechanism and field structural data suggest strain partitioning of displacements between both (1) left-lateral, high-angle, northeast-trending faults, and (2) lower-angle, northeast-trending reverse faults or thrust faults within the CCFZ (Dragovich and others, 2011a,b), forming a flower structure (Appendix D). This is supported by the dominance of thrust and strike-slip focal mechanisms along several faults within the CCFZ. Outcrops along the CCFZ within the field area contain abundant kinematic evidence for left-lateral strike-slip displacement. About 36 percent of the focal mechanisms in the Sultan portion of the CCFZ have a left-lateral or left-lateral-oblique northeast-trending fault solution as one component of the focal mechanism (Appendix D). Like the CCFZ, the Tokul Creek fault zone is probably a northeast-trending fault zone conjugate to the SWIF that projects to the east of the current map area and may be similarly locally active (Dragovich and others, 2009a,b, 2012; Bradford and Waters, 1934).

Finally, further work is required to study the Skykomish River character and gradient across the CCFZ. The braided habit upstream of Sultan to a few miles downstream of Index might be the result of more unvegetated point bars, visible on aerial photographs, and not neotectonic adjustments as suggested above. It is noteworthy that the geophysical information (this study; Hayashi and others, 2013) suggests that the main strand of the CCFZ has an overall eastside-up component of offset consistent with the possible change of river habit to the east.

PLEISTOCENE ALLUVIUM AND QUATERNARY STRUCTURES

Ancient alluvium representing several Pleistocene nonglacial intervals is widespread in the lower Skykomish River valley (Dragovich and others, 2011a,b). This is similar to the Snoqualmie River valley to the southwest where ancient alluvium has vertical and lateral distribution and internal structure that imply significant tectonic control of these Pleistocene nonglacial river deposits within the broad SWIF and along subsidiary structures. The Pleistocene sediments in Snoqualmie River valley have a petrographic composition similar to that of modern Snoqualmie River alluvium (Dragovich, 2007; Dragovich and others, 2007, 2009a,b,c, 2010a,b, 2011a,b, 2012). We refer to the Snoqualmie and Skykomish River sediments of that composition as SP (Table 1). SP Holocene to Pleistocene basin sediments have a distinct composition and facies architecture, forming mappable depositional facies over time. Analysis in the Monroe quadrangle west of the Sultan quadrangle shows that both ancient and modern Skykomish River alluvial deposits are compositionally and stratigraphically similar to their counterparts in the Snoqualmie River valley ($Qm_{59\text{-}65}Qp_{12\text{-}29}PF_{12\text{-}26}$) (Dragovich and others, 2011a,b). They are dominated by Tertiary granitic to granodioritic rocks, such as the Index, Grotto, and Snoqualmie batholiths that are derived from an intermediate, continental-arc source (Dragovich and others, 2011a,b). These sediments contain significant amounts of monocrystalline quartz (~10–20%), plagioclase, K-spar, and volcanic, granitic, and sedimentary lithic clasts, with lesser, but also significant, green pleochroic hornblende, pyroxene, and mica. Dragovich and others (2010a,b, 2012) mapped ancient Tolt River alluvium similar to modern Tolt River alluvium south of the map area; we correlate ancient Youngs–Elwell Creek locally derived alluvium with the Olympia beds (unit Qc$_{ol}$) in the present map area (Table 1). As observed more regionally (for example, Dragovich and others, 2012), Pleistocene SP sediments

commonly show distinct liquefaction features, including contorted bedding and sand dikes. The most prominent liquefaction in the study area was observed at significant sites 35AA (sec. 6, T27N R8E), 41P, 44E, 44D, 45A, 51L (sec. 8, T27N R8E), 62J (sec. 9, T27N R8E), 311B (sec. 2, T27N R7E), and 312K (sec. 32, T28N R8E).

Ancient SP sediment is observed at many stratigraphic levels and elevations along the Snoqualmie, Skykomish, and Tolt River valleys, where the sediments are commonly tilted or broadly folded within the SWIF and across the Carnation and Monroe fault zones. South and west of the current map area, Dragovich and others (2007, 2009a,b,c, 2010a,b, 2011a,b, 2012), and Littke and others (2009) previously applied growth folding, pull-apart, and inverted basin models to the structures and stratigraphic relations we observed. They also modeled relatively young inversion of sub-basins along the length of the SWIF in the Snoqualmie valley, whereby the Snoqualmie River has been structurally trapped within fault-controlled transpressional or transtensional basins during the Quaternary. This transition from transtensional to transpressional basins is supported by the exceptional thickness of some of the alluvial basin sediments. In this hypothesis, formerly extensional pull-apart basins are uplifted as a result of kinematic changes along the fault zones and are now tilted, folded, and (or) raised in blocks between subparallel faults.

The distribution, structural geometry, and elevation of Olympia beds around the Skykomish River suggests uplift or tilting across these structures (Cross Section A) whereby Olympia beds are likely uplifted and folded around the Monroe anticline on the upper plate of the Monroe fault. As originally proposed by Dragovich and others (2011a,b), the upper plate of the Monroe fault is characterized by uplift and folding of Olympia beds. This is supported by several newly acquired Olympia bed OSL/IRSL ages of 22.9, 23.8, 24.5, 36.8, 39.8, and 73.3 ka, as well as radiocarbon ages of 18.0, 21.9, 22.0, 23.8, 24.8, and >43.5 ka (Appendices A and B; Dragovich and others, 2011a,b) sampled across the Monroe anticline (elevations 75–300 ft above present sea level [23–91 m]). The age, stratigraphic, and structural information suggest that the Monroe fault anticline and syncline are potentially active structures having evidence for Pleistocene displacement (for example, fold tightening along the Monroe syncline). Although the combined structural, stratigraphic, and age information appears compelling, further investigation may prove that some of the elevation differences for the Olympia may be related to complex grading and inset relations of the Skykomish River during and after the Olympia nonglacial interval. The ages and structural information also support earlier contentions of Dragovich and others (2011a,b) that the elevation difference between dated ancient Skykomish River alluvial deposits (unit Qc_o) is at least partially the result of folding and uplift across the Monroe fault and anticline. Likewise, the orientation of bedding in Olympia beds, including pre-Fraser SP deposits mapped below the Olympia beds in the area north of the Skykomish River, indicates that ancient SP units are folded around the Monroe syncline (Dragovich and others, 2011a,b). SP sediments in the Monroe synclinal basin north of the Skykomish River are similarly folded and are at least 450 ft (137 m) thick. See units Qc_o, Qc_o?, and Qc_{pf} for between 30 and 215 ka and >300 ka OSL/IRSL ages from the core of the Monroe syncline. (See *Isostatic Gravity and Aeromagnetic Analyses*, Appendices A and B, and Cross Section A.) Although verging in an opposing direction, the Monroe structural setting is similar to that of basins and folds around the south-vergent Carnation fault directly to the south of the study area (Dragovich and others, 2010a,b, 2012). In that area, ancient SP is (1) folded around the Tolt River anticline, uplifting Whidbey Formation SP sediments to an elevation of about 900 ft (275 m), and (2) mapped in the synclinal basin north of this reverse fault. Thick ancient SP sediments are also mapped in the Fall City area south of the quadrangle, where SP sediments in probable SWIF pull-apart basins are as much as 800 ft (250 m) thick (Dragovich and others, 2007). Another example is directly south of the Carnation fault in the Lake Joy quadrangle, where basin sediments are as much as 400 ft (122 m) thick (Dragovich and others, 2012) directly south of the potentially active Carnation fault.

ISOSTATIC GRAVITY AND AEROMAGNETIC ANALYSES

Map-view qualitative analysis and modeling of potential field geophysical anomalies along cross section lines within the Sultan quadrangle support our interpreted stratigraphic and structural arrangement, especially at depth. High-quality aeromagnetic data define the geomagnetic anomalies (Figs. 1 and 2 on map sheet; Blakely and others, 1999), and an unpublished regional database of gravity data constrains isostatic gravity anomalies (see Anderson and others, 2006, for an overview of this database). In addition, gravity data collected in 2012 define detailed anomalies in the quadrangle. Extensive sampling and measurement of physical properties for units in this and neighboring quadrangles (Dragovich and others, 2010a,b, 2011a,b, 2012) provide strong support for predicting anomalies produced by cross section interpretations, as well as a means for interpreting map-view anomalies in terms of subsurface geologic units. As in previously studied neighboring quadrangles, undivided Western mélange belt rocks

(unit KJm$_W$) have low magnetic susceptibility and are moderately dense, accounting for map regions with high gravity anomalies and relatively low magnetic anomalies (for example, gravity high WMBH in Fig. 1 on map sheet). Although we separate metasediments (unit KJms$_W$) and metachert (unit KJmc$_W$) in the field, they are not separated in our geophysical modeling because they have similar densities. However, it is probable that the Sultan quadrangle contains more tectonic fragments of metagabbro (unit KJigb$_W$) than previously investigated regions. Not only is this supported by mapping of Tabor and others (1993) that shows metagabbro is common at the surface in the area, but laterally extensive, low-amplitude, long-wavelength magnetic highs (for example, WMB in Fig. 1 on map sheet) extend throughout the quadrangle, suggesting unit KJigb$_W$ bodies are common at depth. Also reflecting previous work, the Mount Persis unit is less dense overall than unit KJm$_W$ and is locally quite magnetic, with variable density (Dragovich and others, 2012). The basalts (unit Evb$_P$) and basaltic andesites (unit Eva$_{PD}$) are especially magnetic and dense, while tuffs (unit Evt$_P$) and volcaniclastic (unit Evc$_P$) units have low magnetic susceptibility and low density (Dragovich and others, 2012). Therefore, Mount Persis unit map areas have overall low gravity (PL in Fig. 1 on map sheet), but exhibit short-wavelength, higher-amplitude magnetic anomalies with highs reflecting a greater percentage of basalts and (or) andesites (PB in Fig. 1 on map sheet) and lows reflecting a greater percentage of tuffaceous and (or) clastic rocks (PT in Fig. 1 on map sheet). Geophysical model A (Fig. 2 on map sheet) is consistent with the hypothesis that Mount Persis units interfinger on the structural cross sections; however, these units could have numerous configurations that would also predict the geophysical anomalies observed, and therefore the configuration we show is not the only possibility. On the other hand, Mount Persis unit basalts, andesites, tuffs, and volcaniclastic rocks have distinguishable physical property characteristics; therefore, their general distribution within Cross Section A is well supported by the geophysical modeling. Similar logic applies to the distribution of metagabbro within the Western mélange belt basement rocks. The contrasting magnetic character of units KJm$_W$ and Evs$_P$ support our model of the Monroe fault, because it clearly divides the map into two regions containing quite different geophysical signatures with anomalies reflecting the low density and variable magnetization expected of the Mount Persis unit in the southeast, and the high density and more deeply sourced magnetization coming from the Western mélange belt to the northwest (See Fig. 1 and model A in Fig. 2 on map sheet). Thus we do not interpret Mount Persis unit to exist north of the Monroe fault, and instead interpret unit KJm$_W$ close to the surface.

Mapping within and directly to the east of the quadrangle suggests that the Young's Creek complex (unit Eigd$_Y$) intrudes to a shallow level in the eastern part of the map area (Cross Section B in Fig. 2 on map sheet) and is consistent with a gabbroic intrusive complex present directly to the south of the map area (unit Ei$_P$ of Dragovich and others, 2012). The granodiorite is slightly less dense than rocks of the Western mélange belt, and therefore has little effect on the gravity anomalies within the quadrangle. However, gabbroic phases are expected at depth based on observed mafic enclaves within the granodiorite and a probable mafic border phase directly to the east. Presence of a large, dense pluton in this region is also supported by recent regional gravity and magnetic modeling of the Puget Lowland crustal structure (Anderson and others, 2011). Therefore, we expect that gabbro at depth just east of the quadrangle affects gravity gradients within the Sultan quadrangle and is responsible for high gravity anomalies observed along the eastern edge of the map (YCGB in Fig. 1 on map sheet). Because units Eigd$_Y$ and KJm$_W$ have relatively similar densities, the intrusive contact geometry on Cross Section B (Fig. 2 on map sheet) is speculative.

In addition to the Monroe fault, two other younger tectonic features are evident in the geophysical map: (1) the Monroe syncline, and (2) the CCFZ. A gravity low clearly marks the east-trending axis of the Monroe syncline (MS in Fig. 1 on map sheet); this northward shift in the axis of this gravity low to the east is probably the result of left-stepping geometry crossing the CCFZ. This northward shift in gravity lows is more apparent on regional gravity maps. In the western part of the quadrangle, the southern boundary of the syncline coincides with the Monroe fault (Cross Section A in Fig. 2 on map sheet), however, to the east, it is not clear if a fault exists along its southern margin, though it could be permissible given an east-trending gravity gradient in this region (MSEG in Fig. 1 on map sheet). Unit Ts is undivided Tertiary sedimentary rocks (shown only at depth on the cross sections), as indicated by the relative amplitude of the gravity low associated with the Monroe syncline (especially along Cross Section B). These rocks may correlate with the distal volcaniclastic rocks of Mount Persis, Blakeley Formation, rocks of Bulson Creek, or Miocene sedimentary rocks, and our interpretation is similar to previous work in the Monroe area where units Evc$_P$, ΦEc, ΦEn, and Mvc occur at depth along the axis of the Monroe syncline (Dragovich and others, 2011a,b). Note that the magnitude of the gravity low due to the syncline along Cross Section A is very poorly constrained—the map shows a gravity low in this region, but the magnitude of the low is not well supported by the gravity data, thus the thickness of the units within the syncline can only be generally constrained without more data. There are, however, gravity data north of this line, so the strong upward swing of the gravity values predicted by the model at its north end is realistic.

The CCFZ is evident in the geophysical data; there are relatively lower magnetic anomalies along the entire fault zone, and a strong gradient (CCMS in Fig. 1 on map sheet) along a section of the main strand showing significant vertical offset (Cross Section B in Fig. 2 on map sheet). A companion study using passive seismic imaging of the subsurface across the CCFZ directly north of Cross Section B supports shallowing bedrock across the main strand (Hayashi and others, 2013). In addition, moderate gravity values in the middle of Cross Section B indicate widely distributed, lower density unit KJm_W within the CCFZ. Hence, we model a wide zone of moderately less dense unit tz (Cross Section B in Fig. 2 on map sheet) with more limited zones of lower density unit tz immediately adjacent to each strand. Although the exact physical properties of these tectonized units are uncertain, modeled values agree with the general alteration and tectonism observed along the CCFZ. The distribution of metavolcanic subunit $KJmv_W$ is highly speculative at depth, but helps us fit very subtle magnetic highs across the middle and eastern parts modeled along Cross Section B; however, either unit $KJmv_W$ and (or) deep unit $KJigb_W$ could adequately model these magnetic anomalies.

GEOCHEMISTRY OF BEDROCK AND QUATERNARY SAND DEPOSITS

A large geochemical dataset now exists for Quaternary ancient and modern alluvium and glacial deposits (n = 98 samples)(Dragovich and others, 2010a,b, 2011a,b, 2012, this study). See Appendix C for analytical methods and geochemical data (Table C1) and additional plots (Figs. C1-C4). Dragovich and others (2010a,b, 2011a,b) were able to discriminate modern and ancient alluvium that have a locally derived provenance from samples that have a Skykomish and Snoqualmie River basin provenance (SP), based on their chondrite-normalized La/Lu ratios (Fig. 3)(Table 1). This ratio difference is interpreted to result from local alluvium having a larger volcanic component, while the SP alluvium has a larger plutonic component. In addition, Dragovich and others (2010a,b, 2011a,b) were able to discriminate between glacial and nonglacial sediments using Pb/Yb ratios (Fig. 3). Sand sample petrography indicates this is the result of lesser igneous and higher sedimentary lithic detritus in the glacially derived samples. A few samples from this study and the Lake Joy quadrangle (Dragovich and others, 2012) plot transitionally between local and SP sources (for example, the unit Qc_O sample taken at significant sites 45A and 45B) on La/Lu and Pb/Yb discriminations (Fig. 3), probably a result of geochemical homogenization due to river systems eroding into local deposits (for example, deposits near a cutbank on an ancient river where the input of local detritus is increased). Both glacial and nonglacial sediments plot between intermediate and felsic sources on discrimination diagrams (Fig. C1; Dragovich and others, 2010a,b, 2011a,b, 2012) and some have a large local volcanic detrital component (for example, unit Qga_V geochemical sample 13AA , sec. 4, T26N R8, and Figs. 3 and C1).

A large geochemical dataset now exists for the volcanic rocks of Mount Persis (Mount Persis unit; n=64 samples)(Dragovich and others, 2009a,b, 2010a,b, 2011a,b, 2012, this study). The Mount Persis unit was originally described by Tabor and others (1993) as being mostly andesitic in composition. However, our studies have revealed composition ranges from medium-K calc-alkaline basalt to rhyolite, with most samples being andesite or dacite (Fig. 4; Table C1); however, samples with lower SiO_2 values are transitional to tholeiitic (Fig. C2). About two-thirds of the Mount Persis unit samples are metaluminous, while about one third are peraluminous (Fig. C3). Predominantly, peraluminous samples have $SiO_2 > 68\%$ (Fig. C3). With four exceptions, the Mount Persis samples with $SiO_2 < 68\%$ are magnesian, and the samples with $SiO_2 > 68\%$ are ferroan (Fig. C4). Mount Persis samples have elevated Th/Yb ratios and Ta/Yb ratios (Fig. 5). A granodiorite from the Youngs Creek intrusive complex (unit $Eigd_Y$ 1.62 mi [2.6 km] directly east of age site 11G and the Sultan quadrangle's eastern boundary) is medium-K calc-alkaline (Fig. C2), metaluminous (Fig. C3), and magnesian (Fig. C4). This sample has identical Th/Yb and Ta/Yb ratios to the Mount Persis unit (Fig. 5). Mount Persis unit volcanics are calc-alkaline to tholeiitic, metaluminous to peraluminous, and magnesian—similar to modern continental arcs (Pearce, 1996a; Frost and others, 2001). This setting is supported by the Mount Persis unit plotting in the active continental arc field on the Th/Yb vs. Ta/Yb diagram of Pearce (1982, 1983; Fig. 5). The peraluminous and ferroan chemistries of samples that have $SiO_2 > 68\%$ (Figs. C3 and C4) are interpreted as the result of increased assimilation of continental crust as this magmatic system evolved to more felsic compositions. Unit $Eigd_Y$ granodiorite has the same major element geochemical affinities as the Mount Persis unit (Figs. 4, C2, C3, and C4) and has a Ta/Yb ratio that overlaps the Mount Persis ratios (Fig. 5). We suggest the Youngs Creek intrusive complex sample fractionated from the same enriched mantle source as the Mount Persis unit. The fluid mobile element, Th, is elevated in Mount Persis samples as a result of dehydration of a subducting plate initiating partial melting in the mantle during convergent tectonic activity (Pearce, 1982, 1983, 1996b). Twelve Mount Persis samples have SiO_2, Sr, and Y values indicating adakites (Table C1) (Defant and

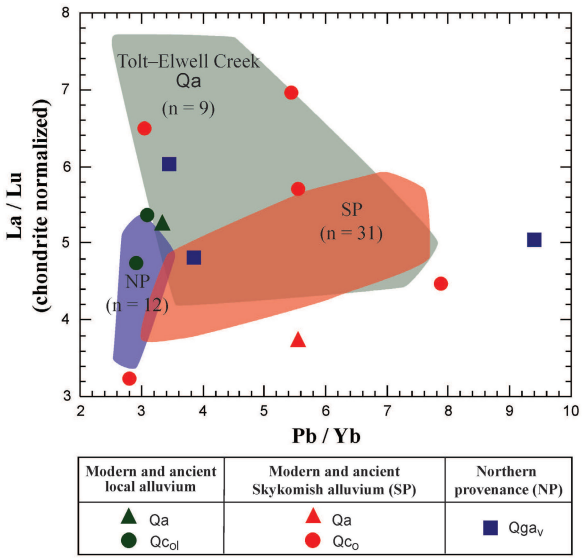

Figure 3. Chondrite-normalized La/Lu vs. Pb/Yb diagram for Quaternary samples. Chondrite normalization values are from McDonough and Sun (1995). SP = modern and ancient Skykomish and Snoqualmie River basin provenance; Tolt–Elwell Creek = Qa. Colored fields for NP, SP, and Qa are derived from previous studies (n=number of previous study samples; Dragovich and others, 2010a,b, 2011a,b). Compare with provenance information on Table 1.

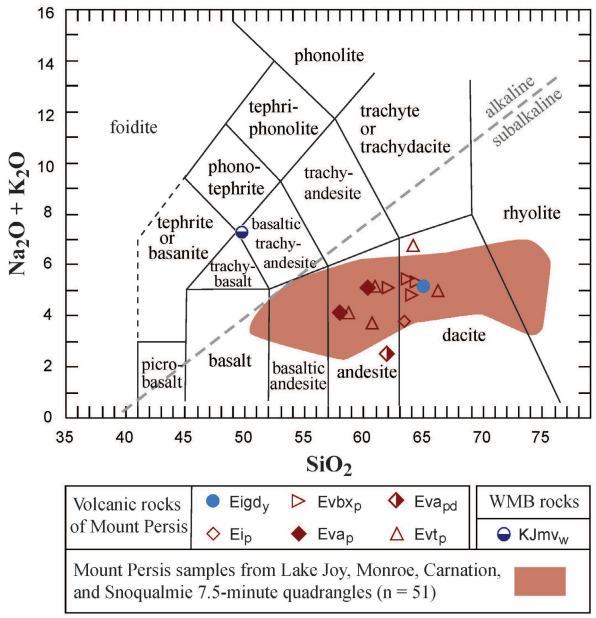

Figure 4. Total alkali silica diagram of Le Maitre and others (2002) adapted for the Western mélange belt and the volcanic rocks of Mount Persis, including Youngs Creek intrusive complex. Data that define the brown colored Mount Persis unit field are taken from 51 samples from earlier studies of Dragovich and others (2009a,b, 2010a,b, 2011a,b, 2012).

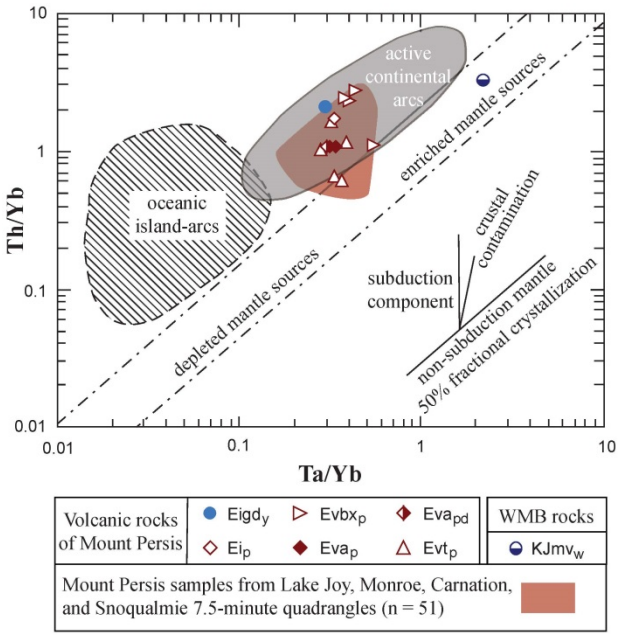

Figure 5. Th/Yb vs. Ta/Yb diagram of Pearce (1982, 1983) adapted for Western mélange belt and the volcanic rocks of Mount Persis including the Youngs Creek intrusive complex. Data that define the brown colored Mount Persis unit field are taken from 51 samples from earlier studies of Dragovich and others (2009a,b, 2010a,b, 2011a,b, 2012).

Drummond, 1990). This adakitic affinity could be the result of melting of a subducted oceanic ridge (Defant and Drummond, 1990). Sample 50S is chloritized metabasalt from the Western mélange belt (unit KJmv$_W$; sec. 10, T27N R8E on map sheet and Table C1) that plots as an alkaline basaltic trachyandesite on Figure 4. Based on the subdivision for basaltic trachyandesite of Le Maitre and others (2002) this sample can be chemically classified as a mugearite. This sample is an alkaline basaltic trachyandesite (Fig. 4) and plots in the mantle array field on the Th/Yb

vs. Ta/Yb diagram of Pearce (1982, 1983), indicating an extremely enriched mantle source and an intraplate tectonic origin (Fig. 5). The elevated Yb with respect to the other trace elements may have resulted from a hotspot plume melting a deep garnet peridotite source (Pearce, 1996b, 2008). We interpret this sample to have originated in an oceanic island setting that was created by hotspot magmatism, similar to other mélanges in Washington State, such as the Eastern mélange belt and the De Roux unit, that have plate oceanic island basalt magmatic affinities with lithologic relationships that exclude a flood basalt interpretation (Tabor, 1994; MacDonald and others, 2009).

ACKNOWLEDGMENTS

This geologic map was funded in part by the U.S. Geological Survey (USGS) National Cooperative Geologic Mapping Program under award no. G12AC20234. We thank: Jason Hiskey (student, Western Wash. Univ.) for help in the field; Randall Conger-Best (student, Wash. State Univ.) for help in the office; Jonathan M. Lees (Univ. of North Carolina) for help with the earthquake data; Harrison Gray (USGS, Denver) for help with OSL analyses, and Koichi Hayashi (Geometrics, Inc.) for organizing, implementing, and running the passive seismic companion study cited in the text; Julie Stangell (Hancock Forest Management), Mark Baugh (Campbell Group, LLC) and Mr. Bowman (property owner) for logistical help; Ray Wells (USGS) for laboratory support; Laureen Wagoner, Rick Conrey, and Charles Knaack (WSU) for geochemical analyses of samples. We thank Eric Dingeldein (Wash. State Dept. of Transportation), Cyd Donk (City of Sultan permit assistant), Carolyn Eslick (City of Sultan Mayor), Jeff Jones (Snohomish County), and Sue Kahle and Theresa Olsen (USGS, Water Resources Division) for subsurface geologic information. We also thank our Washington Division of Geology and Earth Resources colleagues: Tim Walsh for a review, Jessica Czajkowski for GIS help and a review; Tara Salzer for logistical support, and Lee Walking for assistance with references.

REFERENCES CITED

Anderson, M. L.; Blakely, R. J.; Brocher, T. M.; Pratt, T. L.; Wells, R. E.; Haugerud, R.; Bush, M., 2006, Structure of the Seattle uplift from seismic, gravity, magnetic, geologic, and geomorphic data [abstract]: Eos (American Geophysics Union Transactions), v. 87, no. 52, Supplement, T41A-1554.

Anderson, M. L.; Blakely, R. J.; Wells, R. E.; Dragovich, J., 2011, Eastern boundary of the Siletz terrane in the Puget Lowland from gravity and magnetic modeling with implications for seismic hazard analysis [abstract]: Eos (American Geophysical Union Transactions), Fall Meeting, Abstract GP33B-06. [http://adsabs.harvard.edu/abs/2011AGUFMGP33B..06A]

Armstrong, J. E.; Crandell, D. R.; Easterbrook, D. J.; Noble, J. B., 1965, Late Pleistocene stratigraphy and chronology in southwestern British Columbia and northwestern Washington: Geological Society of America Bulletin, v. 76, no. 3, p. 321-330.

Associated Earth Sciences, Inc., 2001, Proposed borrow pit dewatering impact analysis—Trilogy at Redmond Ridge, King County, Washington: Associated Earth Sciences, Inc., 1 v.

Associated Earth Sciences, Inc., 2002, Final hydrogeologic and geotechnical assessment report—Pegasus Thoroughbred Training Center, King County, Washington: Associated Earth Sciences, Inc., 1 v.

Associated Earth Sciences, Inc., 2003, Proposed Snoqualmie Ridge II project—Environmental impact statement—Technical report on geology, soils, and groundwater: Associated Earth Sciences, Inc., [Kirkland, Wash., under contract to] Quadrant Corporation, 1 v.

Associated Earth Sciences, Inc., 2004, Environmental impact statement—Technical report on geology, soils and ground water, Redmond Ridge East UPD/FCC and Panhandle preliminary plat, King County, Washington: Associated Earth Sciences, Inc., 1 v.

Associated Earth Sciences, Inc., 2007, Summary of SRS-1 No. 1 infiltration pond, general geologic hazard, and geotechnical engineering recommendations, recreation complex, Redmond Ridge East, King County, Washington: Associated Earth Sciences, Inc., 1 v.

Bhatia, M. R.; Crook, K. A. W., 1986, Trace element characteristics of graywackes and tectonic setting discrimination of sedimentary basins: Contributions to Mineralogy and Petrology, v. 92, no. 2, p. 181-193.

Blakely, R. J.; Wells, R. E.; Weaver, C. S., 1999, Puget Sound aeromagnetic maps and data: U.S. Geological Survey Open-File Report 99-514, version 1.0. [http://pubs.usgs.gov/of/1999/of99-514/]

Booth, D. B., 1984, Glacier dynamics and the development of glacial landforms in the eastern Puget Lowland, Washington: University of Washington Doctor of Philosophy thesis, 217 p., 1 plate. [http://hdl.handle.net/1773/6696]

Booth, D. B., 1986, The formation of ice-marginal embankments into ice-dammed lakes in the eastern Puget Lowland, Washington, U.S.A., during the late Pleistocene: Boreas, v. 15, no. 3, p. 247-263.

Booth, D. B., 1990, Surficial geologic map of the Skykomish and Snoqualmie Rivers area, Snohomish and King Counties, Washington: U.S. Geological Survey Miscellaneous Investigations Series Map I-1745, 2 sheets, scale 1:50,000, with 22 p. text. [http://pubs.er.usgs.gov/publication/i1745]

Bradford, D. C.; Waters, A. C., 1934, The Tolt River earthquake and its bearing on the structure of the Cascade Range: Seismological Society of America Bulletin, v. 24, no. 1, p. 51-62.

Broecker, W. S.; Kulp, J. L.; Tucek, C. S., 1956, Lamont natural radiocarbon measurements, III: Science, v. 124, no. 3213, p. 154-165.

Colman, S. M.; Pierce, K. L., 1981, Weathering rinds on andesitic and basaltic stones as a Quaternary age indicator, western United States: U.S. Geological Survey Professional Paper 1210, 56 p. [http://pubs.er.usgs.gov/publication/pp1210]

Danner, W. R., 1957, A stratigraphic reconnaissance in the northwestern Cascade mountains and San Juan Islands of Washington State: University of Washington Doctor of Philosophy thesis, 3 v. [562 p.], 7 plates.

Defant, M. J.; Drummond, M. S., 1990, Derivation of some modern arc magmas by melting of the subducted lithosphere in a volcanic arc: Nature, v. 347, no. 6294, p. 662-665.

Dickinson, W. R., 1970, Interpreting detrital modes of graywacke and arkose: Journal of Sedimentary Petrology, v. 40, no. 2, p. 695-707.

Dragovich, J. D., 2007, Sand point count and geochemical data in the Fall City and Carnation 7.5-minute quadrangles, King County, Washington: Washington Division of Geology and Earth Resources Open File Report 2007-3, 2 Microsoft Excel files and 6 p. text. [http://www.dnr.wa.gov/publications/ger_ofr2007-3_fallcity_supplement.zip]

Dragovich, J. D.; Anderson, M. L.; MacDonald, J. H., Jr.; Mahan, S. A; DuFrane, S. A.; Littke, H. A.; Wessel, G. R.; Saltonstall, J. H.; Koger, C. J.; Cakir, Recep, 2010a, Supplement to the geologic map of the Carnation 7.5-minute quadrangle, King County, Washington—Geochronologic, geochemical, point count, geophysical, earthquake, fault, and neotectonic data: Washington Division of Geology and Earth Resources Open File Report 2010-2, 42 p., 8 digital appendices. [http://www.dnr.wa.gov/publications/ger_ofr2010-2_carnation_supplement.zip]

Dragovich, J. D.; Anderson, M. L.; Mahan, S. A.; Koger, C. J.; Saltonstall, J. H.; MacDonald, J. H., Jr.; Wessel, G. R.; Stoker, B. A.; Bethel, J. P.; Labadie, J. E.; Cakir, Recep; Bowman, J. D.; DuFrane, S. A., 2011a, Geologic map of the Monroe 7.5-minute quadrangle, King and Snohomish Counties, Washington: Washington Division of Geology and Earth Resources Open File Report 2011-1, 1 sheet, scale 1:24,000, with 24 p. text. [http://www.dnr.wa.gov/publications/ger_ofr2011-1_geol_map_monroe_24k.zip]

Dragovich, J. D.; Anderson, M. L.; Mahan, S. A.; MacDonald, J. H., Jr.; McCabe, C. P; Cakir, Recep; Stoker, B. A.; Villeneuve, N. M.; Smith, D. T.; Bethel, J. P., 2012, Geologic map of the Lake Joy 7.5- minute quadrangle, King County, Washington: Washington Division of Geology and Earth Resources Map Series 2012-01, 2 sheets, scale 1:24,000, with 79 p. text and 1 Excel file. [http://www.dnr.wa.gov/publications/ger_ms2012-01_geol_map_lake_joy_24k.zip]

Dragovich, J. D.; Anderson, M. L.; Walsh, T. J.; Johnson, B. L.; Adams, T. L., 2007, Geologic map of the Fall City 7.5-minute quadrangle, King County, Washington: Washington Division of Geology and Earth Resources Geologic Map GM-67, 1 sheet, scale 1:24,000. [http://www.dnr.wa.gov/publications/ger_gm67_geol_map_fallcity_24k.zip]

Dragovich, J. D.; Littke, H. A.; Anderson, M. L.; Hartog, Renate; Wessel, G. R.; DuFrane, S. A.; Walsh, T. J.; MacDonald, J. H., Jr.; Mangano, J. F.; Cakir, Recep, 2009a, Geologic map of the Snoqualmie 7.5-minute quadrangle, King County, Washington: Washington Division of Geology and Earth Resources Geologic Map GM-75, 2 sheets, scale 1:24,000. [http://www.dnr.wa.gov/publications/ger_gm75_snoqualmie_24k.zip]

Dragovich, J. D.; Littke, H. A.; Anderson, M. L.; Wessel, G. R.; Koger, C. J.; Saltonstall, J. H.; MacDonald, J. H., Jr.; Mahan, S. A.; DuFrane, S. A., 2010b, Geologic map of the Carnation 7.5-minute quadrangle, King County, Washington: Washington Division of Geology and Earth Resources Open File Report 2010-1, 1 sheet, scale 1:24,000, with 21 p. text. [http://www.dnr.wa.gov/Publications/ger_ofr2010-1_geol_map_carnation_24k.zip]

Dragovich, J. D.; Littke, H. A.; MacDonald, J. H., Jr.; DuFrane, S. A.; Anderson, M. L.; Wessel, G. R.; Hartog, Renate, 2009b, Geochemistry, geochronology, and sand point count data for the Snoqualmie 7.5-minute quadrangle, King County, Washington: Washington Division of Geology and Earth Resources Open File Report 2009-4, 35 p. text, with 3 Microsoft Excel files. [http://www.dnr.wa.gov/Publications/ger_ofr2009-4_snoqualmie_suppl.zip]

Dragovich, J. D.; Mahan, S. A.; Anderson, M. L.; MacDonald, J. H., Jr.; Wessel, G. R.; DuFrane, S. A.; Cakir, Recep; Bowman, J. D.; Littke, H. A., 2011b, Analytical data from the Monroe 7.5-minute quadrangle, King and Snohomish Counties, Washington—Supplement to Open File Report 2011-1: Washington Division of Geology and Earth Resources Open File Report 2011-2, 58 p., 2 plates, 2 Microsoft Excel files. [http://www.dnr.wa.gov/publications/ger_ofr2011-2_monroe_supplement.zip]

Dragovich, J. D.; Walsh, T. J.; Anderson, M. L.; Hartog, Renate; DuFrane, S. A.; Vervoot, Jeff; Williams, S. A.; Cakir, Recep; Stanton, K. D.; Wolff, F. E.; Norman, D. K.; Czajkowski, J. L., 2009c, Geologic map of the North Bend 7.5-minute quadrangle, King County, Washington, with a discussion of major faults, folds, and basins in the map area: Washington Division of Geology and Earth Resources Geologic Map GM-73, 1 sheet, scale 1:24,000. [http://www.dnr.wa.gov/publications/ger_gm73_geol_map_northbend_24k.zip]

Frost, B. R.; Barnes, C. G.; Collins, W. J.; Arculus, R. J.; Ellis, D. J.; Frost, C. D., 2001, A geochemical classification for granitic rocks: Journal of Petrology, v. 42, no. 11, p. 2033-2048.

Fuller, R. E., 1925, The geology of the northeastern part of Cedar Lake quadrangle with special reference to the de-roofed Snoqualmie batholith: University of Washington Master of Science thesis, 96 p., 4 plates.

Hayashi, Koichi; Cakir, Recep; Dragovich, J. D; Stoker, B. A; Walsh, T. J.; Littke, H. A., 2013, Passive seismic analyses in the Sultan 7.5-minute quadrangle, King and Snohomish Counties, Washington: Washington Division of Geology and Earth Resources Open File Report 2013-04, 9 p. [http://www.dnr.wa.gov/publications/ger_ofr2013-04_seismic_analysis_sultan_quad.pdf]

Jett, G. A., 1986, Sedimentary petrology of the western mélange belt, north Cascade Range, Washington: University of Wyoming Master of Science thesis, 85 p.

Jett, G. A.; Heller, P. L., 1988, Tectonic significance of polymodal compositions in mélange sandstones, western mélange belt, north Cascade Range, Washington: Journal of Sedimentary Petrology, v. 58, no. 1, p. 52-61.

Johnson, D. M.; Hooper, P. R.; Conrey, R. M., 1999, XRF analysis of rocks and minerals for major and trace elements on a single low dilution Li-tetraborate fused bead: Advances in X-ray Analysis, v. 41, p. 843-867. [http://www.sees.wsu.edu/Geolab/note/V41_91.pdf]

Knaack, C.; Cornelius, S.; Hooper, P., 1994, Trace element analysis of rocks and minerals by ICP/MS: Department of Geology Washington State University Open-file Report, December 1994, 18 p.

Knoll, K. M., 1967, Surficial geology of the Tolt River area, Washington: University of Washington Master of Science thesis, 91 p., 1 plate.

Le Maitre, R. W.; Streckeisen, A.; Zanettin, B.; Le Bas, M. J.; Bonin, B.; Bateman, P., eds., 2002, Igneous rocks—A classification and glossary of terms; 2nd ed.: Cambridge University Press, Cambridge, U.K., 256 p.

Lees, J. M., 1999, Geotouch—Software for three and four-dimensional GIS in the earth sciences**:** Computers & Geosciences, v. 26, no. 7, p. 751-761.

Lees, J. M., 2007, RFOC—Graphics for spherical distributions and earthquake focal mechanisms, graphics for statistics on a sphere, as applied to geological fault data, crystallography, earthquake focal mechanisms, radiation patterns, ternary plots and geographical/geological maps: Comprehensive R Archive Network (CRAN). [accessed May 31, 2011, at http://streaming.stat.iastate.edu/CRAN/web/packages/RFOC/index.html].

Lees, J. M., 2008, GEOmap—Topographic and geologic mapping: Comprehensive R Archive Network (CRAN) [accessed May 31, 2011, at http://streaming.stat.iastate.edu/CRAN/web/packages/GEOmap/index.html].

Littke, H. A.; Dragovich, J. D.; Anderson, Megan; Hartog, Renate; Wessel, G. R.; DuFrane, S. A.; Walsh, T. J.; MacDonald, J. H., Jr.; Cakir, Recep, 2009, Geologic map of the Snoqualmie 7.5-minute quadrangle, King County, Washington—Active faulting, basin inversion and Miocene volcanic extrusion of the Snoqualmie batholith along the Rattlesnake Mountain fault zone [abstract]: Geological Society of America Abstracts with Programs, v. 41, no. 7, p. 457.

MacDonald, J. H., Jr.; Miller, R. B.; Dragovich, J. D.; Metzger, E. P.; Miller, J. S.; Harper, G. D., 2009, Geology and geochemistry of the De Roux unit and possibly correlative tectonostratigraphic terranes within the Cascade mountains, Washington: Geological Society of America Abstracts with Programs, v. 41, no. 7, p. 518.

Mackin, J. H., 1941, Glacial geology of the Snoqualmie–Cedar area, Washington: Journal of Geology, v. 49, no. 5, p. 449-481.

McDonough, W. F.; Sun, S. S., 1995, The composition of the Earth: Chemical Geology, v. 120, p. 223-253.

Morrison, R. B., ed., 1991, Quaternary nonglacial geology—Conterminous U.S.: Geological Society of America DNAG Geology of North America, v. K-2, 672 p., 8 plates.

Pearce, J. A., 1982, Trace element characteristics of lavas from destructive plate boundaries. *In* Thorpe, R. S., ed., Andesites—Orogenic andesites and related rocks: John Wiley & Sons [Chichester, U.K.], p. 525-548.

Pearce, J. A., 1983, Role of the subcontinental lithosphere in magma genesis at active continental margins. *In* Hawksworth, C. J.; Norry, M. J., eds., Continental basalts and mantle xenoliths: Shiva Publishing, [Nantwich, Great Britain], p. 230-249.

Pearce, J. A., 1996a, Sources and setting of granitic rocks: Episodes, v. 19, no. 4, p. 120-125.

Pearce, J. A., 1996b, A user's guide to basalt discrimination diagrams. *In* Wyman, D. A., ed., Trace element geochemistry of volcanic rocks—Applications for massive sulphide exploration: Geological Association of Canada Short Course Notes, v. 12, p. 79-113.

Pearce, J. A., 2008, Geochemical fingerprinting of oceanic basalts with applications to ophiolite classification and the search for Archean oceanic crust: Lithos, v. 100, no. 1-4, p. 14-48.

Pessl, Fred, Jr.; Dethier, D. P.; Booth, D. B.; Minard, J. P., 1989, Surficial geologic map of the Port Townsend 30- by 60-minute quadrangle, Puget Sound region, Washington: U.S. Geological Survey Miscellaneous Investigations Series Map I-1198-F, 1 sheet, scale 1:100,000, 13 p. text. [http://ngmdb.usgs.gov/Prodesc/proddesc_9029.htm]

Pettijohn, F. J., 1957, Sedimentary rocks; 2nd ed.: Harper & Row, 718 p.

Porter, S. C.; Swanson, T. W., 1998, Radiocarbon age constraints on rates of advance and retreat of the Puget lobe of the Cordilleran ice sheet during the last glaciation: Quaternary Research, v. 50, no. 3, p. 205-213.

Prescott, J. R.; Hutton, J. T., 1994, Cosmic ray contributions to dose rates for luminescence and ESR dating—Large depths and long-term time variations: Radiation Measurements, v. 23, p. 497-500.

Sherrod, B. L.; Blakely, R. J.; Weaver, C. S.; Kelsey, H. M.; Barnett, Elizabeth; Liberty, Lee; Meagher, K. L.; Pape, Kristin, 2008, Finding concealed active faults—Extending the southern Whidbey Island fault across the Puget Lowland, Washington: Journal of Geophysical Research, v. 113, B05313, doi:10.1029/2007JB005060, 2008.

Tabor, R. W., 1994, Late Mesozoic and possible early Tertiary accretion in western Washington State: the Helena-Haystack mélange and the Darrington–Devils Mountain fault zone: Geological Society of America Bulletin, v. 106, no. 2, p. 217-232.

Tabor, R. W.; Frizzell, V. A., Jr.; Booth, D. B.; Waitt, R. B., 2000, Geologic map of the Snoqualmie Pass 30 x 60 minute quadrangle, Washington: U.S. Geological Survey Geologic Investigations Series Map I-2538, 1 sheet, scale 1:100,000, 57 p. text. [http://geopubs.wr.usgs.gov/i-map/i2538/]

Tabor, R. W.; Frizzell, V. A., Jr.; Booth, D. B.; Waitt, R. B.; Whetten, J. T.; Zartman, R. E., 1993, Geologic map of the Skykomish River 30- by 60-minute quadrangle, Washington: U.S. Geological Survey Miscellaneous Investigations Series Map I-1963, 1 sheet, scale 1:100,000, 42 p. text. [http://pubs.usgs.gov/imap/i1963/]

Troost, K. G.; Booth, D. B.; Wisher, A. P.; Shimel, S. A., 2005, The geologic map of Seattle—A progress report: U.S. Geological Survey Open-File Report 2005-1252, version 1.0, 1 sheet, scale 1:24,000. [http://pubs.usgs.gov/of/2005/1252/]

U.S. Geological Survey Geologic Names Committee, 2010, Divisions of geologic time—Major chronostratigraphic and geochronologic units: U.S. Geological Survey Fact Sheet 2010-3059, 2 p. [http://pubs.usgs.gov/fs/2010/3059/]

Varnes, D. J., 1978a, repr. 1995, Landslide classification system. *In* Dragovich, J. D.; Brunengo, M. J., Landslide map and inventory, Tilton River–Mineral Creek area, Lewis County, Washington: Washington Division of Geology and Earth Resources Open File Report 95-1, 165 p., Plate 3. [http://www.dnr.wa.gov/publications/ger_ofr95-1_lewis_co_landslides_plates.pdf; http://www.dnr.wa.gov/publications/ger_ofr95-1_lewis_co_landslides_text.pdf]

Varnes, D. J., 1978b, Slope movement types and processes. *In* Schuster, R. L.; Krizek, R. J., eds., Landslides—Analysis and control: National Academy of Sciences Transportation Research Board Special Report 176, p. 11-33, 1 plate.

Walsh, T. J., 1984, Geology and coal resources of central King County, Washington: Washington Division of Geology and Earth Resources Open File Report 84-3, 24 p., 2 plates. [http://www.dnr.wa.gov/publications/ger_ofr84-3_central_king_co_coal_24k.pdf]

Wolfe, J. A.; Forest, C. E.; Molnar, Peter, 1998, Paleobotanical evidence of Eocene and Oligocene paleoaltitudes in midlatitude western North America: Geological Society of America Bulletin, v. 110, no. 5, p. 664-678.

Yount, J. C.; Marcus, K. L.; Mozley, P. S., 1980, Radiocarbon-dated localities from the Puget Lowland, Washington: U.S. Geological Survey Open-File Report 80-780, 51 p., 1 plate. [http://pubs.er.usgs.gov/publication/ofr80780]

Appendix A. Radiocarbon Ages

Table A1. Radiocarbon ages in the Sultan 7.5-minute quadrangle. Lab uncertainty values are one standard deviation (68% confidence interval) and include random errors that can be estimated by the lab, but exclude uncertainties that cannot be detected by the laboratory's analytical procedures. Analyses were performed by Beta Analytic, Inc. (Miami, Florida). Conventional radiocarbon ages are adjusted for measured $^{13}C/^{12}C$ ratio. 'yr BP' signifies radiocarbon years before A.D.1950. We report only the radiocarbon ages in or very near the Sultan 7.5-minute quadrangle, although some discussion may include data from other mapped quadrangles. See Dragovich and others (2010b, 2011b, 2012) for a compilation of radiocarbon sites in the adjacent Carnation, Monroe, and Lake Joy 7.5-minute quadrangles, respectively. Data are organized chronologically from youngest to 'infinite' radiocarbon ages. Sample locations shown on map sheet. All elevations are measured above mean sea level and obtained from the topographic map of the Sultan 7.5-minute quadrangle. **Geologic units:** unit Qa, Youngs Creek alluvium; unit Qc_{ol}, Olympia beds, local facies; unit Qc_{o}, Olympia beds, Skykomish River facies; unit Qc_{pf}, pre-Fraser nonglacial deposits, Skykomish River facies. SP, ancient nonglacial Skykomish River basin provenance (Table 1). AMS, radiocarbon analysis by atomic mass spectrometry for small samples; IRSL, infrared stimulated luminescence sediment dating technique; OSL, optically stimulated luminescence sediment dating technique; Mount Persis unit, volcanic rocks of Mount Persis.

Age Site	Analyzed organic material (geologic unit)	$^{13}C/^{12}C$ (o/oo)	Conventional radiocarbon age(yr BP)	Notes
40D	wood (unit Qa of Youngs Creek)	-27.8	9,440 ±40	Standard radiometric analysis with extended counting of multiple wood fragments from a Holocene peat deposit along Youngs Creek in the central region of the Sultan quadrangle. Site 40D was stratigraphically below a 10-ft (3 m)-thick stratified Youngs Creek alluvial sequence and excavated from a thin, moderately consolidated peat bog deposit composed of detritus, scattered logs, sticks, and minor silts and sands. Wood fragments were carefully separated from the peat in the field and appeared fresh when sampled, although rapidly became dark in color when exposed to the air. Vivianite, a bright blue powder-like hydrated iron phosphate mineral, associated with replacing organic materials such as wood or bones, was also present throughout the sample. The presence of vivianite should not skew the integrity of the age because it is a non-organic mineral. The vivianite and minor rootlets were microscopically removed from this and subsequent samples recorded in this table prior to sending to Beta Analytic for analysis. Petrographic analysis of Youngs Creek alluvial sand at a nearby site indicates the alluvium has a locally derived provenance containing volcanic lithic grains, microlitic grains of brown to red volcanic glass derived from the Mount Persis unit, minor sedimentary and metasedimentary lithic grains, monocrystalline and polycrystalline quartz, plagioclase, pyroxene, and hornblende. Other minor lithic grains observed included a few granitic lithic grains, mica, and metamorphic grains. Either the nature of this material, or the manner in which it was transported, gave gross IRSL age overestimates. Latitude and longitude are 47.806625°, -121.824848°; elevation = 530 ft (162 m).
102A	wood (unit Qc_{o})	-24.7	18,020 ±70	Standard radiometric analysis of wood from a 30-ft (9 m) tributary stream cutbank on the south side of the Skykomish River valley in the eastern portion of the Sultan quadrangle. Strata consist of compact, nonglacial stratified sands to cobble gravel overlying tan clay to silty fine sand and fine sandy silt with scattered organic debris (including logs). Sand and silt beds above the sample location were disturbed in a manner consistent with earthquake-induced liquefaction. Wood was obtained from a horizontally buried tree within the strata. Petrographic sand analysis indicates ancient SP alluvium overbank deposit with a granitic provenance; distinctly crystal-rich with abundant subangular monocrystalline quartz, plagioclase, pyroxene, hornblende, and K-spar with minor biotite and volcanic-lithic grains, as well as some brown volcanic glass likely derived from the nearby Mount Persis unit. Olympia age (unit Qc_{o}) is consistent with the sample stratigraphy and elevation relative to other ancient alluvial deposits. Latitude and longitude are 47.844671°, -121.778275°; elevation = 260 ft (79 m).
31AE	sticks/twigs (unit Qc_{ol})	-26.2	21,890 ±80	AMS analysis of small sticks and twigs collected from a cutbank along Elwell Creek in the western portion of the Sultan quadrangle. The cutbank exposes alluvial overbank silts, organic silts with peat-like beds in subhorizontal bedding planes. Petrographic and geochemical analysis of Elwell and Youngs Creek alluvial sands at nearby site 31AA (sec. 24, T27N R7E) indicate locally derived ancient alluvium; dominant grain types include Mount Persis unit volcanic-lithic grains, pyroxene, hornblende, monocrystalline and polycrystalline quartz, and plagioclase, and a few polycrystalline quartz, epidote, and sedimentary and metamorphic lithic grains. The data are consistent with an OSL/IRSL age of 22.9 to 23.8 ka (age site 44A, ~2,000 ft [610 m] downstream) and an IRSL age of 39.8 ka (age site 43D, 1,350 ft [412 m] upstream) from Olympia beds. Also see nearby Olympia age radiocarbon sites 31AB and 44A along Elwell Creek. Latitude and longitude are 47.825181°, -121.851627°; elevation = 130 ft [40 m].

Age Site	Analyzed organic material (geologic unit)	$^{13}C/^{12}C$ (o/oo)	Conventional radiocarbon age(yr BP)	Notes
31AB	sticks/twigs (unit Qc_{ol})	-27.2	22,020 ±100	AMS analysis of small sticks and twigs collected along a 40-ft (12 m)-high subvertical cutbank along Elwell Creek just north of the Elwell–Youngs Creek confluence in the western portion of the Sultan quadrangle. The cutbank exposed compact nonglacial ancient alluvial sediments containing organic-rich overbank silt with oxidized sand interbeds and some minor pebble gravel. Petrographic and geochemical analysis of Elwell and Youngs Creek alluvial sands at nearby site 31AA indicate locally derived ancient alluvium; dominant grain types include Mount Persis unit volcanic lithic grains, pyroxene, hornblende, monocrystalline and polycrystalline quartz, plagioclase, epidote, and sedimentary and metamorphic lithic grains. The data are consistent with an OSL/IRSL age of 22.9 to 23.8 ka (age site 44A, ~2,000 ft [610 m] downstream) from Olympia beds. Latitude and longitude are 47.821097°, -121.851377°; elevation = 150 ft.
44A	sticks (unit Qc_{o})	-28.1	23,760 ±100	Standard radiometric analysis of flattened sticks on nonglacial subhorizontal beds collected from an Elwell Creek cutbank in the western portion of the Sultan quadrangle. Minor moss was removed with a wire brush from the sticks prior to sending to Beta Analytic for analysis. Sample was from distinctly compact, stratified, crossbedded, orange-red sand with silt and clay and sticks locally associated with other plant debris. Sands were dominantly monocrystalline quartz, plagioclase, and K-spar with minor polycrystalline quartz, hornblende, and pyroxene with metamorphic, volcanic, and granitic grains. Both geochemical and petrographic analyses of the sand sample indicate a transitional ancient Elwell–Youngs Creek (unit Qc_{ol}) and Skykomish basin provenance (unit Qc_{o}). Some beds contain relatively high monocrystalline quartz content consistent with ancient Skykomish River basin provenance. The OSL/IRSL age of 22.9 to 23.8 ka 3 ft (1 m) above this radiocarbon sample is identical with the radiocarbon age (23.8 ka). Latitude and longitude are 47.830265°,-121.848240°; elevation = 105 ft (32 m).
10-49E	plant material (unit Qc_{o})	-27.1	24,790 ±170	AMS analysis of plant material in a cutbank outcrop along Skykomish River below the eastern end of the trailer park in the northwestern portion of the Sultan quadrangle. Sample is nonglacial sand, silt, and silt with disseminated dark organic material, including plant material and charcoal. Outcrop extends into the river and below summer water level and is undergoing active bank erosion. Sands at the site are monocrystalline quartz-rich with lesser, but significant, plagioclase, biotite, hornblende, and K-spar and distinct SP batholith provenance. Latitude and longitude are 47.845773°, -121.873481°; elevation = 75 ft (23 m). See the site 10-49E photo in Appendix 7 of Dragovich and others (2011b).
10-24D	charred organics (unit Qc_{o})	-24.9	>43,500	AMS analysis of charred organics in a 30-ft (9 m)-high extensive road cut outcrop located in the northeast corner of the Monroe quadrangle, ~1,250 ft (381 m) west of the Sultan quadrangle boundary. Sample is from nonglacial crossbedded and plane-bedded sands with stringers of disseminated dark organic material in the lower part of the exposure. Bedded fluvial channel gravels dominate the uppermost part of the outcrop. Coarse sand at the site contains significant monocrystalline quartz, distinct granitic lithic grains, and some metamorphic and sedimentary lithic grains. Monocrystalline quartz is significantly more abundant than polycrystalline quartz, suggesting a nonglacial SP provenance, and is petrographically very similar to modern Skykomish alluvium. Other analyzed sands contained a higher percentage of more diverse lithic grain types, including slightly more serpentinite, metasedimentary lithic clasts, and polycrystalline quartz. We suspect these beds contain older Quaternary sediment due to the incorporation of emerging local highlands detritus, including nearby Western mélange belt rocks, by the ancient Skykomish River. An OSL sample was taken 3 ft (1 m) from the radiocarbon sample at 10-24D and provided an age of 51.1 ±3.84 ka (Dragovich and others, 2011b). Latitude and longitude are 47.844443°, -121.881831°; elevation = 300 ft (91 m). See the site 10-24D photo in Appendix 7 of Dragovich and others (2011b).
31E	wood (unit Qgl_{v})	-27.4	>43,500	AMS analysis of a single small carbonized wood fragment in laminated clay, silt, and sand with scattered gravel. The sample was obtained in an erosional cutbank exposing Vashon advance glaciolacustrine deposits (unit Qgl_{v}) along Youngs Creek east of the Elwell and Youngs Creek confluence in the western portion of the Sultan quadrangle. The subrounded edges of wood fragment indicate a detrital origin, possibly from an older ancient nonglacial unit (example, unit Qc_{pf}). A nearby medium sand sample of unit Qga_{v} was analyzed geochemically and petrographically and was found to have a distinct northern polymictic provenance that contained a variety of lithic grains of intrusive, volcanic, sedimentary, and metamorphic grain types (~70%), with some monocrystalline quartz, plagioclase, polycrystalline quartz, and true granitic lithic grains and a few grains of hornblende, meta-argillite, pyroxene, and rare biotite, but did not contain free K-spar grains. Latitude and longitude are 47.809605°, -121.843588°; elevation = 250 ft (76 m).
41P	wood (unit Qc_{pf})	-23.9	>43,500	AMS analysis of a wood fragment located along a railroad cut outcrop paralleling US 2 on the north side of the Skykomish River valley in the northwest portion of the Sultan quadrangle. Exposed strata include very compact light brown silt with scattered pebble gravel and thin interbeds of sand with sparse disseminated dark organic material. These strata display intense liquefaction features. Deposits have a micaceous and quartz-rich nonglacial provenance consistent with SP. See IRSL age site 45B (>300 ka) from unit Qc_{pf}. 1.7 mi (2.7 km) northeast of site 41P. Latitude and longitude are 47.8511789°, -121.857613; elevation = 100 ft (31 m).

Appendix B. Infrared and Optically Stimulated Luminescence Age Data for Quaternary Nonglacial Deposits

Luminescence ages for sediment samples are presented in Table B1. See Dragovich and others (2011b) for a discussion of the infrared stimulated luminescence and optically stimulated luminescence methodologies. The petrographic and geochemical examination of the sands from the age sites, combined with deposit stratigraphy, show units Qc$_o$ and Qc$_{pf}$ are ancient Snoqualmie River alluvium with a strong Cascade batholith or an ancient Skykomish River basin provenance (SP, Table 1). Conversely, unit Qc$_{ol}$ is ancient Youngs Creek–Elwell Creek sediment with a local provenance (LP, Table 1). The Pleistocene nonglacial character of the sampled SP and LP sediments, combined with the other age information, support our correlation of the sampled strata with the Olympia nonglacial interval for most samples. (We use the informal term 'Olympia beds' for the "deposits of the Olympia nonglacial" of Pessl and others [1989].) Many of the luminescence ages are corroborated by adjacent or nearby radiocarbon ages (Appendix A), with some notable exceptions as discussed below. See *Description of Map Units* for further information and Appendix C for nearby sand geochemistry.

Table B1. Infrared stimulated luminescence (IRSL) and optically stimulated luminescence (OSL) data from the Sultan 7.5-minute quadrangle. Table B1 provides elemental concentrations, cosmic and total dose rates, equivalent doses, and ages from IRSL (fine-grained feldspars) and OSL (quartz) fractions. Sample identifiers are bold. See map sheet for sample locations. Gy, Gray (unit of absorbed radiation); ka, 1,000 years.

Sample ID/ information	Water content (%)[a]	K (%)[b]	U (ppm)[b]	Th (ppm)[b]	Cosmic dose[c] additions (Gy/ka)	Total dose rate (Gy/ka)	Equivalent dose (Gy)	n[d]	Age (ka)[e]
43B	7(35)	1.85 ±0.05	1.44 ±0.19	6.09 ±0.55	0.13 ±0.01	3.10 ±0.16[f]	346 ±17.9[f]	– – –	112 ±7.60[f]
Stratified alluvial LP sand (unit Qa) along Youngs Creek in the central part of the Sultan quadrangle. We obtained a radiocarbon age of 9,440 ±40 yr BP (9.44 ka) at age site 40D from wood fragments in peat stratigraphically 3 ft (1 m) below the IRSL sample. The anomalously old age for the alluvium suggests mass deposition for the sands, resulting in an old age. See site 40D (Appendix C) for geochemical analyses at this location. The sample was dominated by volcanic-lithic grains and plagioclase and thus contains very few K-spar grains for IRSL analyses. It is likely the signal was contaminated to some degree by unstable plagioclase emissions. We also had some evidence for partial bleaching in the IRSL data, but the simplest and most sensible solution was that the lithic grains carried a large residual luminescence signal that was not bleached away at transport. Latitude and longitude are 47.806625°, -121.824848°; elevation = 530 ft (162 m).									
43D	12(28)	2.12 ±0.04	1.38 ±0.21	7.07 ±0.15	0.12 ±0.01	2.47 ±0.08[f]	98.3 ±4.33[f]	– – –	39.8 ±1.94[f]
Overbank LP sand with silt (unit Qc$_{ol}$) located along Elwell Creek, north of the Elwell–Youngs Creek confluence in the eastern portion of the Sultan quadrangle. Site is along a substantial erosional cutbank exposing stratified cobble gravel, sand, and silt with crossbedding and scours. We obtained a radiocarbon age at age site 31AB of 22,020 ±100 yr BP (22.0 ka) in similar strata west of the site, confirming the sediments are correlative with the Olympia beds. See site 43D in Appendix C for geochemical analysis. Latitude and longitude are 47.821121°, -121.850454°; elevation = 145 ft (44 m).									
44A	12(41)	1.93 ±0.05	1.40 ±0.15	6.45 ±0.47	0.12 ±0.01	2.29 ±0.10 3.09 ±0.13[f]	52.4 ±3.98 73.4 ±4.70[f]	21(30) – – –	22.9 ±2.00 23.8 ±1.83[f]
Crossbedded, oxidized SP sand, silt, and clay (unit Qc$_o$) along Elwell Creek in the eastern portion of the Sultan quadrangle. Site is along an erosional cutbank and exposes stratified, extremely compact, crossbedded orange-red sediments with scattered flattened sticks and plant debris on subhorizontal beds. We obtained a radiocarbon age of 23,760 ±100 yr BP (23.76 ka) 3 ft (1 m) below this site, confirming the sediments are correlative with the Olympia beds (Appendix A). See site 44A in Appendix C for geochemical analysis. Latitude and longitude of site are 47.830265°, -121.848240°; elevation = 105 ft (32 m).									
44B	24(64)	1.70 ±0.04	1.11 ±0.09	6.29 ±0.21	0.19 ±0.02	2.55 ±0.06[f]	187 ±5.42[f]	– – –	73.3 ±2.67[f]
Brown SP silty sand to sandy silt with pebble gravel and interbedded with organic-rich silt alluvium (unit Qc$_o$) and some moderately sorted beds of silt, sand, and pebble gravel along Ben Howard Road in the northern portion of the Sultan quadrangle. Provenance and stratigraphy at this site, along with surrounding Olympia bed age sites (~15–60 ka), indicate these compact and organic deposits are anomalously old. The poor sorting and pebble angularity of some beds suggest deposition by mass wasting probably resulted in only partial bleaching, and thus an anomalously old age for the OSL. See nearby site 44A in Appendix C for geochemical analysis. Latitude and longitude of site are 47.842756°, -121.865931°; elevation = 100 ft (31 m).									

Sample ID/ information	Water content (%)[a]	K (%)[b]	U (ppm)[b]	Th (ppm)[b]	Cosmic dose[c] additions (Gy/ka)	Total dose rate (Gy/ka)	Equivalent dose (Gy)	n[d]	Age (ka)[e]
44D	12(42)	1.90 ±0.04	1.53 ±0.11	5.57 ±0.14	0.14 ±0.01	3.04 ±0.05[f]	112 ±4.03[f]	– – –	36.8 ±1.47[f]
Oxidized orange to grey-tan, fine, micaceous sand and silt SP alluvium (unit Qc$_o$) displaying distinct liquefaction features (including ballooned or chaotic rootless bedding). See nearby site 44A in Appendix C for geochemical analysis. Latitude and longitude of site are 47.838795°, -121.858958°; elevation = 300 ft (91 m).									
44E	6(37)	1.40 ±0.02	1.50 ±0.10	4.16 ±0.22	0.18 ±0.01	2.54 ±0.07[f]	62.3 ±2.87[f]	– – –	24.5 ±1.31[f]
Compact stratified SP sand and silt with very thin organic beds (unit Qc$_o$) exposed in a trench adjacent to Ben Howard Road on the south side of the Skykomish River in the northern portion of the Sultan quadrangle. Thin sand dikes cut the strata locally as illustrated in Appendix E. See site 44E in Appendix C for geochemical analysis. Latitude and longitude of site are 47.847263°, -121.830148°; elevation = 240 ft (73 m).									
44G	1(24)	2.32 ±0.05	2.79 ±0.18	8.07 ±0.37	0.26 ±0.02	4.36 ±0.15[f]	6.37 ±0.33[f]	– – –	1.46 ±0.09[f]
SP sand from a modern channel bar (unit Qa) on the south bank of the Skykomish River south of the City of Sultan. The sample was taken from the top 8 in. (20 cm) of a modern point bar on the Skykomish River, a few meters above mean river level, and was used as a 'zero age' baseline for IRSL measurements (see nearby site 44F, sec. 5, T27N R8E, and Appendix C for geochemical analysis of modern Skykomish River alluvium). Latitude and longitude of site are 47.859263°, -121.809993°; elevation = 100 ft (31 m).									
45A	4(28)	1.34 ±0.02	1.19 ±0.07	3.03 ±0.13	0.16 ±0.01	1.75 ±0.04 2.32 ±0.05[f]	50.8 ±6.09 >500[f]	13(48) – – –	29.0 ±1.88 >215[f]
Compact and stratified micaceous SP silt to fine- to coarse-grained sand (unit Qc$_o$); distinctly tilted to the northwest with probable liquefaction features. Site located west of the Sultan River in the northwest portion of the Sultan quadrangle along Reiner Road. We tentatively correlate the strata with the Olympia beds, given the preferred quartz OSL age and the occurrence of Olympia beds along the Monroe syncline west of the area (Dragovich and others, 2011a,b). See site 45A in Appendix C for geochemical analysis. Latitude and longitude of site are 47.864477°, -121.837074°; elevation = 290 ft (88 m).									
45B	7(31)	0.92 ±0.03	0.87 ±0.12	2.90 ±0.31	0.13 ±0.01	1.71 ±0.10[f]	>500[f]	– – –	>300[f]
Thickly bedded silty fine- to medium-grained sand with scattered local coarse sand-pebble beds and orange silt beds (unit Qc$_{pf}$) along a Sultan River steep erosional cutbank west of the city of Sultan in the northwest portion of the Sultan quadrangle. Pebbly sand and silt interbeds are as much as 4 in. (10 cm) thick. See sites 41B and 45B in Appendix C for geochemical analyses at this location. Latitude and longitude of site are 47.866326°, -121.829825°; elevation = 120 ft (37 m).									

[a] Field moisture, with figures in parentheses indicating the complete saturation percent. Ages calculated using approximately 60% of saturation values.

[b] Analyses obtained using laboratory gamma spectrometry (high-resolution Ge detector).

[c] Cosmic doses and attenuation with depth were calculated using the methods of Prescott and Hutton (1994). See text for details.

[d] Number of replicated equivalent dose (De) estimates to calculate the mean. Figures in parentheses indicate total number of measurements made, including failed runs.

[e] Dose rate and age for 250–180 micron–sized quartz sand. Linear + exponential fit used on equivalent dose, with single aliquot regeneration. Errors to one sigma.

[f] Feldspar from fine grains of 4–11 micron polymineral silt. Exponential fit used for multiple aliquot additive doses. Errors to one sigma. Fade tests indicate no correction.

Appendix C. Geochemical Data

Whole-rock major- and trace-element analyses were run on glacial and nonglacial sands and rock using x-ray fluorescence (XRF) and inductively coupled plasma source mass spectrometry (ICP-MS) at the GeoAnalytical Laboratory at Washington State University (WSU). Grinding of samples was completed at WSU using a tungsten carbide mill for XRF analyses and iron equipment for ICP-MS analyses. Estimates of accuracy and precision, as well as discussion of analytical methods for both XRF and ICP-MS at WSU, are given by Johnson and others (1999) and Knaack and others (1994), respectively. We provided a better comparison between Quaternary sands by sieving with 2 mm (no. 10) and 0.075 mm (no. 200) sieves at the DNR laboratory in Olympia, Wash., prior to grinding, so that only the sand-size fraction was chemically analyzed. Although most samples were well sorted sand, sieving eliminated erroneous results that may occur from inclusion of fines and pebbles in the sand samples.

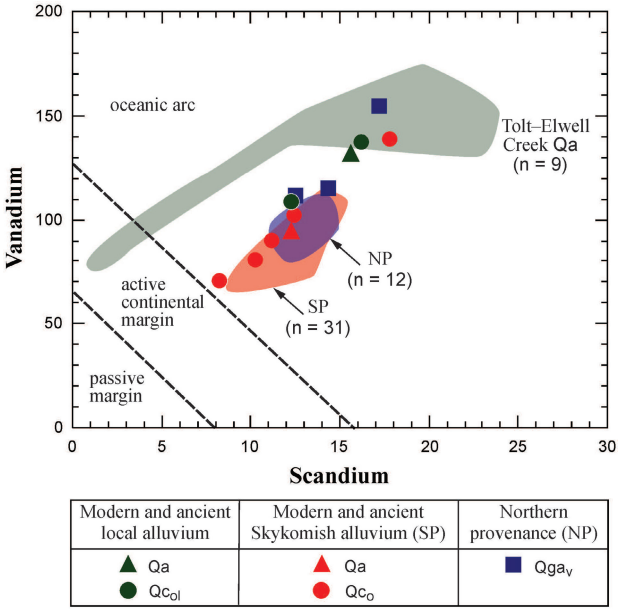

Figure C1. V vs. Sc provenance diagram of Bhatia and Crook (1986) for Quaternary samples. SP, Skykomish and Snoqualmie River basin provenance. Fields for northern provenance, NP, and Tolt–Elwell Creek Qa are defined by data from Dragovich and others (2010a,b, 2011a,b, 2012). Data normalized loss on ignition (LOI)-free before being plotted.

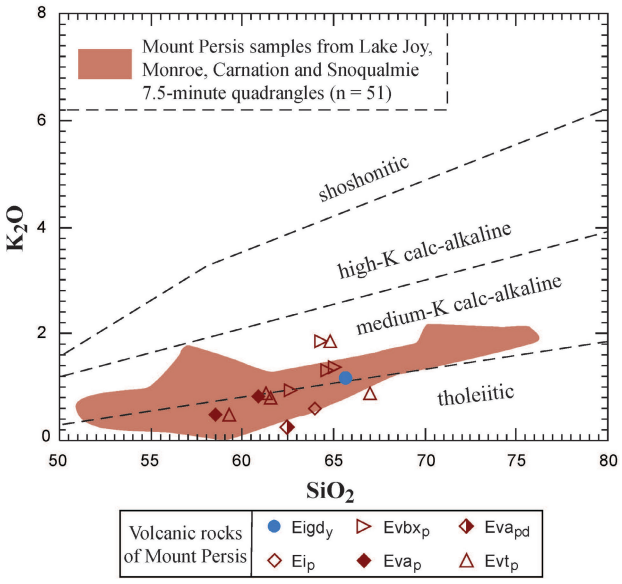

Figure C2. K_2O vs. SiO_2 diagram for volcanic rocks of Mount Persis (Tabor and others, 1993) including Youngs Creek intrusive complex. Data that define the Mount Persis unit field are taken from Dragovich and others (2009a,b, 2010a,b, 2011a,b, 2012). Data normalized LOI-free before being plotted.

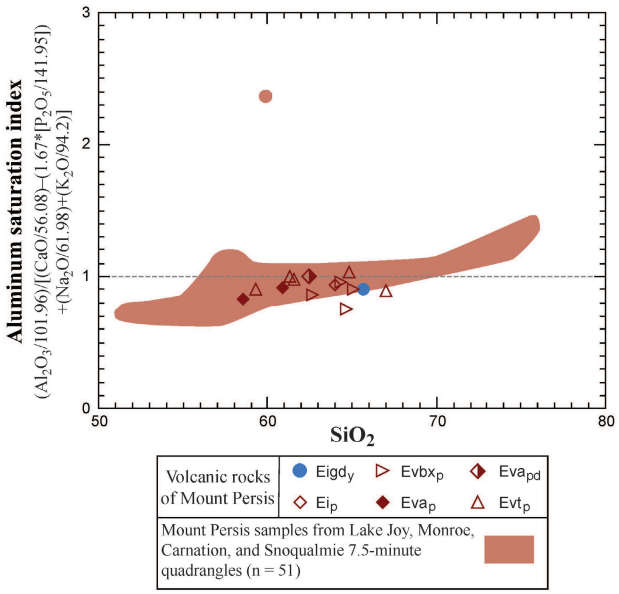

Figure C3. Aluminum saturation index vs. SiO_2 diagram for volcanic rocks of Mount Persis. Aluminum saturation index calculated following the method of Frost and others (2001). Mount Persis unit fields are taken from Dragovich and others (2009a,b, 2010a,b, 2011a,b, 2012). Data normalized LOI-free before being plotted.

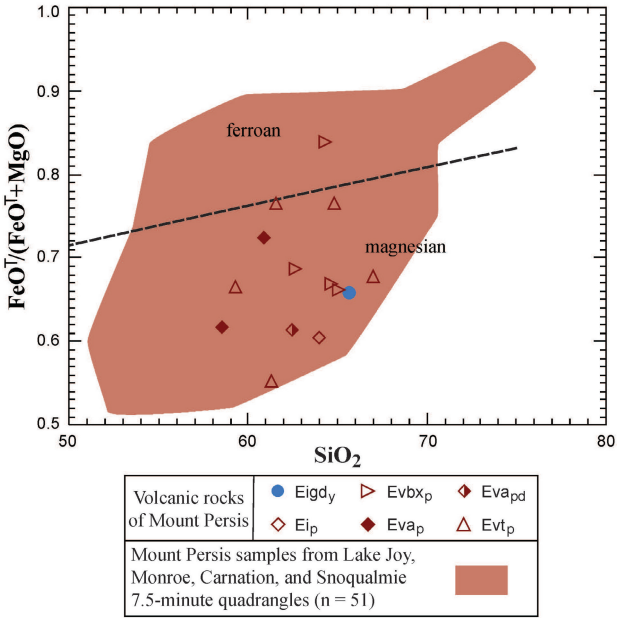

Figure C4. $FeO^T/(FeO^T+MgO)$ vs. SiO_2 diagram from Frost and others (2001) for volcanic rocks of Mount Persis including Youngs Creek intrusive complex. Data that define the Mount Persis unit field are taken from Dragovich and others (2009a,b, 2010a,b, 2011a,b, 2012). Data normalized LOI-free before being plotted.

Table C1. Normalized x-ray fluorescence data from the Sultan 7.5-minute quadrangle. All data listed below have been normalized to 100% on a LOI (loss on ignition)-free basis. Table C2 contains the raw data values. See major caption at top of Appendix C for additional information.

Sample	1A	3W	5E	5N	7B	7T	11G[Z]	13AA	14P	15M	17F	18Q*	20J	30L	31AA	32R	34S	40R	41B	43D[L]	44A[L,R]	44E[L]	44F	45A[L]	45B[L]	47G[Z]	50S
Lat. Long.	47.7935 -121.8470	47.8003 -121.8608	47.7565 -121.8304	47.7574 -121.8229	47.7583 -121.8180	47.7699 -121.8097	47.7988 -121.7166	47.7763 -121.7876	47.8088 -121.8325	47.7559 -121.7611	47.8148 -121.7759	47.8082 -121.7703	47.8009 -121.7781	47.7877 -121.8683	47.8206 -121.8519	47.8070 -121.8579	47.7942 -121.8665	47.8040 -121.8235	47.8664 -121.8298	47.8211 -121.8505	47.8303 -121.8482	47.8473 -121.8301	47.8596 -121.8125	47.8645 -121.8371	47.8663 -121.8298	47.7686 -121.8080	47.8450 -121.7696
Unit	$Evbx_p$	Eva_p	Evt_p	Evt_p	Evt_p	Eva_{pd}	$Eigd_y$	Qga_v	$Evbx_p$	Qga_v	Evt_p	$Evbx_p$	Qga_v	$Evbx_p$	Qco_l	Evt_p	Eva_p	Qa	Qc_o	Qco_l	Qc_o	Qc_o	Qa	Qc_o	Qc_o	Ei_p	$KJmv_w$
SiO_2	64.69	58.54	66.99	61.29	59.27	62.48	65.63	68.21	65.07	72.73	61.58	62.68	70.74	64.32	66.35	64.81	60.92	65.74	72.49	69.96	72.07	74.54	71.29	72.15	73.65	64.02	50.04
TiO_2	0.60	0.94	0.67	0.80	1.08	0.78	0.77	1.03	0.69	0.74	0.80	0.93	0.67	0.69	0.83	0.77	0.93	0.88	0.41	0.73	0.57	0.55	0.52	0.70	0.34	0.68	2.21
Al_2O_3	15.57	16.78	14.24	17.04	17.38	17.49	15.86	14.37	16.53	14.23	17.92	15.95	15.05	17.05	17.14	16.73	17.74	17.45	14.34	14.98	13.60	13.86	14.52	13.09	14.15	16.20	18.49
FeO^T	4.43	7.21	5.58	5.78	7.15	5.49	4.61	5.95	4.17	4.46	6.43	6.03	4.58	5.60	6.04	5.49	6.25	6.13	3.23	4.27	3.76	3.89	3.91	5.48	2.73	5.30	9.49
MnO	0.14	0.11	0.09	0.12	0.13	0.09	0.06	0.11	0.11	0.08	0.14	0.11	0.11	0.11	0.11	0.06	0.11	0.10	0.07	0.07	0.06	0.09	0.08	0.10	0.05	0.06	0.25
MgO	2.20	4.48	2.65	4.67	3.59	3.47	2.39	2.71	2.14	1.79	1.98	2.76	1.78	1.07	2.32	1.69	2.38	2.50	1.65	2.03	1.88	1.45	1.89	2.44	1.45	3.48	5.89
CaO	7.41	7.62	4.60	6.35	7.04	7.54	5.38	3.89	5.80	2.15	5.78	6.08	2.72	5.57	2.85	3.49	6.39	3.17	2.90	3.52	3.40	1.78	2.98	2.21	2.63	6.36	5.43
Na_2O	3.52	3.64	4.11	2.87	3.68	2.24	4.00	2.68	3.97	2.55	4.34	4.15	2.88	3.56	2.68	4.88	4.27	2.85	3.40	3.08	3.23	2.50	3.19	2.58	3.43	3.18	3.37
K_2O	1.33	0.50	0.90	0.89	0.48	0.27	1.19	0.92	1.37	1.19	0.82	0.95	1.40	1.88	1.56	1.87	0.85	1.02	1.42	1.27	1.34	1.28	1.53	1.11	1.49	0.60	3.93
P_2O_5	0.10	0.17	0.16	0.19	0.19	0.16	0.12	0.11	0.15	0.08	0.20	0.35	0.09	0.15	0.12	0.20	0.15	0.15	0.09	0.08	0.09	0.07	0.09	0.14	0.09	0.11	0.90
Total	100.00	100.00	100.00	100.00	100.00	100.00	100.00	100.00	100.00	100.00	100.00	100.00	100.00	100.00	100.00	100.00	100.00	100.00	100.00	100.00	100.00	100.00	100.00	100.00	100.00	100.00	100.00
LOI	3.63	2.80	5.84	8.26	1.57	9.54	1.73	3.15	2.49	4.70	7.57	2.41	3.13	6.70	5.63	1.93	1.13	5.48	1.54	3.35	2.21	4.00	2.06	4.06	1.62	4.47	5.15
Cr	50	114	82	133	36	95	21	346	45	79	3	93	108	9	87	6	11	81	65	94	73	121	76	161	49	64	33
V	83	153	79	152	177	115	116	154	103	111	117	127	115	57	137	74	141	131	80	108	90	102	94	138	70	118	126
Ga	18	18	15	18	20	24	18	16	18	15	22	24	15	20	19	21	20	19	14	16	14	14	15	13	14	18	20
Cu	65	95	81	395	84	53	15	39	88	48	66	72	40	31	57	25	68	63	25	39	30	32	37	41	18	74	28
Zn	37	75	46	84	60	67	27	75	62	60	94	83	64	59	77	71	73	97	51	60	51	52	67	76	49	56	82

* average of two chemical analyses
T all iron reported as Fe^{2+}
Z U-Pb zircon sample
L OSL/IRSL age sample
R Radiocarbon age sample

Table C2. Unnormalized x-ray fluorescence data from the Sultan 7.5-minute quadrangle. Table C1 contains the data that have been normalized on a LOI-free basis. See major caption at top of Appendix C for additional information. Some geochemical sample locations are shown on map.

Sample	1A	3W*	5E	5N	7B	7T	11GZ	13AA	14P	15M	17F	18Q*	20J	30L	31AA	32R	34S	40R	41B	43D^{L}	44A^{L,R}	44E^{L}	44F	45AL	45BL	47G^{Z}	50S
Lat. Long.	47.7935 -121.8470	47.8003 -121.8608	47.7565 -121.8304	47.7574 -121.8229	47.7583 -121.8180	47.7699 -121.8097	47.7988 -121.7166	47.7763 -121.7876	47.8088 -121.8325	47.7559 -121.7611	47.8148 -121.7759	47.8082 -121.7703	47.8009 -121.7781	47.7877 -121.8683	47.8206 -121.8519	47.8070 -121.8579	47.7942 -121.8665	47.8040 -121.8235	47.8664 -121.8298	47.8211 -121.8505	47.8303 -121.8482	47.8473 -121.8301	47.8596 -121.8125	47.8645 -121.8371	47.8663 -121.8298	47.7686 -121.8080	47.8450 -121.7696
Unit	Evbxp	Evap	Evtp	Evtp	Evtp	Evapd	Eigdy	Qgav	Evbxp	Qgav	Evtp	Evbxp	Qgav	Evbxp	Qcol	Evtp	Evap	Qa	Qco	Qcol	Qco	Qco	Qa	Qco	Qco	Eip	KJmv
SiO_2	62.49	57.10	63.18	56.32	58.25	56.42	64.56	65.81	62.91	69.11	56.85	61.17	68.13	59.85	62.29	63.29	60.08	61.98	71.17	67.82	70.59	71.22	69.95	68.88	72.45	61.43	47.33
TiO_2	0.58	0.91	0.63	0.73	1.07	0.71	0.75	1.00	0.67	0.70	0.74	0.91	0.64	0.64	0.78	0.75	0.92	0.83	0.40	0.71	0.55	0.53	0.51	0.66	0.33	0.65	2.09
Al_2O_3	15.04	16.37	13.43	15.66	17.08	15.79	15.60	13.87	15.98	13.52	16.55	15.56	14.49	15.86	16.09	16.34	17.50	16.45	14.07	14.52	13.32	13.24	14.25	12.50	13.92	15.55	17.49
FeO^{T}	4.28	7.03	5.26	5.31	7.03	4.96	4.53	5.74	4.04	4.24	5.94	5.89	4.41	5.21	5.67	5.37	6.16	5.78	3.17	4.14	3.68	3.72	3.83	5.23	2.69	5.08	8.98
MnO	0.13	0.11	0.09	0.11	0.12	0.08	0.06	0.11	0.11	0.08	0.13	0.11	0.10	0.10	0.10	0.06	0.11	0.10	0.07	0.06	0.06	0.09	0.08	0.10	0.05	0.06	0.24
MgO	2.13	4.37	2.50	4.29	3.52	3.13	2.35	2.62	2.07	1.70	1.83	2.70	1.71	1.00	2.18	1.65	2.35	2.35	1.62	1.97	1.84	1.39	1.85	2.33	1.43	3.34	5.57
CaO	7.16	7.43	4.34	5.83	6.92	6.81	5.29	3.76	5.61	2.04	5.34	5.93	2.62	5.18	2.68	3.41	6.31	2.99	2.85	3.41	3.33	1.70	2.92	2.11	2.58	6.10	5.13
Na_2O	3.40	3.55	3.87	2.63	3.62	2.03	3.94	2.59	3.83	2.42	4.01	4.05	2.77	3.31	2.52	4.77	4.21	2.69	3.34	2.98	3.17	2.39	3.13	2.46	3.38	3.05	3.19
K_2O	1.28	0.49	0.85	0.81	0.48	0.24	1.17	0.88	1.33	1.13	0.76	0.92	1.35	1.75	1.47	1.82	0.84	0.97	1.39	1.23	1.31	1.22	1.50	1.06	1.47	0.58	3.72
P_2O_5	0.10	0.16	0.15	0.18	0.19	0.14	0.12	0.11	0.15	0.08	0.18	0.35	0.09	0.14	0.11	0.20	0.15	0.14	0.09	0.08	0.09	0.06	0.09	0.14	0.09	0.10	0.85
Total	96.59	97.54	94.31	91.90	98.27	90.31	98.37	96.48	96.68	95.02	92.33	97.59	96.30	93.04	93.89	97.66	98.62	94.27	98.17	96.94	97.95	95.55	98.12	95.46	98.38	95.95	94.58
LOI	3.63	2.80	5.84	8.26	1.57	9.54	1.73	3.15	2.49	4.70	7.57	2.41	3.13	6.70	5.63	1.93	1.13	5.48	1.54	3.35	2.21	4.00	2.06	4.06	1.62	4.47	5.15
Cr	48	111	77	122	35	86	21	334	44	75	3	91	104	8	82	5	11	76	64	92	71	115	74	154	48	62	31
V	80	149	75	140	174	104	114	149	100	106	108	123	110	53	128	72	139	124	79	105	88	97	92	132	69	113	119
Ga	17	18	14	17	20	22	17	15	17	15	20	24	14	19	17	21	19	18	13	16	14	14	15	13	14	17	19
Cu	63	93	76	363	83	48	15	37	85	45	61	70	39	29	54	25	67	59	24	38	29	31	37	39	18	71	27
Zn	36	73	43	77	59	60	27	72	60	57	86	80	62	55	72	69	72	91	50	59	50	50	65	72	48	53	77

* average of two chemical analyses
T all iron reported as Fe^{2+}
Z U-Pb zircon sample
L OSL/IRSL age sample
R Radiocarbon age sample

Table C3. Normalized inductively coupled plasma mass spectrometry data from the Sultan 7.5-minute quadrangle. All data listed below have been normalized to 100% on a LOI-free basis. Table C4 contains the raw data values. See major caption at top of Appendix C for additional information. Some geochemical sample locations are shown on map.

Sample	1A	3W*	5E	5N	7B	7T	11G[Z]	13AA	14P	15M	17F	18Q*	20J	30L	31AA	32R	34S	40R	41B	43D[L]	44A[L,R]	44E[L]	44F	45A[L]	45B[L]	47G[Z]	50S
Lat. Long.	47.7935 -121.8470	47.8003 -121.8608	47.7565 -121.8304	47.7574 -121.8229	47.7583 -121.8180	47.7699 -121.8097	47.7988 -121.7166	47.7763 -121.7876	47.8088 -121.8325	47.7559 -121.7611	47.8148 -121.7759	47.8082 -121.7703	47.8009 -121.7781	47.7877 -121.8683	47.8206 -121.8519	47.8070 -121.8579	47.7942 -121.8665	47.8040 -121.8235	47.8664 -121.8298	47.8211 -121.8505	47.8303 -121.8482	47.8473 -121.8301	47.8596 -121.8125	47.8645 -121.8371	47.8663 -121.8298	47.7686 -121.8080	47.8450 -121.7696
Unit	Evbx$_p$	Eva$_p$	Evt$_p$	Evt$_p$	Evt$_p$	Eva$_{pd}$	Eigd$_y$	Qga$_v$	Evbx$_p$	Qga$_v$	Evt$_p$	Evbx$_p$	Qga$_v$	Evbx$_p$	Qc$_{ol}$	Evt$_p$	Eva$_p$	Qa	Qc$_o$	Qc$_{ol}$	Qc$_o$	Qc$_o$	Qa	Qc$_o$	Qc$_o$	Ei$_p$	KJmv ...
La	17.3	13.9	11.2	12.0	11.7	11.8	16.1	15.9	15.3	25.3	24.3	24.9	13.0	14.0	73.7	14.6	11.6	13.9	15.5	15.2	11.0	13.7	12.5	13.4	10.8	12.5	8.6
Ce	31.2	29.2	24.8	27.0	25.4	25.7	34.6	31.2	31.7	55.2	47.6	50.9	26.9	28.3	148.4	29.5	27.7	29.0	33.6	32.6	21.9	28.0	25.4	29.0	21.5	24.5	17.0
Pr	4.0	3.7	3.2	3.5	3.4	3.3	4.4	3.8	4.2	6.9	5.7	6.3	3.5	3.6	15.3	3.7	2.8	3.6	3.9	4.0	2.7	3.5	3.2	3.3	2.7	3.7	2.1
Nd	15.7	15.1	13.2	14.4	14.5	13.7	18.3	14.8	17.3	27.2	21.6	25.0	14.1	14.3	53.8	14.7	11.2	14.2	15.3	16.2	10.5	13.8	12.6	13.0	10.7	15.6	8.5
Sm	3.4	3.6	3.1	3.5	3.7	3.4	4.4	3.3	3.9	5.9	4.6	5.6	3.4	3.4	9.2	3.4	2.6	3.2	3.5	3.7	2.3	3.1	2.9	2.9	2.5	3.9	1.9
Eu	1.0	1.2	1.1	1.2	1.2	1.1	1.1	1.0	1.4	1.7	1.3	1.6	1.2	0.9	2.8	1.0	0.8	0.9	1.0	1.1	0.8	1.0	0.9	0.9	0.8	1.2	0.7
Gd	3.4	3.6	3.2	3.5	3.9	3.4	4.5	3.2	3.8	5.3	4.3	5.6	3.5	3.3	7.5	3.4	2.6	3.2	3.4	3.6	2.3	3.0	2.8	2.7	2.5	4.3	1.9
Tb	0.6	0.6	0.5	0.6	0.6	0.6	0.8	0.5	0.6	0.8	0.7	0.9	0.6	0.6	1.1	0.6	0.5	0.6	0.6	0.6	0.4	0.5	0.5	0.5	0.4	0.7	0.3
Dy	3.3	3.7	3.1	3.3	3.9	3.5	4.6	3.3	3.6	4.7	4.1	5.7	3.6	3.3	6.3	3.6	2.8	3.8	3.6	3.7	2.5	3.1	2.9	2.8	2.8	4.4	1.9
Ho	0.7	0.7	0.6	0.7	0.8	0.7	0.9	0.7	0.7	0.9	0.8	1.2	0.8	0.7	1.2	0.8	0.6	0.8	0.7	0.7	0.5	0.6	0.6	0.6	0.6	0.9	0.4
Er	1.8	2.0	1.7	1.8	2.1	1.9	2.5	1.8	1.9	2.4	2.2	3.2	2.0	1.8	3.1	2.1	1.6	2.4	2.1	2.1	1.4	1.7	1.6	1.5	1.7	2.5	1.1
Tm	0.3	0.3	0.2	0.3	0.3	0.3	0.4	0.3	0.3	0.3	0.3	0.5	0.3	0.3	0.4	0.3	0.2	0.3	0.3	0.3	0.2	0.3	0.2	0.2	0.3	0.4	0.2
Yb	1.6	1.8	1.5	1.6	1.9	1.8	2.3	1.7	1.7	2.1	2.1	3.0	1.8	1.7	2.7	2.0	1.5	2.2	1.9	1.9	1.4	1.6	1.5	1.5	1.6	2.3	1.0
Lu	0.3	0.3	0.2	0.3	0.3	0.3	0.3	0.3	0.3	0.3	0.3	0.5	0.3	0.3	0.4	0.3	0.2	0.3	0.3	0.3	0.2	0.3	0.2	0.2	0.3	0.4	0.2
Ba	428	181	149	146	172	36	167	295	258	202	412	462	216	222	2339	326	394	473	442	349	475	347	376	508	470	434	500
Th	4	2	1	1	2	2	5	4	2	2.4	6	5	2	3	9	3	3	4	4	3	3	3	3	4	3	3	3
Nb	7	9	7	9	8	8	8	9	9	17.92	12	13	8	7	98	8	7	6	9	9	4	7	6	5	5	5	3
Y	19	19	16	17	20	17	24	17	19	22.98	22	30	19	17	30	19	14	21	19	19	13	16	15	14	15	24	10
Hf	4	4	3	3	3	3	4	4	4	5.95	5	6	4	4	8	3	4	4	4	4	3	4	3	3	3	3	2
Ta	0.63	0.63	0.51	0.6	0.55	0.56	0.7	0.71	0.68	1.19	0.94	0.99	0.58	0.58	6.16	0.58	0.5	0.46	0.69	0.65	0.29	0.56	0.45	0.37	0.36	0.35	0.24
U	0.87	0.57	0.31	0.56	0.67	0.49	1.77	1.27	0.69	0.82	1.47	1.66	0.69	1.1	2.37	0.93	0.97	1.2	1.23	1.03	1.2	1.03	1.08	1.41	1.2	1.03	0.9
Pb	3.48	2.08	1.12	1.21	2.52	2.88	3.19	2.74	2.84	3.71	3.2	3.82	2.7	2.49	3.89	18.81	5.19	8.45	5.86	6.32	7.78	4.65	4.56	8.16	8.87	6.44	7.87
Rb	26.5	4.4	18.2	20.7	6.5	5.8	28.4	28.4	16.4	13.7	48.1	41.8	17.3	11.6	72.4	21.7	26.8	40.7	43.2	24.3	39	27.2	29.6	35.4	41.9	30.6	41.3
Cs	0.13	0.19	0.53	0.38	0.08	1.91	0.69	0.1	0.27	0.63	0.48	0.3	0.32	0.31	1.75	0.84	0.75	1.87	1.96	1.1	1.78	0.79	0.72	1.54	2.15	1.46	1.9
Sr	327	315	216	184	293	213	262	277	396	442	232	242	321	289	599	265	205	272	199	282	316	253	249	229	267	185	327
Sc	12.5	19	14.1	16.7	18.7	15.9	13.9	12.3	10.3	14.8	9.7	11.9	14.6	14.1	14.1	17.2	12.5	14.3	16.2	15.6	10.2	12.2	11.1	12.4	12.2	17.8	8.2
Zr	138	141	120	135	124	132	148	151	138	256	214	253	134	154	383	126	133	138	154	154	93	137	121	113	100	93	71

* average of two chemical analyses
[Z] U-Pb zircon sample
[L] OSL/IRSL age sample
[R] Radiocarbon age sample

Table C4. Unnormalized inductively coupled plasma mass spectrometry data from the Sultan 7.5-minute quadrangle. See major caption at top of Appendix C for additional information. Some geochemical sample locations are shown on map.

Sample	1A	3W*	5E	5N	7B	7T	11G[Z]	13AA	14P	15M	17F	18Q*	20J	30L	31AA	32R	34S	40R	41B	43D[L]	44A[L,R]	44E[L]	44F	45A[L]	45B[L]	47G[Z]	50S
Lat. Long.	47.7935 -121.8470	47.8003 -121.8608	47.7565 -121.8304	47.7574 -121.8229	47.7583 -121.8180	47.7699 -121.8097	47.7988 -121.7166	47.7763 -121.7876	47.8088 -121.8325	47.7559 -121.7611	47.8148 -121.7759	47.8082 -121.7703	47.8009 -121.7781	47.7877 -121.8683	47.8206 -121.8519	47.8070 -121.8579	47.7942 -121.8665	47.8040 -121.8235	47.8664 -121.8298	47.8211 -121.8505	47.8303 -121.8482	47.8473 -121.8301	47.8596 -121.8125	47.8645 -121.8371	47.8663 -121.8298	47.7686 -121.8080	47.8450 -121.7696
Unit	Evbxp	Evap	Evtp	Evtp	Evtp	Evapd	Eigdy	Qgav	Evbxp	Qgav	Evtp	Evbxp	Qgav	Evbxp	Qcol	Evtp	Evap	Qa	Qco	Qcol	Qco	Qco	Qa	Qco	Qco	Eip	KJmv
La	16.66	13.60	10.56	11.07	11.45	10.67	15.84	15.33	14.14	24.62	22.63	24.30	12.77	13.42	69.74	14.04	11.01	13.37	14.56	14.28	10.78	13.26	12.24	12.85	10.64	11.93	8.41
Ce	30.15	28.45	23.40	24.79	24.94	23.20	34.06	30.20	29.25	53.73	44.24	49.70	26.50	27.17	140.36	28.48	26.28	27.91	31.53	30.70	21.52	27.09	24.86	27.67	21.05	23.36	16.72
Pr	3.82	3.61	3.00	3.22	3.30	2.99	4.37	3.66	3.90	6.71	5.26	6.13	3.42	3.44	14.45	3.60	2.70	3.43	3.63	3.74	2.65	3.35	3.12	3.14	2.67	3.48	2.08
Nd	15.18	14.75	12.48	13.25	14.24	12.37	18.03	14.34	15.95	26.51	20.13	24.38	13.93	13.74	50.92	14.21	10.68	13.71	14.40	15.24	10.34	13.36	12.32	12.38	10.50	14.92	8.33
Sm	3.27	3.51	2.95	3.17	3.60	3.05	4.30	3.18	3.64	5.75	4.23	5.46	3.37	3.22	8.69	3.25	2.47	3.05	3.24	3.45	2.28	2.96	2.80	2.74	2.45	3.74	1.86
Eu	0.96	1.20	1.00	1.10	1.15	0.98	1.04	0.99	1.29	1.66	1.19	1.51	1.16	0.82	2.68	0.97	0.76	0.89	0.96	1.02	0.74	0.92	0.87	0.81	0.78	1.17	0.73
Gd	3.31	3.52	2.99	3.18	3.81	3.05	4.40	3.08	3.53	5.19	3.99	5.42	3.49	3.19	7.08	3.23	2.46	3.11	3.21	3.41	2.26	2.92	2.78	2.54	2.44	4.09	1.85
Tb	0.54	0.59	0.49	0.52	0.63	0.52	0.75	0.53	0.58	0.82	0.64	0.91	0.59	0.53	1.07	0.56	0.43	0.56	0.55	0.57	0.38	0.48	0.46	0.44	0.43	0.69	0.30
Dy	3.19	3.62	2.95	3.07	3.83	3.13	4.55	3.14	3.36	4.56	3.78	5.58	3.57	3.19	5.94	3.48	2.67	3.65	3.39	3.50	2.41	2.99	2.85	2.66	2.72	4.23	1.88
Ho	0.65	0.72	0.60	0.61	0.77	0.62	0.92	0.64	0.66	0.87	0.76	1.14	0.74	0.64	1.12	0.73	0.54	0.78	0.69	0.69	0.51	0.62	0.58	0.52	0.58	0.87	0.38
Er	1.73	1.93	1.56	1.64	2.03	1.70	2.48	1.71	1.73	2.30	2.04	3.10	1.94	1.74	2.92	2.02	1.48	2.27	1.94	1.97	1.39	1.67	1.60	1.43	1.63	2.40	1.06
Tm	0.24	0.28	0.22	0.24	0.29	0.24	0.36	0.25	0.24	0.32	0.31	0.46	0.28	0.25	0.40	0.29	0.22	0.33	0.28	0.28	0.21	0.24	0.24	0.21	0.24	0.34	0.16
Yb	1.56	1.72	1.42	1.51	1.83	1.58	2.27	1.59	1.54	2.00	1.94	2.88	1.80	1.59	2.58	1.92	1.40	2.15	1.81	1.78	1.35	1.58	1.50	1.39	1.59	2.19	1.02
Lu	0.25	0.27	0.22	0.23	0.28	0.25	0.34	0.25	0.23	0.31	0.31	0.45	0.28	0.24	0.41	0.30	0.23	0.33	0.29	0.28	0.21	0.24	0.24	0.21	0.24	0.34	0.16
Ba	413	176.81	141	134	169	32	165	285	239	197	383	451	213	213	2213	314	375	455	415	329	466	336	369	485	461	415	492
Th	3.59	1.91	1.34	1.30	1.93	1.62	4.81	3.80	1.83	2.34	5.67	4.98	2.09	3.19	8.20	2.60	2.66	3.70	3.75	2.91	3.21	2.93	3.00	3.44	2.96	2.49	2.51
Nb	6.55	8.32	6.94	8.26	7.53	7.24	8.16	8.24	8.73	17.46	10.70	12.25	7.52	6.84	92.84	7.83	6.23	5.77	8.77	8.49	3.61	7.01	5.56	4.72	4.45	4.88	3.13
Y	18.73	18.29	15.39	15.58	19.40	15.57	23.92	16.29	17.25	22.39	20.23	29.54	18.84	16.38	28.48	18.35	13.42	19.94	17.52	17.75	12.85	15.69	14.86	12.94	14.78	22.83	9.92
Hf	3.65	3.46	2.80	3.04	3.22	3.08	4.35	3.90	3.25	5.79	5.10	6.22	3.50	3.96	7.74	3.19	3.35	3.61	3.88	3.80	2.51	3.54	3.16	2.98	2.80	2.40	1.98
Ta	0.61	0.61	0.48	0.55	0.54	0.50	0.68	0.69	0.63	1.16	0.88	0.97	0.58	0.56	5.83	0.56	0.47	0.44	0.65	0.61	0.29	0.54	0.44	0.35	0.35	0.33	0.23
U	0.84	0.55	0.29	0.51	0.66	0.44	1.74	1.22	0.64	0.80	1.37	1.62	0.68	1.05	2.24	0.90	0.92	1.16	1.16	0.97	1.18	1.00	1.06	1.35	1.18	0.99	0.88
Pb	3.36	2.03	1.05	1.11	2.47	2.60	3.14	2.65	2.63	3.62	2.98	3.73	2.66	2.39	3.68	18.15	4.93	8.14	5.50	5.96	7.64	4.51	4.46	7.79	8.71	6.15	7.74
Rb	25.6	4.26	17.1	19.0	6.4	5.2	28.0	27.4	15.2	13.3	44.7	40.8	17.0	11.2	68.4	20.9	25.4	39.2	40.5	22.9	38.3	26.4	29.0	33.8	41.1	29.2	40.6
Cs	0.13	0.19	0.50	0.35	0.08	1.73	0.68	0.10	0.25	0.62	0.45	0.30	0.31	0.30	1.65	0.81	0.71	1.80	1.84	1.03	1.75	0.76	0.70	1.47	2.11	1.40	1.86
Sr	316	306.81	204	169	288	192	258	268	366	430	216	236	317	277	567	255	195	262	186	265	310	245	244	219	262	176	321
Sc	12.1	18.56	13.3	15.4	18.4	14.3	13.6	11.9	9.5	14.4	9.0	11.6	14.4	13.5	13.4	16.6	11.9	13.8	15.2	14.7	10.0	11.8	10.9	11.9	12.0	17.0	8.1
Zr	134	137.97	113	124	122	119	145	146	128	249	199	247	132	148	362	122	127	133	145	146	91	133	118	108	98	88	70

* average of two chemical analyses
[Z] U-Pb zircon sample
[L] OSL/IRSL age sample
[R] Radiocarbon age sample

Appendix D. Earthquake Epicenters, Hypocenters, and Focal Mechanisms in and near the Sultan 7.5-minute Quadrangle

To better understand the relationships among mapped faults, we analyzed earthquake data for an area in and around the Sultan quadrangle using our geologic/geophysical interpretations and sense of fault movement at depth. This broader study area boundary is shown in Figure D1 and encompasses 674 epicenters and 46 focal mechanisms obtained from the Pacific Northwest Seismic Network (PNSN)(http://www.pnsn.org). The resultant focal-mechanism stereonets are shown as icons in Table D1 below. These stereonets provide information on the geometry of the earthquake-generating fault, including the geometry of the potential fault planes and the sense of movement. The focal mechanism provides two potential fault plane solutions. We use our structural field data to interpret which of the planes is the likely failure surface, especially for earthquakes in the CCFZ. The PNSN hypocenter depths are less than 25 mi (40 km) and are interpreted as crustal events unrelated to plate subduction. The P and T axes determined from these data constrain focal mechanism plots on stereonets and are used to calculate rakes (Lees, 1999, 2007, 2008). The reported focal mechanism solutions shown in Table D1 are extracted from pick files (M cards) provided by PNSN. See *Fault Nomenclature, Activity, and Structures* and Dragovich and others (2010a,b, 2011a,b, 2012) for further information, including more detailed mapping of the Duvall earthquake epicenters.

Table D1. Hypocenter, epicenter, and focal mechanism data for the Sultan quadrangle area. This table provides the focal mechanism ID number and the strike, dip, and rake for both of the focal mechanism solutions' nodal planes. See Figure D1 for epicenter locations in and around the Sultan map area. We label the epicenters having focal mechanisms with the focal mechanism ID number on Figure D1. The earthquake identification number gives the date (yr/month) and time (day, hr, decimal second) in sequential order without spaces. *Italicized rows* are earthquakes outside the Sultan 7.5-minute quadrangle but shown on Figure D1; focal mechanisms 3 and 18 are not shown in Figure D1 and are just outside the study area boundary. Focal mechanisms within the CCFZ are indicated in the right column by "CCFZ". The preferred fault plane solution (bold data) is the preferred focal mechanism fault plane and fault rake orientation within the CCFZ, given our left-lateral, northeast-trending CCFZ model. For CCFZ earthquakes, strike-slip or oblique-slip focal mechanisms with a left-lateral sense of offset for the north- to northeast-trending solution plane are denoted by (S), while reverse or oblique-reverse focal mechanisms with a component of left-lateral sense of offset for the north- to northeast-trending solution plane are denoted by (R). Note that the hypocenter and focal mechanism data show a strong correlation with the kinematics of the northeast-trending CCFZ where about 28 percent of the focal mechanisms in the CCFZ have a left-lateral or left-lateral-oblique northeast-trending fault solution, and this expands to about 40 percent of the CCFZ focal mechanisms if the reverse or reverse-oblique-slip solutions with a component of left-lateral offset are included. An even higher percentage (70 %) of left-lateral or left-lateral-oblique northeast-trending earthquakes occur along the southern portion of the CCFZ in the Lake Joy and Monroe quadrangles as noted in Dragovich and others (2012).

Focal mechanism ID no.	Earthquake ID number; depth (km); magnitude	Latitude & longitude (decimal degree)	Strike(°)1	Dip(°)1	Rake(°)1	Strike(°)2	Dip(°)2	Rake(°)2	Preferred fault type	Focal mechanism illustration	CCFZ quakes
FM_1	AF200292573055.2; 7.25; 2.4	47.7908 -121.8228	70	45	40	-51	63	127	reverse-oblique strike-slip		CCFZ
FM_2	*AF2003131224728.18; 0.03; 2.5*	*47.7438 -121.8382*	***40***	***70***	***-30***	*141*	*62*	*-157*	*normal-oblique strike-slip* (S)		*CCFZ*
FM_3	*AF200362861550.27; 15.68; 2.4*	*47.9305 -121.8382*	*105*	*25*	*80*	*-64*	*65*	*95*	*reverse*		*Outside map*
FM_4	AF2004425144233.32; 17.7; 2.5	47.8237 -121.8668	45	15	140	**174**	**80**	**78**	reverse-oblique strike-slip (R)		
FM_5	AF200511912727.99; 0.4; 2.4	47.7673 -121.8442	25	45	80	219	46	100	reverse		CCFZ
FM_6	AF200512275467.52; 12.42; 2.3	47.7692 -121.8245	**0**	**40**	**-21**	106	77	-128	normal-oblique strike-slip		CCFZ
FM_7	AF20061294341.25; 4.71; 2.0	47.7605 -121.8448	**20**	**20**	**160**	129	83	71	reverse-oblique strike-slip		CCFZ

Focal mechanism ID no.	Earthquake ID number; depth (km); magnitude	Latitude & longitude (decimal degree)	Strike(°)1	Dip(°)1	Rake(°)1	Strike(°)2	Dip(°)2	Rake(°)2	Preferred fault type	Focal mechanism illustration	CCFZ quakes
FM_8	AF200671983011.99; 2.13; 2.4	47.7728 -121.8670	75	45	120	**216**	**52**	**64**	oblique reverse (R)		CCFZ
FM_9	AF20061028183132.86; 7.15; 2.8	47.7635 -121.8670	110	70	160	**207**	**71**	**21**	reverse-oblique strike-slip (R)		CCFZ
FM_10	AF200771223028.53; 7.63; 2.8	47.8318 -121.8575	50	70	-110	-83	28	-47	oblique normal		
FM_11	AF2008112673127.89; 17.53; 2.8	47.7783 -121.7723	50	45	90	230	45	90	reverse		
FM_12	AF2010928151228.66; 7.81; 1.9	47.7692 -121.8478	-60	80	-150	**204**	**61**	**-12**	normal-oblique strike-slip (S)		CCFZ
FM_13	*AF197851614526.55; 5.98; 1.8*	*47.9125 -121.9033*	*70*	*70*	*110*	*203*	*28*	*47*	*oblique reverse*		
FM_14	*AF1980919225316.28; 4.4; 3.8*	*47.9075 -121.8230*	**15**	**60**	**50**	*254*	*48*	*138*	*oblique reverse*		*CCFZ*
FM_15	*AF1980921174512.97; 3.15; 3.5*	*47.9085 -121.8243*	*-90*	*90*	*40*	**180**	**50**	**180**	*reverse-oblique strike-slip*		*CCFZ*
FM_16	AF1987110132614.8; 18.54; 2.0	47.8612 -121.8687	165	45	110	-42	48	71	oblique reverse		
FM_17	AF198852916935.34; 13.85; 2.2	47.7747 -121.8355	**25**	**35**	**50**	251	64	114	oblique reverse		CCFZ
FM_18	*AF1990215183459.15; 16.34; 3.4*	*47.9218 -121.9233*	*15*	*55*	*40*	*259*	*58*	*137*	*reverse-oblique strike-slip*		*Outside map*
FM_19	AF19925415557.58; 17.43; 2.5	47.7890 -121.8443	70	45	90	250	45	90	reverse		CCFZ
FM_20	AF199622022213.19; 5.38; 2.6	47.7670 -121.8628	55	55	100	218	36	76	reverse		CCFZ
FM_21	AF1996534422.67; 4.35; 5.4 (Duvall quake main shock)	47.7608 -121.8760	10	60	100	171	31	74	reverse		CCFZ
FM_22	AF199653620146.95; 5.02; 2.6	47.7637 -121.8692	80	60	120	**211**	**41**	**49**	oblique reverse (R)		CCFZ
FM_23	AF199653152724.31; 7.5; 2.7	47.7580 -1218628	105	75	170	**198**	**80**	**15**	strike-slip (S)		CCFZ
FM_24	AF19965316755.47; 5.4; 2.5	47.7697 -121.8605	**175**	**55**	**-50**	-61	51	-133	oblique normal		CCFZ
FM_25	AF199654121646.77; 7.33; 2.6	47.7798 -121.8597	105	35	100	-87	56	83	reverse		CCFZ
FM_26	*AF199654153720.45; 6.54; 2.5*	*47.7733 -121.8797*	**185**	**40**	**90**	*5*	*50*	*90*	*reverse*		*CCFZ*
FM_27	AF19965581339.57; 4.86; 2.6	47.7578 -121.8600	60	50	90	240	40	90	reverse		CCFZ
FM_28	AF1996559610.86; 7.33; 2.6	47.7758 -121.8738	100	70	171	**193**	**81**	**20**	strike-slip (S)		CCFZ
FM_29	AF19965511623.53; 8.46; 3.0	47.7705 -121.8745	25	30	100	193	61	84	reverse		CCFZ

Focal mechanism ID no.	Earthquake ID number; depth (km); magnitude	Latitude & longitude (decimal degree)	Strike(°)1	Dip(°)1	Rake(°)1	Strike(°)2	Dip(°)2	Rake(°)2	Preferred fault type	Focal mechanism illustration	CCFZ quakes
FM_30	AF19965743916.97; 4.57; 2.7	47.7613 -121.8557	**25**	**55**	**140**	141	58	43	reverse-oblique strike-slip		CCFZ
FM_31	AF19965764519.39; 4.27; 2.3	47.7555 -121.8673	95	85	140	**189**	**50**	**6**	reverse-oblique strike-slip (R)		CCFZ
FM_32	AF19965772961.09; 4.11; 2.7	47.7650 -121.8617	75	65	170	**169**	**81**	**25**	strike-slip (S)		CCFZ
FM_33	*AF199651064068.61; 8.3; 2.7*	*47.7693 -121.8833*	*120*	*70*	*171*	**213**	**81**	**20**	*strike-slip* (S)		*CCFZ*
FM_34	*AF199651243611.92; 4.25; 2.7*	*47.7645 -121.8828*	*120*	*70*	*-130*	**8**	**44**	**-29**	*oblique normal*		*CCFZ*
FM_35	AF1996512125153.35; 6.15; 2.8	47.7588 -121.8485	-35	60	40	212	56	143	reverse-oblique strike-slip		CCFZ
FM_36	*AF1996513152851.39; 6.87; 2.4*	*47.7850 -121.8775*	*190*	*80*	*150*	*-74*	*61*	*12*	*reverse-oblique strike-slip*		*CCFZ*
FM_37	AF1996516183359.85; 5.01; 2.6	47.7568 -121.8540	**35**	**90**	**70**	-55	20	180	oblique reverse (R)		CCFZ
FM_38	AF19966172223.84; 8.56; 3.2	47.7920 -121.8172	165	65	100	-38	27	69	reverse		CCFZ
FM_39	AF1996691452 51.03; 7.9; 3.0	47.7630 -121.8405	**165**	**60**	**30**	59	64	146	reverse-oblique strike-slip		CCFZ
FM_40	AF19966192147183.05; 7.43; 3.0	47.7867 -121.8188	160	55	-20	**262**	**74**	**-143**	normal-oblique strike-slip (S)		CCFZ
FM_41	AF199662619748.62; 8.84; 2.6	47.7837 -121.8567	90	50	130	**217**	**54**	**52**	oblique reverse (R)		CCFZ
FM_42	*AF19967322443.71; 14.19; 3.2*	*47.7885 -121.8790*	**20**	**50**	**150**	*130*	*67*	*44*	*reverse-oblique strike-slip*		*CCFZ*
FM_43	AF1996102775328.42; 5.4; 2.6	47.7542 -121.8600	-65	80	170	**27**	**80**	**10**	strike-slip (S)		CCFZ
FM_44	AF1997219205243.21; 5.3; 1.8	47.7552 -121.8560	-75	80	180	**195**	**90**	**-10**	strike-slip (S)		CCFZ
FM_45	AF1997921151345.74; 6.25; 2.1	47.7677 -121.8682	125	35	110	-79	57	77	oblique reverse		CCFZ
FM_46	AF1997101923619.09; 5.44; 3.1	47.7675 -121.8638	135	30	-20	242	80	-119	normal-oblique strike-slip		CCFZ
FM_47	*AF1998624155317.85; 3.95; 2.5*	*47.7643 -121.8852*	*90*	*55*	*100*	*253*	*36*	*76*	*reverse*		*CCFZ*
FM_48	AF199977223055.67; 5.74; 1.9	47.7620 -121.8488	145	25	40	18	74	110	reverse-oblique strike-slip		CCFZ
FM_49	AF1999727125953.73; 4.5; 2.2	47.7732 -121.8662	5	25	140	132	74	70	reverse-oblique strike-slip		CCFZ
FM_50	AF1999825174843.49; 7.43; 2.0	47.7590 -121.8613	**10**	**45**	**0**	-80	90	135	strike-slip (S)		CCFZ
FM_51	AF201304291608; 2.52; 2.5	47.771 -121.819	105	50	-100	300	41	-78	normal (S)		

THIS PAGE INTENTIONALLY LEFT BLANK.

Figure D1 Explanation

38 Focal Mechanisms

Depth (km)	Magnitude
0 - 2.5	0 - 1
2.6 - 5	1.1 - 2
5.1 - 10	2.1 - 3
10.1 - 15	3.1 - 5
15.1 - 20	5.1 - 6
20.1 - 25	
25.1 - 30	
30.1 - 34.2	

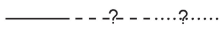

Fault, unknown offset—Solid where location accurate; dashed where inferred; dotted where concealed; queried where identity or existence questionable

Thrust fault—Solid where location accurate; dashed where inferred; dotted where concealed; sawteeth on upper (tectonically higher) block

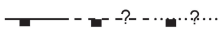

Reverse fault—Solid where location accurate; dashed where inferred; dotted where concealed; queried where identity or existence questionable; rectangles on upthrown block

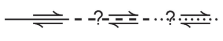

Right-lateral strike-slip fault—Solid where location accurate; dashed where inferred; dotted where concealed; queried where identity or existence questionable; arrows show relative motion

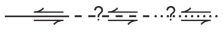

Left-lateral strike-slip fault—Solid where location accurate; dashed where inferred; dotted where concealed; queried where identity or existence questionable; arrows show relative motion

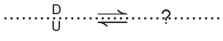

High-angle right-lateral, oblique-slip fault—Location concealed; queried where identity or existence questionable; arrows show relative horizontal motion; U, upthrown block; D, downthrown block

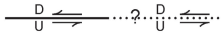

High-angle left-lateral, oblique-slip fault—Solid where location accurate; dotted where concealed; arrows show relative horizontal motion; U, upthrown block; D, downthrown block

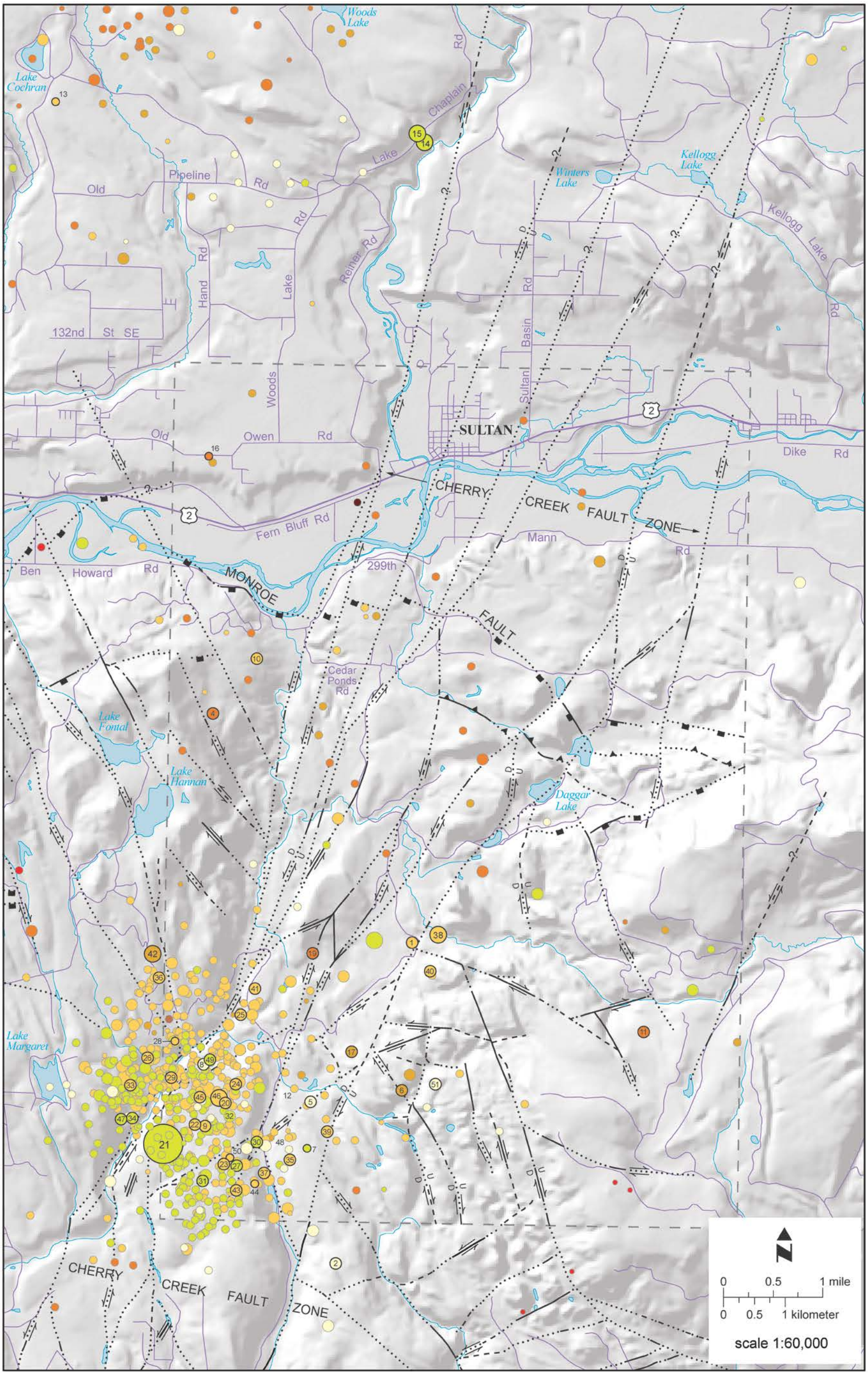

Figure D1. Earthquake epicenters in and around the Sultan 7.5-minute quadrangle (dashed box). Focal mechanism data for the numbered epicenters with bold outlines are presented in Table D1. Faults are simplified from our current mapping and Dragovich and others (2010a, 2011a, 2012).

THIS PAGE INTENTIONALLY LEFT BLANK.

Appendix E. Photographs of Geologic Features

Figure E1. Faulted Vashon advance lake deposit diamicton (unit Qgl_V) at significant site 31D (on map) along Youngs Creek in the western portion of the Sultan 7.5-minute quadrangle. We map this area as unit Qtz due to the high incidence of fracturing and faulting as well as probable liquefaction features caused by Quaternary faulting near the main strand of the CCFZ. See photo E5 for a probable tectonic fault also displacing unit Qgl_V downstream of this site. These features, along with the location of the Duvall earthquake to the SSW, are consistent with the CCFZ being an active fault zone. View is to the southwest and shows the north-northeast-trending steep fractures that are subparallel to the CCFZ (left photo). The photo on the right shows a close-up view of clast orientation along the fractures. We obtained a radiocarbon-infinite age from nearby age site 31E (>43.5 ka) just downstream (map, Appendix A).

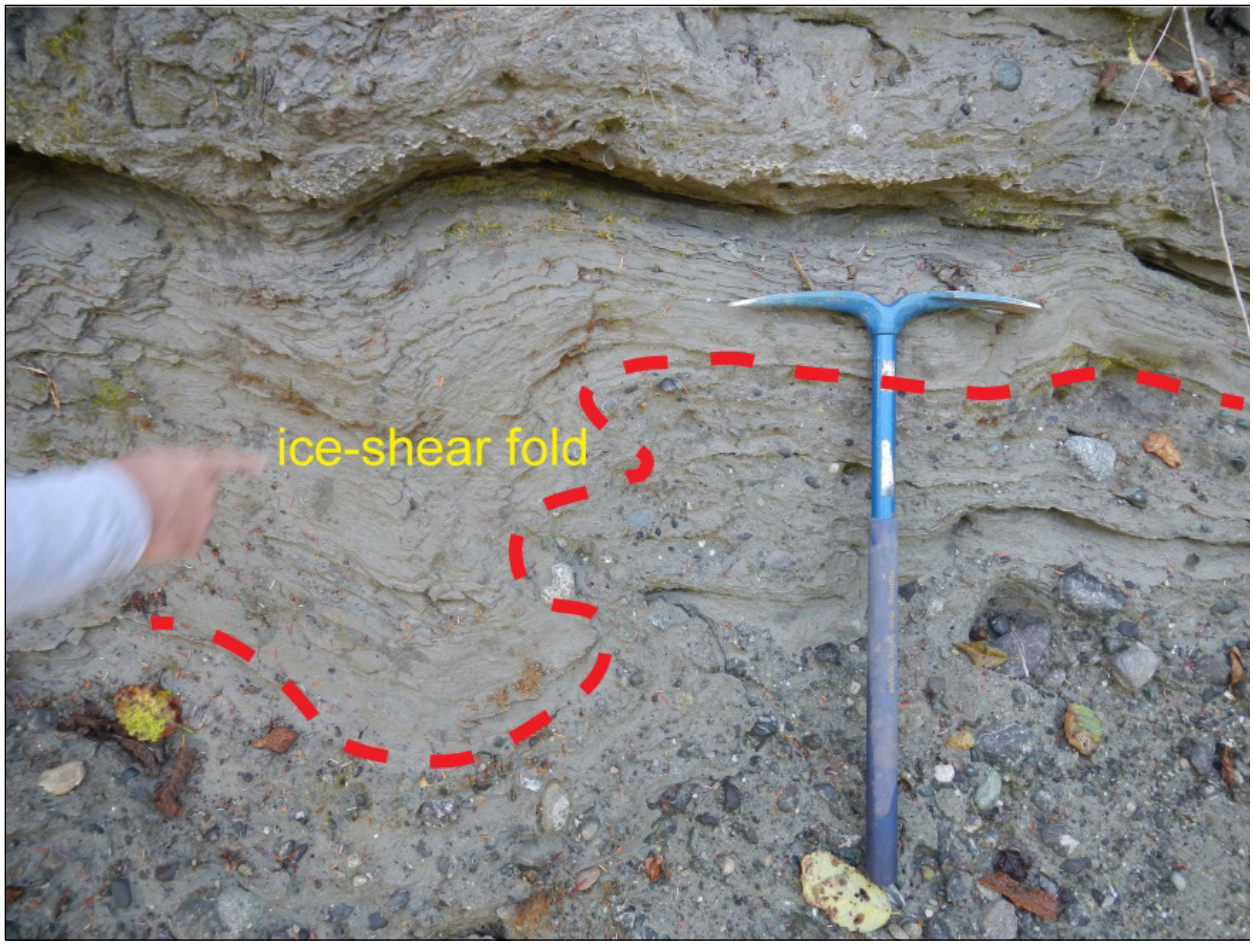

Figure E2. An ice-shear fold in unit Qgl_V at site 31F along Youngs Creek, directly southwest of age site 31E (map, Appendix A) in the Sultan 7.5-minute quadrangle. The fold axis trends N67°E and plunges 5° NE, and the axial plane for the fold dips shallowly to the west-northwest, consistent with ice flowing to the east-southeast. Ice-shear structures such as these have a flat plane of shear, commonly producing inclined to overturned folds with flat to gently dipping axial planes similar to thrust-generated structures. Folds are overturned in the direction of ice shear. At this site, laminated silt advance lake deposits grade into subtly bedded to massive diamicton. These diamicton beds are the result of aqueous debris flows and can mimic the look of some till. Flow till and iceberg dump deposits are very commonly interbedded with unit Qgl_V laminated silts and clays in the region. Look direction is to the southwest.

Figure E3. Liquefaction or ice-shear deformation of unit Qc_{pf} at site 312F. View is to the west and shows distorted and disturbed beds with minor folds. Site is east of the city of Sultan in the Sultan 7.5-minute quadrangle and directly south of significant site 312K (on map). Outcrop is within a 140-ft (43 m)-wide by 60-ft (18 m)-high exposure of nonglacial Skykomish River basin–provenance ancient alluvium. Strata at this site consist of very stiff folded and distorted thin-bedded clay, sand, and silt with some oxidized beds. Upper photo shows variable fold axes, some trending N60°E, and minor folds with a shallow plunge. Bottom photo shows intensely folded and distorted bedding with many rootless folds and overturned folds. (See similar deformation at nearby site 312G on Figure E4 below.)

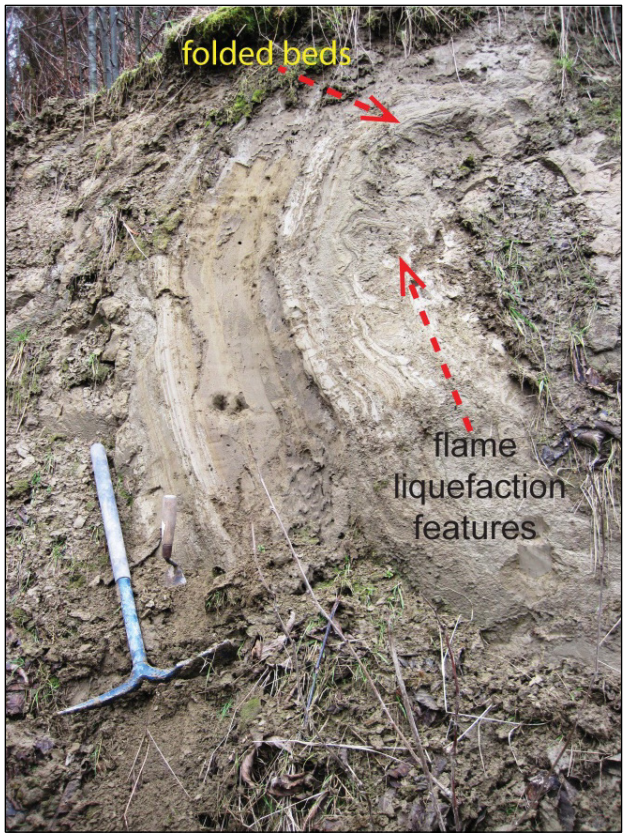

Figure E4. Looking northwest at folded and distorted beds in ancient Skykomish River alluvium (unit Qc_{pf}) at site 312G. Site is directly south of significant site 312K (on map) and next to site 312F (Fig. E3) east of the city of Sultan in the Sultan 7.5-minute quadrangle. Strata at this site consist of nonglacial Skykomish River basin–provenance ancient alluvium and are composed of thin beds of clay, silt, and sand with some thick beds of massive sand. Beds are very dense and highly folded or distorted with local areas of blocky broken strata or overturned folds. Flames in thin beds of sand are visible in the middle of the outcrop. Fold axes range in trend from N47°W to S80°W and plunge between 80°NE and 33°SW respectively. Ice-related deformation, liquefaction, and tectonic deformation are possible at this site and at nearby site 312F (Fig. E3). We tentatively postulate that the distinct steep southeast tilt of these beds at several spaced sites in the area are the result of tectonic deformation by nearby concealed fault strands within the CCFZ. Intense liquefaction, or perhaps ice-related shearing, may have contributed to some of the high-strain deformation observed. Thus, this outcrop may record deformation by several mechanisms.

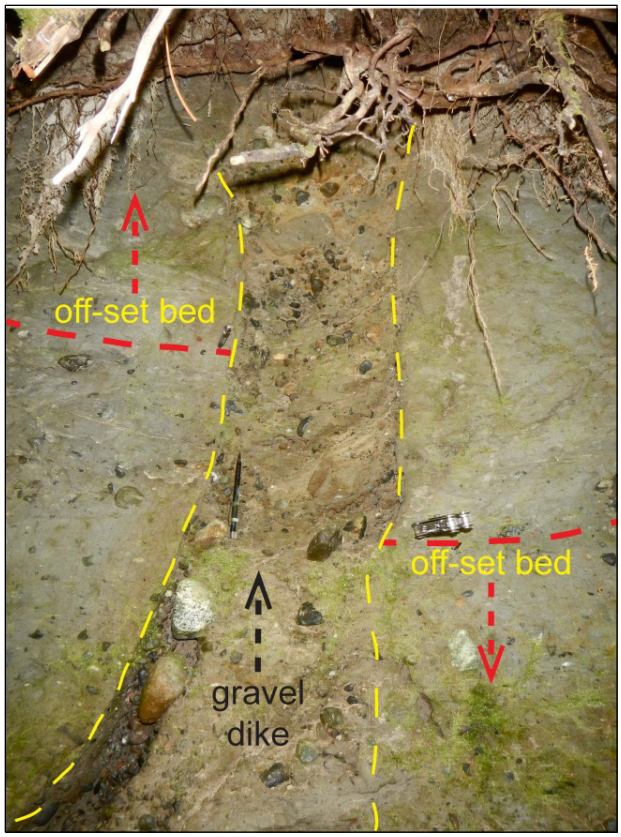

Figure E5. Faulted advance lake deposits (unit Qgl_v) at significant site 31G on Youngs Creek in the western portion of the Sultan 7.5-minute quadrangle. We map this area as unit Qtz due to the high incidence of probable Quaternary faulting and liquefaction features near the main strand of the CCFZ. View is to the southwest and shows disturbance of laminated to thinly bedded silt and silty sand with thick beds of diamicton below. Offset of a distinct silty sand marker bed indicates 11 in. (28 cm) of west-side-up offset along this small fault. (Red arrows show offset direction, and red line shows contact between silt-sand beds and diamicton.) The marker bed is overlain by thinly bedded to laminated silts lacking gravel and underlain by silty sand diamicton. The fault strikes N30°E and dips subvertically. A gravel dike within the fault is likely the result of earthquake-induced liquefaction, perhaps produced by faulting. Other small outcrops of fractured and likely faulted advance lake deposits were noted in this area of unit Qtz along Youngs Creek. See Figure E1 for probable tectonic disturbance in unit Qgl_v near this site.

Appendix F. U/Pb Geochronology

Table F1. Sample 11G U-Pb zircon data from unit $Eigd_y$ in the Gold Bar 7.5-minute quadrangle. Forty-nine zircons were analyzed from the granodiorite of the Youngs Creek intrusive complex. (See unit $Eigd_y$ for outcrop and petrographic description of the sample.) The age estimates are 39.35 ±0.31 to 42.99 ±0.26 Ma, depending upon the minimum zircon population chosen (Fig. F1). Note the lack of old or "exotic" zircons as compared to Table F2 and samples found regionally in the volcanic rocks of Mount Persis (for example, Dragovich and others, 2011b); cps = counts per second.

Sample 11G from the Gold Bar 7.5-minute Quadrangle								
Zircon grain no. (n=49 zircons)	**^{206}Pb (cps)**	**^{204}(Pb+Hg) (cps)**	**^{238}U/^{206}Pb**	**2 σ**	**^{207}Pb/^{206}Pb**	**2 σ**	**^{206}Pb/^{238}U age (Ma)**	**2 σ error (Ma)**
zircon-7	21907	184	167.545	5.272	0.041	0.001	38	1
zircon-24	20702	183	167.890	5.605	0.042	0.001	38	1
zircon-40	21846	140	168.947	5.642	0.045	0.001	38	1
zircon-5	25516	181	162.811	5.513	0.046	0.002	39	1
zircon-10	24182	174	165.392	5.932	0.044	0.001	39	1
zircon-13	29978	212	165.519	5.468	0.044	0.001	39	1
zircon-17	24627	207	164.280	6.388	0.044	0.001	39	2
zircon-26	22817	196	162.741	5.414	0.041	0.001	39	1
zircon-27	32202	171	164.375	5.182	0.044	0.001	39	1
zircon-2	21207	161	161.916	5.216	0.045	0.001	40	1
zircon-4	28504	161	159.454	4.936	0.043	0.001	40	1
zircon-12	21579	181	162.239	4.937	0.042	0.001	40	1
zircon-16	25619	215	161.127	5.339	0.042	0.001	40	1
zircon-21	24128	216	161.207	6.156	0.043	0.001	40	2
zircon-22	23615	206	162.494	5.446	0.043	0.001	40	1
zircon-48	38320	217	161.024	6.269	0.050	0.002	40	2
zircon-49	25202	238	159.176	5.817	0.049	0.003	40	1
zircon-50	26087	230	159.921	5.162	0.048	0.001	40	1
zircon-30	10197	140	154.947	5.112	0.031	0.001	41	1
zircon-23	9052	166	153.328	6.145	0.039	0.003	42	2
zircon-29	16147	159	151.591	4.619	0.038	0.001	42	1
zircon-31	5012	152	152.925	5.383	0.031	0.005	42	1
zircon-39	12980	145	151.390	5.191	0.042	0.002	42	1
zircon-46	7508	178	154.164	5.231	0.038	0.002	42	1
zircon-6	10549	168	150.151	4.514	0.039	0.003	43	1
zircon-8	8587	173	147.815	4.776	0.037	0.002	43	1
zircon-9	11373	184	148.683	4.869	0.042	0.002	43	1
zircon-11	11655	181	151.059	5.519	0.038	0.002	43	2
zircon-14	10056	209	147.909	4.584	0.033	0.002	43	1
zircon-19	16609	202	149.292	4.722	0.040	0.002	43	1
zircon-25	15676	176	148.460	5.730	0.042	0.002	43	2
zircon-32	10912	140	150.301	4.808	0.038	0.003	43	1
zircon-33	12985	140	150.583	4.621	0.043	0.002	43	1
zircon-34	12669	169	150.816	4.954	0.040	0.001	43	1
zircon-35	8917	155	151.130	5.404	0.040	0.003	43	2
zircon-36	4649	147	150.292	5.457	0.028	0.003	43	2
zircon-37	14514	138	150.810	4.720	0.042	0.001	43	1
zircon-38	9262	150	150.565	5.127	0.045	0.004	43	1
zircon-42	8816	159	148.791	5.694	0.042	0.002	43	2
zircon-47	12213	218	149.135	4.770	0.045	0.002	43	1
zircon-1	5772	160	145.232	5.226	0.035	0.004	44	2
zircon-3	19179	173	145.145	4.603	0.043	0.001	44	1
zircon-18	8601	211	147.118	4.567	0.032	0.004	44	1
zircon-20	13691	229	146.424	4.821	0.040	0.002	44	1
zircon-28	14805	167	147.274	4.576	0.038	0.001	44	1

Sample 11G from the Gold Bar 7.5-minute Quadrangle								
Zircon grain no. (n=49 zircons)	**^{206}Pb (cps)**	**^{204}(Pb+Hg) (cps)**	**^{238}U/^{206}Pb**	**2 σ**	**^{207}Pb/^{206}Pb**	**2 σ**	**^{206}Pb/^{238}U age (Ma)**	**2 σ error (Ma)**
zircon-43	7149	186	146.450	5.601	0.040	0.004	44	2
zircon-45	9272	229	146.217	6.384	0.049	0.002	44	2
zircon-44	9820	182	144.037	4.936	0.043	0.002	45	2
zircon-15	15856	261	141.022	4.388	0.065	0.003	46	1

Table F2. Sample 47G U-Pb zircon data from unit Ei_p in the Sultan 7.5-minute quadrangle. Twenty-nine zircons were analyzed from this intrusive dacite of the Drunken Charlie Lake intrusive complex. (See unit Ei_p for sample information.) Note the old or exotic zircons obtained during intrusion from older country rock, with one zircon as old as the Precambrian (1,340 Ma). The crystallization age obtained was 46.46 ±0.37 Ma, using the youngest portion of the zircon population (Fig. F2); cps = counts per second.

Sample 47G from the Sultan 7.5-minute Quadrangle								
Zircon grain no. (n=29 zircons)	**^{206}Pb (cps)**	**^{204}(Pb +Hg) (cps)**	**^{238}U/^{206}Pb**	**2 σ**	**^{207}Pb/^{206}Pb**	**2 σ**	**^{206}Pb/^{238}U age (Ma)**	**2 σ error (Ma)**
zircon-20	10045	168	142.244	4.546	0.045	0.002	45	1
zircon-25	3248	140	142.608	4.742	0.024	0.005	45	1
zircon-28	16687	142	141.964	5.519	0.047	0.003	45	2
zircon-02	9626	137	139.177	4.705	0.045	0.002	46	2
zircon-03	5924	160	138.703	4.992	0.037	0.004	46	2
zircon-04	5036	170	140.777	5.211	0.031	0.003	46	2
zircon-06	7533	195	138.445	4.815	0.048	0.002	46	2
zircon-10	7913	224	138.986	5.553	0.053	0.004	46	2
zircon-11	10507	191	139.599	4.170	0.049	0.003	46	1
zircon-16	4185	182	138.898	5.311	0.035	0.004	46	2
zircon-19	9522	166	141.137	5.009	0.044	0.004	46	2
zircon-23	9895	161	139.272	5.686	0.047	0.003	46	2
zircon-24	15986	131	139.734	4.581	0.045	0.002	46	2
zircon-05	13478	183	135.575	4.584	0.050	0.003	47	2
zircon-07	7062	203	137.736	4.360	0.049	0.004	47	1
zircon-09	6638	223	137.811	4.700	0.049	0.004	47	2
zircon-12	6086	186	136.761	4.395	0.049	0.004	47	2
zircon-14	8775	206	136.656	5.196	0.050	0.002	47	2
zircon-17	6673	191	137.059	5.228	0.039	0.003	47	2
zircon-22	6229	127	136.535	4.433	0.030	0.002	47	2
zircon-08	6731	189	134.912	4.888	0.047	0.004	48	2
zircon-13	7291	203	134.768	4.637	0.057	0.004	48	2
zircon-18	11939	180	132.739	4.279	0.049	0.004	48	2
zircon-27	5672	147	132.541	5.143	0.041	0.004	48	2
zircon-26	24723	116	73.035	2.299	0.046	0.001	88	3
zircon-15	49019	223	63.024	2.154	0.060	0.002	101	3
zircon-01	43081	132	39.825	1.228	0.048	0.001	160	5
zircon-29	39909	131	38.741	1.388	0.053	0.003	164	6
zircon-21	1585989	174	4.328	0.182	0.088	0.001	1340	51

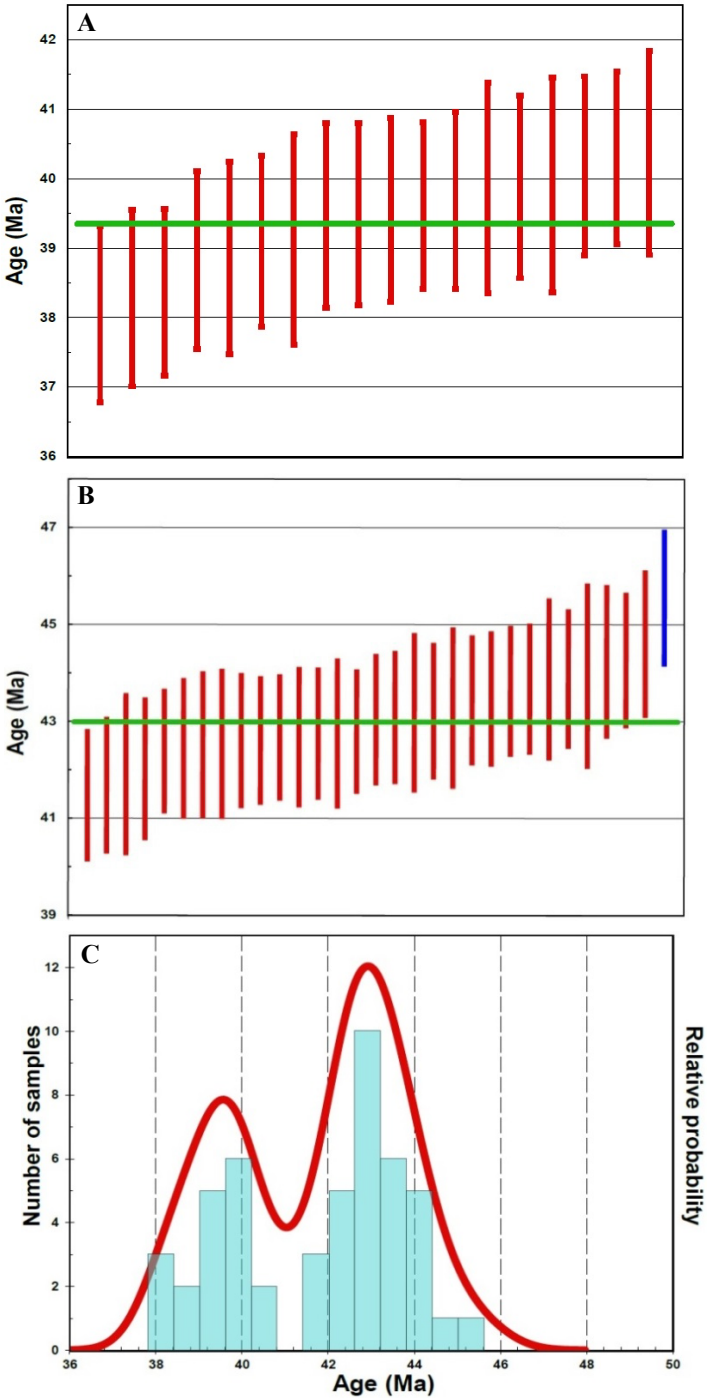

Mean = 39.35 ±0.31 [0.78%] 95% confidence
Weighted by data-point errors only,
0 of 18 rejected
MSWD = 1.14, probability = 0.31
(error bars are 2σ)

Mean = 42.99 ± 0.26 [0.60%] 95% confidence.
Weighted by data-points errors only,
1 of 31 rejected (blue line).
MSWD = 1.12, probability = 0.30
(error bars are 2σ)

Figure F1 . Zircon ages and age distribution for sample 11G. **A.** Outset and green line in graph show the weighted mean of $^{206}Pb/^{238}U$ zircon ages for the younger of the two populations in sample 11G. **B.** Outset and green line in graph show the weighted mean of $^{206}Pb/^{238}U$ zircon ages for the older of the two populations in sample 11G, excluding the oldest zircon (blue bar). **C.** Probability density plot with histogram shows the bimodal $^{206}Pb/^{238}U$ age distribution for the zircons sampled in graphs A and B. We suspect the youngest age (~39 Ma) represents the crystallization age of the granodiorite, but report both ages here and in the unit description. Most likely the age peaks represent two magmatic pulses. MSWD = mean standard weighted deviates.

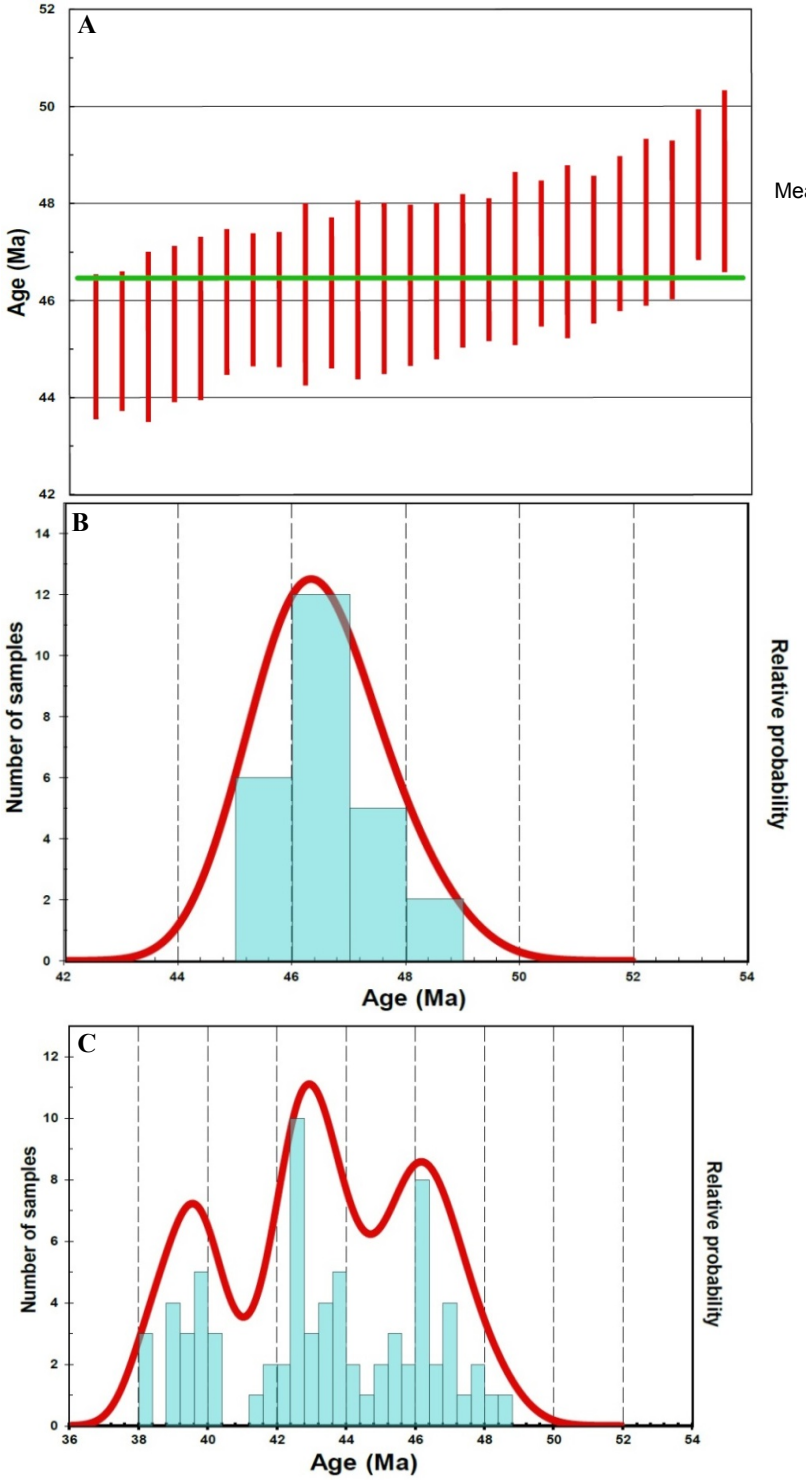

Figure F2..Zircon ages and age distribution for sample 47G; combined age distribution for samples 11G and 47G**. A.** Green line shows the weighted mean of $^{206}Pb/^{238}U$ zircon ages for youngest age population in sample 47G. **B.** Probability density plot with histogram for the zircon ages in A, showing a unimodal, approximately normal age distribution (for the young zircon population) consistent with random analytical errors, although a geologic source of the age scatter cannot be ruled out. **C.** Probability density plot with histogram of the Tertiary zircon ages for both samples (11G and 47G). The distribution of the age peaks indicates local intrusive activity in pulses over ~6–10 Ma.